Investigations of the Destruction Mechanism of High Pressure Water Jetting

By

Sergeï den Haan

University of Technology
Delft

August 8, 2019

TU Delft Delft University of Technology

Investigations of the Destruction Mechanism of High Pressure Water Jetting

by

Sergeï Franciscus den Haan

to obtain the degree of Master of Science
at the Delft University of Technology,
to be defended publicly on Thursday August 15, 2019 at 1:30 PM.

Student number:	4083806	
Project duration:	November 15, 2018 – August 15, 2019	
Thesis committee:	Prof. Dr. sc.nat D.F. Bruhn,	TU Delft, supervisor
	Assoc.Prof. Dr. ir. K.H.A.A. Wolf,	TU Delft
	Asst.Prof Dr. Ir. A.A.M. Dieudonné,	TU Delft
	Ir. S. Hahn,	International Geothermal Centre (GZB)

This thesis is confidential and cannot be made public until august 15, 2022.

TU Delft Delft University of Technology

Abstract

As the demand for green energy is growing, geothermal energy will play an important part in the future energy mix. Geothermal energy is widely used for both direct-use and electricity generation. A viable geothermal reservoir must have a sufficiently high temperature, a fluid pathway through the rock (permeability) and a fluid that can collect and transport the heat to the surface. Deeper reservoirs often have high temperatures and a low permeability, whereas shallow reservoirs often have a high permeability but low temperatures. When the permeability is too low, the reservoir can be stimulated. This is conventionally done by fracking the reservoir rock; that is, creating fractures to enhance the flow. This is a very expensive and potentially hazardous operation. Another technique is Radial Jet Drilling (RJD), which uses a high pressure focused fluid jet in order to drill small diameter horizontal holes (laterals) from the vertical borehole. Laterals can be drilled in multiple directions of the borehole and can be as long as 100 metres, potentially increasing the production 3-8 times (Blöcher et al., 2016). However, the destruction mechanism of rocks during jetting is not yet fully understood.

Experiments and simulations were conducted in order to investigate the destruction mechanism of a rock during jet impingement. First, experiments and simulations were carried out which had the aim to find a relation between stagnation pressure (exerted pressure on the rock by a water jet) and jetted cavity depth. The experiments provided information about the maximum jettable depth (with a static nozzle), while the simulations provided a continuous pressure depth relationship. Combining the simulation and experimental results leads to the conclusion that pressure fluctuations are key for the destruction process, which is consistent with the theorem of hydraulic fracturing.

Furthermore, a Finite Difference Method (FDM) solver was developed in order to investigate the pore pressure *inside* a porous rock during jet impingement. The solver was used to investigate (1) the difference in pressure between the first layer of pores (adjacent to impinged area) and the fluid pressure of the jet and (2) the influence of an increased pore pressure in the whole sample (i.e., back pressure). It became clear that the pressure fluctuations in time between the pores and jet are significant and sufficient enough to induce hydraulic fracturing. Increasing the back pressure resulted in higher pressure fluctuations, but only when the back pressure is higher than the average jetting pressure.

There are still some doubts in the literature in whether or not cavitation erosion is the governing destruction mechanism. Cavitation is the formation of vapour bubbles in a fluid due to fluid pressure drop below the vapour pressure. Once the bubbles travel to a higher pressure regime, they implode, creating either a shock wave or a mini jet, resulting in

erosion of material. Hahn et al. (2019) and Kumagai et al. (2011) evaluated the location of cavitation erosion on a flat surface and concluded that cavitation erosion is not the governing erosion mechanism as there was no damage at the impinged area. But those studies did not prove that cavitation erosion does not occur inside a hole. Experiments and simulations were therefore performed to investigate cavitation erosion *inside* a cavity. It is found that cavitation erosion does occur inside a cavity, even at cavity depths of >25mm. However, experiments on one of the rocks showed that the maximum jetting depth was 25mm. From these results, it was concluded that although cavitation erosion occurs inside a cavity, it cannot be the governing destruction mechanism.

Based on the results in this study, it is concluded that hydraulic fracturing is the governing erosion mechanism, because of the proved dependency of destruction on pressure fluctuations and the disprove of surface erosion due to shear forces (in literature, Buset et al. (2001)) and cavitation erosion being the governing mechanism. Another, in literature, proposed mechanism is pore-elastic tensile failure, which is partly interconnected with the theorem of hydraulic fracturing and not further investigated in this study. Based on this conclusion, a 'jetting correlation' was developed which is able to predict whether a rock is jettable or not. Combined with the pressure-depth relationship, it can also predict the maximum jetting depth. The correlation matched with the experimental results, which is another indication that hydraulic fracturing is the governing destruction mechanism.

Preface

This report outlines the research done by a master student of the Delft University of Technology, in cooperation with the International Geothermal centre in Bochum. It has been written to fulfil the graduation requirements of the Master Petroleum Engineering & Geosciences in order to obtain the degree Master of Science. The study was part of the ongoing research project SURE (Novel Productivity Enhancement Concept for a Sustainable Utilisation of a Geothermal Resource) which is funded by the EC 2020 horizon, to investigate Radial Jetting Technology.

The work presented henceforth was mostly conducted at the International Geothermal Centre (GZB), where I was allowed to make use of their laboratories and knowledge under the supervision of PhD candidate Simon Hahn and ir. Volker Wittig. I also made use of the knowledge and facilities of the Delft University of Technology with the help and supervision of prof. David F. Bruhn.

This project will be of most interest to readers that want to gain knowledge about the destruction mechanism of porous rocks during impingement by a high water pressure water jet used in the stimulation technique Radial Jet Drilling (RJD). The report describes experimental methods and simulations which give insights on the process of jetting a porous rock.

Sergeï den Haan
Delft, August 2019

Acknowledgements

Throughout my research, I received lots of help and assistance. I first want to thank Volker Wittig and Rolf Bracke for giving me the opportunity to use the knowledge and facilities of the International Geothermal Centre (GZB) during my six months internship. Furthermore, I want to thank all the employees of the 'Advanced Drilling Department' of GZB, but particularly PhD candidate Simon Hahn, who helped me with my research throughout these six months. He always made time to discuss various subjects and always gave useful input, he was of great support both socially and scientifically. I also want to thank student and part-time employee of GZB, Fehrat Kör, who was always willing to help with manufacturing parts which were needed for the experiments, where he also gave useful input of on how to change or improve the experiments. Furthermore, I want to thank Sarah Jasper for helping in the laboratory, and prof. Ralph Lindken from the Hochshule Bochum for the valuable discussions and feedback on both the experiments and simulations. Finally, I want to thank Dr. Shahin Jamali, who was willing to make microscopic images on a very short time notice.

I want express my gratitude towards my supervisor prof. David Bruhn from the TU Delft. He made it possible for me to do an internship at GZB. He was, although his busy schedule, always available for meetings, either in person or via skype. I am especially grateful for his support during the last phase of my thesis project, where he spent a lot of time helping me with structuring my thesis and gave constructive comments and points of improvements. I also want to thank Wim Overweel and Joost van Meel from the TU Delft, who could both help me on very short notice with making CT-scans and microscopic images. I am also very honoured and thankful to both assoc. prof. Karl-Heinz Wolf and ass. prof. Anne-Catherine Dieudonné who are both on my graduation committee. Karl-heinz Wolf was a great supervisor during my bachelor thesis, where Anne-Catherine Dieudonné was also in my committee. I am very pleased that they were both willing to be on my master committee again.

Finally I want to thank my family and close friends, they were of great support during my entire time in Delft, and were always willing to help where they could. I want to especially thank my girlfriend, who was of great support throughout my whole study. She has checked this thesis for spelling and content for which I am very grateful.

Nomenclature

ϵ	Turbulence dissipation rate	$[m^2/s^3]$
μ	Dynamic viscosity	$[Pa \cdot s]$
ω	Specific turbulence dissipation rate	$[s^{-1}]$
ϕ	Porosity	[-]
ρ	Density	$[kg/m^3]$
σ	Stress	$[Pa]$
A	Area	$[m^2]$
BC	Boundary Condition	[-]
C	Capacitance	[Farad]
C_{eff}	Compressibilty factor	[-]
CFD	Computational Fluid Dynamics	[-]
CT	Computer Tomography	[-]
D	Pore throat diameter	$[m]$
$DDES$	Delayed Detached Eddy Simulation	[-]
DES	Detached Eddy Simulation	[-]
EGS	Enhanced Geothermal System	[-
F	Force	$[N]$
f	Frequency	$[Hz]$
FDM	Finite Difference Method	[-]
HCP	Hexagonal Closed Packing	[-]
K	Permeability	[mD]

k	Turbulence kinetic energy	$[m^2/s^2]$
KI	Fracture toughness	$[Pa\sqrt{m}]$
L	Length	$[m]$
LES	Large Eddy Simulation	[-]
P	Pressure	$[Pa]$
PDE	Partial Differential Equation	[-]
PIV	Particle Imagine Velocimetry	[-]
Q	Volumetric flow rate	$[m^3/s]$
R	Resistance	$[\Omega]$
r	Radius	$[m]$
$RANS$	Reynolds-Averaged Navier Stokes	[-]
RJD	Radial Jet Drilling	[-]
ROP	Rate of Penetration	$[m/s]$
S	Saturation	[-]
SST	Shear Stress Transport	[-]
t	Time	$[s]$
U	Electrical Potential	[V]
UCS	Ultimate Compressive Strenght	$[Pa]$
UTS	Ultimate Tensile Strenght	$[Pa]$
V	Volume	$[m^3]$

Contents

1. Introduction

To meet the Paris agreement, the future energy mix will change drastically. Geothermal energy has already become more important over the past years and the need for this type of energy will only increase further in the coming decades. It is an attractive source of energy because (1) it is constantly available (other than solar and wind energy) and (2) it can be used for both direct (district) heating and electricity generation depending on location and reservoir depth. A viable geothermal system needs heat, porosity (void space in a rock), permeability (the ability to allow flow through the pores) and a fluid that can store and transport the heat. The temperature of the earth increases with depth while the porosity/permeability decreases with depth. If the reservoir has the right conditions, the heated fluid can be extracted and used. Once the heat is extracted from the fluid at the surface, the cooled water is re-injected into the reservoir in order to maintain the reservoir pressure. Geothermal energy can be subdivided in three categories, shallow geothermal, deep geothermal and ultra-deep geothermal. Where shallow geothermal is mostly used in combination with heat pumps which can provide both heating and cooling. Deep geothermal uses hot water stored in the subsurface of the earth from a depth between 1.5-4km and is now mostly used for direct use, and in some parts of the world for electricity generation, if the geothermal gradient is sufficient (near rift zones or volcanoes). Ultra-deep geothermal uses water from reservoirs at depths more than 4000m depth and is used for electricity generation because of the high temperatures at this depth (>100 °C). However, reservoirs at this depth often have very poor reservoir properties (porosity/permeability) due to compaction, cementation or the rock type which means that the heat cannot be collected and transported. In order to make these reservoirs economically viable, they can be stimulated in order to artificially increase the permeability. This is conventionally done by drilling more (horizontal) wells or by fracking, creating fractures around the borehole by injecting fluid with a very high pressure. This technique is expensive and can induce seismicity. Another stimulation technique is Radial Jet Drilling (RJD), which uses a focused high pressure water jet to create a small diameter (2-5cm) horizontal boreholes, called laterals, from a vertical well with a maximum length of 100m. It is a relatively cheap method which uses little water and does not induce seismicity.

If a reservoir is believed to be suitable for radial jetting (jettable rock type to connect the well with sufficiently productive parts of the reservoir), a nozzle connected to a hose is lowered in a vertical well using coiled tubing. The nozzle is deflected horizontally at the targeted depth using a deflector shoe. The nozzle normally has forward jet stream(s) and some backwards that provide the forward driving force of the nozzle (see in figure 1.1) in order to keep the weight on bit and propel the nozzle further into its own (horizontal)

borehole.

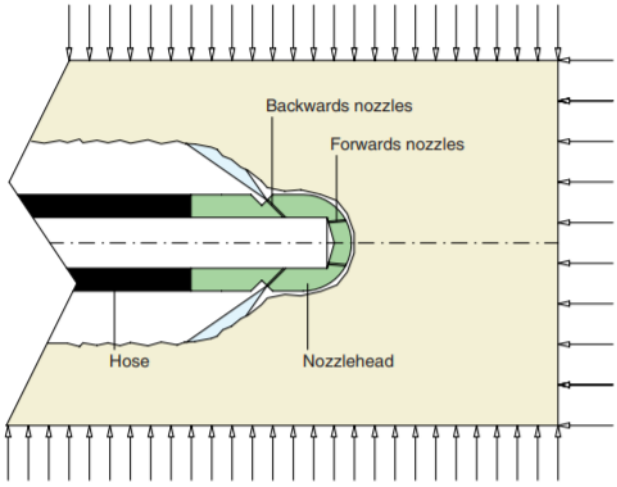

Figure 1.1: General nozzle design, forward jet streams and backward streams to propel the nozzle. (Buset et al., 2001)

RJD has already proved to increase the production in several oil and gas reservoirs with up to 7 times the initial production (Blöcher et al., 2016). For geothermal wells, simulations showed a potential production increase of 3-8 times if the conditions are favourable (homogeneous rock, well cab be connected to sufficiently productive parts, etc.)(Blöcher et al., 2016). This makes radial jet drilling a very promising technique for deep and ultra-deep geothermal applications. However, the jettability (ability to drill the rock with a water jet) of different reservoirs strongly differs, sometimes a jet can drill 100m in less then 15 minutes and sometimes it does not drill at all, mostly depending on reservoir rock properties and the local stress-field of the reservoir (Bakker et al., 2019). This highlights the importance of further research into this technique, where especially understanding the interaction between the rock and the jetted fluid is key. This project focuses on the destruction mechanism of the rock during impingement by a high pressure water jet. Understanding this process might help with the prediction whether a reservoir rock is suitable for the radial jetting technology. Four erosion mechanisms are proposed in literature, namely; cavitation erosion, surface erosion due to shear forces, fracture induction due to stagnation pressure and poro-elastic tensile failure (Buset et al., 2001). The four mechanisms might work simultaneously or there could be one governing mechanism. This study aims to further examine the mechanisms by conducting laboratory experiments on different sandstones, and performing numerical simulations where experiments were no longer possible.

In order to understand the destruction mechanism of a rock, it is important to first know what the exerted fluid pressure on the rock is (i.e, stagnation pressure). A stagnation pressure versus depth relation can also practically be used to find the optimum distance between nozzle and rock; getting too close to the surface does not work, while increasing distance decreases the required jetting pressure. The research objectives are formulated as follows:

- **What is the relation between stagnation pressure and cavity depth?** As the depth of the hole increases while the nozzle is not moving, the stagnation pressure (pressure exerted by the jet on the impinged surface, directly below the outlet of the nozzle) decreases due to (1) kinetic energy loss when penetrating a bigger water column which means less pressure at the cavity bottom and (2) the flow out of the created cavity experiences more resistance because of the increased friction area (the cylindrical cavity wall). Furthermore, as the cavity depth increases, the pressure fluctuations in the cavity are expected to decrease as well, because of the damping effect of the increased water column. If these pressure-depth relationships are developed, they can be compared with the rate of penetration in experiments, in order to find the optimum jetting distance between nozzle and rock.
- **What is the main erosion mechanism of a rock when impinged by a high pressure focused water jet?** Experiments were performed to investigate the *governing* destruction mechanism of multiple sandstones when impinged by a jet. Some experiments have the goal to disprove one of the proposed mechanisms, while other experiments try to prove another destruction mechanism, to eventually come to a conclusion of which destruction mechanism is the governing one. The first research question is needed in order to answer this main second research question because the pressures (fluctuations) at the cavity bottom are expected to be key in the destruction process.

Answering these questions will cause (1) a better nozzle design, because the distance between nozzle and rock can be optimised and (2) a better and faster prediction whether a reservoir rock can be jetted or not, saving both time and money.

2. Literature Review

2.1 Geothermal Energy

Geothermal energy is defined as the heat stored in the earth's crust. It originates from the formation of the earth and radioactive decay. It has been exploited for over a hundred years for electricity at an industrial scale (Chamorro et al., 2014), but has been used much longer for direct use (spas, medicine and minerals). With the new climate agreements set internationally, the play of geothermal energy will become more substantial and has already steadily increased over the past decades (Lund et al., 2011). Geothermal energy is an attractive solution because of its low carbon-emissions, reliability, low-cost and availability for direct-use as well as electricity generation (Goldstein et al., 2011). The potential for geothermal energy is quite high in Europe, especially for direct use from 2000m depth with temperatures between 60-80 °C (see figure 2.1a). But there is also some potential for ultra-deep geothermal (>4000 m) with temperatures of more than 100 °C, as shown in figure 2.1b, that can be used for electricity generation.

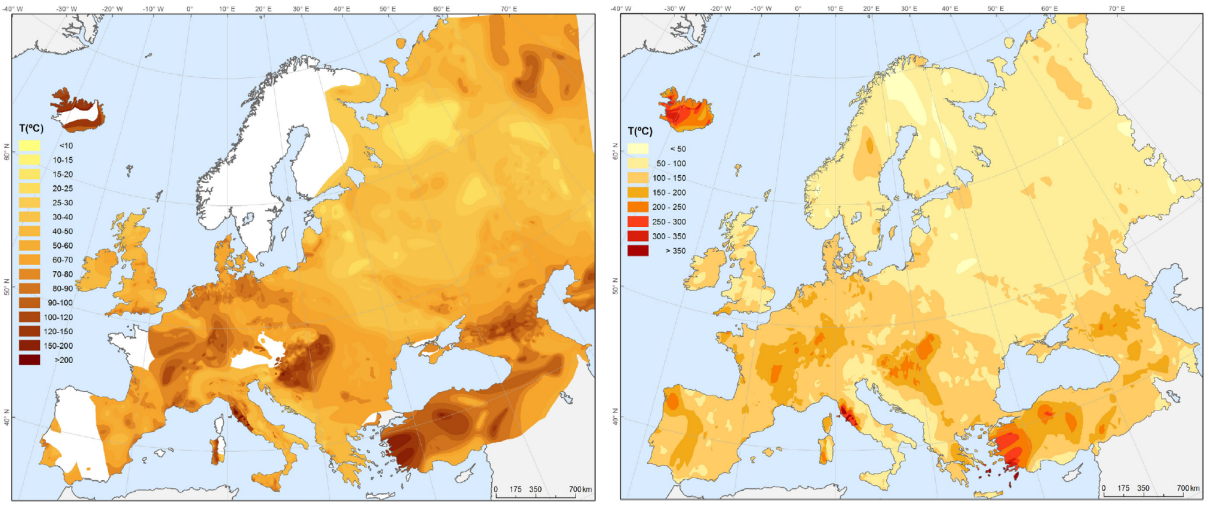

(a) Temperature at a depth of 2000m (Hurter and Haenel, 2002).

(b) Temperature in Europe at a depth of 4500m (Chamorro et al., 2014)

Figure 2.1: Potential of geothermal energy in terms of temperature at 2 and 4km depth in Europe for possible deep and ultra-deep geothermal exploitation

Different types of geothermal sources can be distinguished which are mostly dependent on the geological setting and depth in combination with the geothermal gradient (how fast temperature is rising with increasing depth). Wells in a vapour-dominated reservoir produce steam which can directly be used to feed a turbine in order to produce electricity (Moore and Simmons, 2013). Liquid-dominated reservoirs are more common and flow automatically as the liquid flashes into vapour in the wellbore as the pressure decreases towards the surface. These reservoirs exist near young volcanoes and rift zones (Moore and Simmons, 2013) and are also used for electricity generation. In most parts of Europe, direct-use geothermal is more common and uses the heated water from a reservoir to heat greenhouses or neighbourhoods and is then re-injected in the same layer after it is cooled down in order to maintain the reservoir pressure. The temperature in these types of reservoirs is usually between 60-100 °C (Lund et al., 2011). The last category is ultra-deep geothermal where basement rocks are targeted (or high very high temperatures at shallow depths, in some parts of the world). These rocks are commonly non-permeable which means that potential flow is dependent on existing fractures or induced fractures using hydraulic fracturing. These high enthalpy reservoirs that can be used for electricity generation are considered as enhanced geothermal systems (EGS) and don't need natural convective resources. These reservoirs are less dependent on the geological setting (Moore and Simmons, 2013).

Since both the temperature and pressure increase with depth, and the permeability decrease is proportional to pressure increase, high-enthalpy geothermal reservoirs often have poor porosity and permeability (Grant, 2013). So these reservoirs require engineered enhancements in order to be able to produce them economically. A well-known and controversial technique (especially in the oil and gas industry) is hydraulic fracturing, which means fracturing the reservoir with a high pressure (chemically) enhanced fluid. Another technique used in the oil and gas industry is a high pressure water jet which can drill as far as 100m horizontally from a vertical mother-borehole. The high pressure water jet is directed at the rock through a specially designed nozzle to generate and deepen a cavity. The general jetting technology as well as the nozzle design, the proposed erosion mechanisms and already performed experiments on this topic are further discussed in this chapter.

2.2 Radial Jet Drilling

Maurer et al. (1969) already proposed the use of a high pressure water jet to drill for oil in 1969. They found that the jet diameter and jetting pressure was critical for the rate of penetration (ROP). High pressure water jetting has a few advantages over conventional hydraulic fracturing as it uses very little water (only $1m^3$ (Blöcher et al., 2016)), is cost-efficient and has no environmental impact. Furthermore, it can potentially create new pathways to high-permeable zones, fractures or karst around the wellbore (Blöcher et al. (2016), Bruni et al. (2007)). A disadvantage of the jetting technology can be that the created horizontal lateral is not stable enough to stay open for longer periods of time because of the in-situ stress. Medetbekova et al. (2017) showed in a numerical study that both the hydraulic and thermal stresses lead to the closing of the jetted laterals. The lateral was mostly affected near the producer well, because the fluid pressure is lower near the wellbore (in order to let fluid flow from the lateral to the well), which means that the effective stress of the rock at that location

increases, resulting in a faster closure of the jetted hole. Also field cases showed sometimes a decline of the effectiveness of the jetted laterals over time (Ragab, 2013). Other limitations are that the nozzle cannot be directionally controlled during jetting, the nozzle can go into a different direction or terminate due to heterogeneities or fractures (Cinelli et al., 2013) and the cuttings cannot be analysed because they disappear in the well.

Radial jetting requires at first a "mother" borehole which is close to or in the main target formation. A diverter shoe is then placed in this well at the targeted depth which can guide the hose with the attached nozzle from vertical direction into the horizontal plane as shown in figure 2.2a. If the wellbore has a casing, this casing can be perforated prior to jetting using a casing miller. The nozzle with the attached hose and coiled tubing is then lowered into the borehole and through the deflector shoe. The pump at the surface will give the desired pressure and volumetric flow rate in order to start the jetting process. The drilled lateral has a diameter ranging from 25 to 50mm (Blöcher et al., 2016). After one lateral is drilled, the nozzle is retrieved to the surface and the diverter shoe is rotated and the process starts again in such way that multiple laterals are eventually drilled in different directions at the same depth in the well as shown in figure 2.2b.

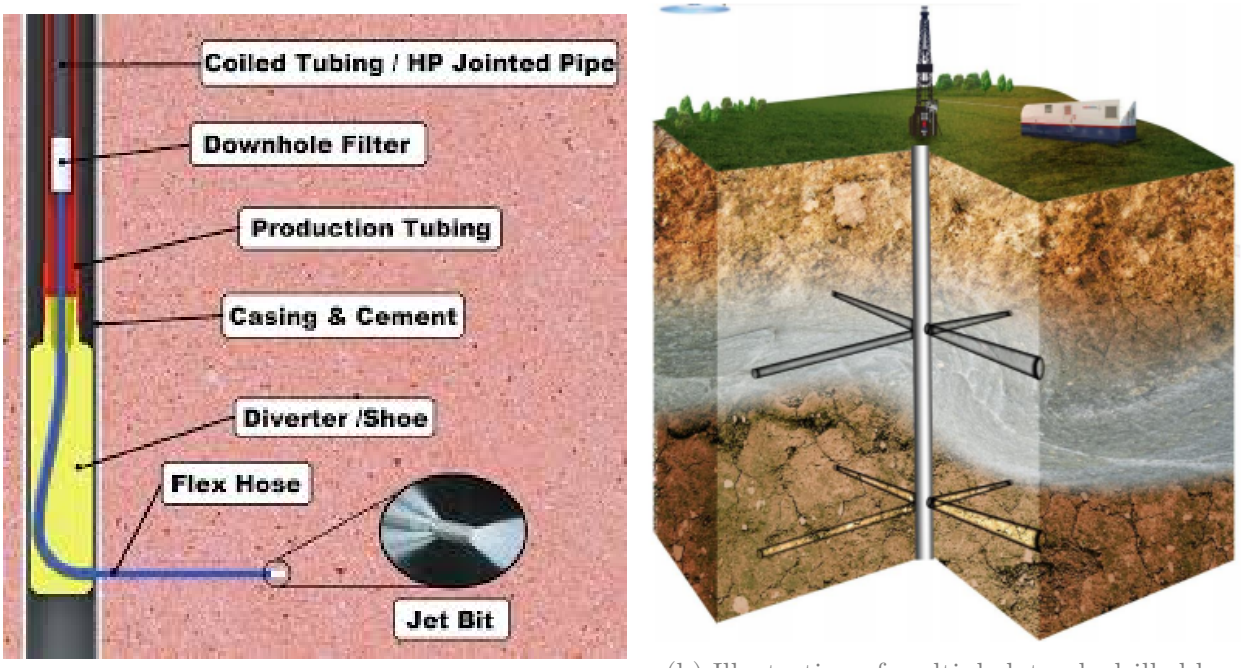

(a) Schematic illustration of the RJD technology downhole (Jun et al., 2018).

(b) Illustration of multiple laterals drilled by a water jet at multiple depths (target zones) in the wellbore (Peters et al., 2015)

Figure 2.2: Schematic overview of how the jet is deflected horizontally from a vertical well (left) and an illustration of multiple laterals at different depths of the well (right).

2.3 Nozzle Design

Since the design of the first nozzle by Maurer et al. (1969), it has been redesigned and modified with the results from experiments and numerical simulations in order to find the optimum nozzle with the highest ROP. The main distinction between types of nozzles that can be made to date is the "static" and "rotating" nozzle. The static nozzle has multiple jets forward and a few backward jets that serve the purpose of propulsion. The static nozzle creates a typical star-shaped borehole, as shown in figure 2.3b. The rotating nozzle has a nozzle-tip that turns with a high rotational speed, generated by the backward pointed jets that are drilled in an angle. The rotating nozzle has a few forwarding jets (not exactly in the middle), and creates a pattern as schematically shown in figure 2.3a. Experiments show that the rotating nozzle has a higher ROP than the static nozzles (Hahn and Wittig, 2017). However, static nozzles are preferred in the field, because the rotating nozzles have the tendency to get stuck in their own borehole (R. ter Veen (WSG), personal communication, January 31, 2019).

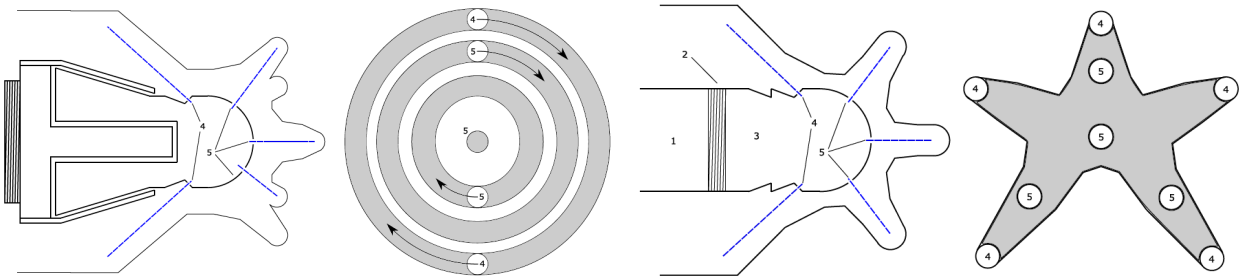

(a) Schematic design and erosion pattern of a typical rotating nozzle (Hahn and Wittig, 2017).

(b) Schematic design and erosion pattern of a typical static nozzle (Hahn and Wittig, 2017).

Figure 2.3: Design of a rotating (left) and static (right) nozzle and their resulting erosion pattern.

Apart from the distinction between a static and rotating nozzle, the location, angle and number of outlets of the jet itself can differ, depending on the application and type of rock. For experiments in the lab that have the objective to investigate the destruction mechanism of a rock, a static nozzle with only one forward jet is sufficient (Hahn et al., 2019). Nozzles can also be designed to be highly cavitating: the process where vapour bubbles are formed in the liquid because the pressure becomes lower than the vapour pressure of the fluid which usually happens where the direction of flow is suddenly changed (e.g. at a sharp edge)(see figure 2.4a)in combination with a high velocity flow. A cavitating nozzle can be useful to investigate the effect of cavitation erosion (the process where the formed vapour bubbles implode, damaging the material close to the implosion), and the impact location of this cavitation erosion (Hahn et al. (2019), Peng et al. (2018)), the process of cavitation erosion is further explained in section 2.6.2. Figure 2.4 shows the difference between cavitating nozzle and a conical non-cavitating nozzle, where it is clear that the nozzle in figure 2.4a has very sharp edges which results in the formation of vapour bubbles.

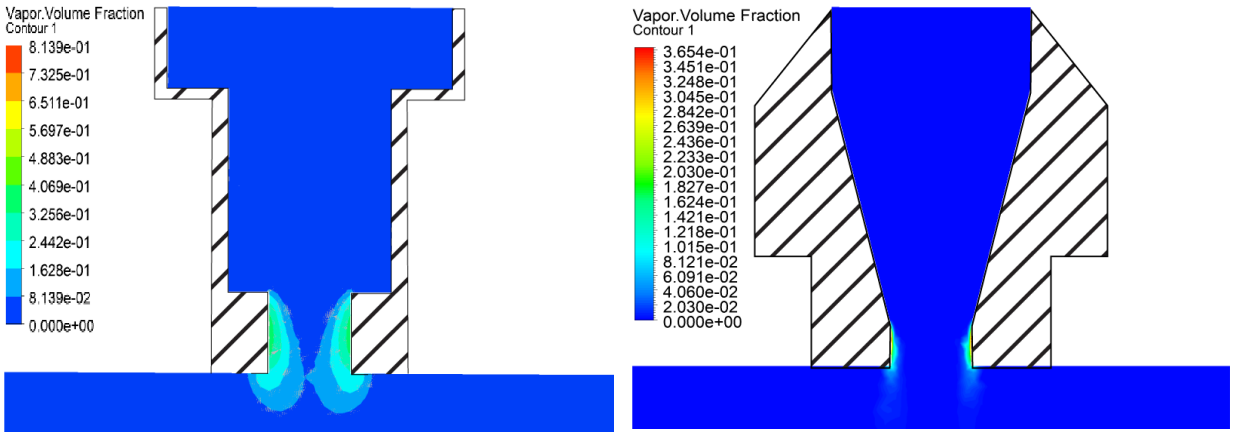

(a) Design of a cavitating nozzle, modified after Grant (2013). The sharp edges create pressure differences and local vacuums, resulting in cavitation bubbles.

(b) Design of a non-cavitating conical nozzle, modified after Blöcher et al. (2016). Almost no cavitation bubbles are generated by this conical shaped nozzle.

Figure 2.4: Illustration of a cavitating (left) and non-cavitating (right) nozzle. The coloured area represents the fluid body while the diagonal seamed area represents the nozzle. The simulations show the vapour generation of both nozzle designs, where the colour increase towards red means a higher vapour fraction. The flow rate is in both simulations the same (18L/min).

2.4 Velocity Measurements

Hahn et al. (2019) investigated the velocity field of water flowing through a cavitating nozzle similar to the one shown in figure 2.4a, jetting a flat aluminium surface with a stand-off distance of 5mm (the distance between the nozzle outlet and the impinged surface). The velocity field is measured using particle image velocimetry (PIV) that makes use of fluorescent particles which are in suspension in the jetting fluid that are photographed. The velocities of the water can be several hundred meters per second which makes this technique challenging. These experiments have to be conducted in a pressurised vessel in order to avoid cavitation bubbles (pressure in the cell $>$ vapour pressure of the fluid) which reflect light and would hence interfere with the fluorescent particles giving erroneous velocities. The Vessel has three windows; a laser creates a plane through two of the windows, and a camera is placed perpendicular to this laser plane to photograph the illuminated particles through the third window. The frequency of the laser and camera are very high and calibrated with one another in order to capture the particles that are moving with a very high velocity. Knowing the distance the particle has travelled from the photograph and the time between two pictures, one can establish the velocity of that particle. Tracking all the particles results in a velocity field. The velocity field of a jet hitting a flat aluminium surface with a nozzle outlet speed of 100m/s and a fluid pressure of 95 bar inside the vessel (i.e., backpressure) to avoid cavitation, is shown in figure 2.5 below. The point on the aluminium surface directly below the nozzle outlet (at radial distance 0 and axial distance -5.0 in figure 2.5) is called the stagnation point because the velocity is stagnating (i.e., velocity is (almost) zero). At the stagnation point the fluid pressure is the highest and called the stagnation pressure.

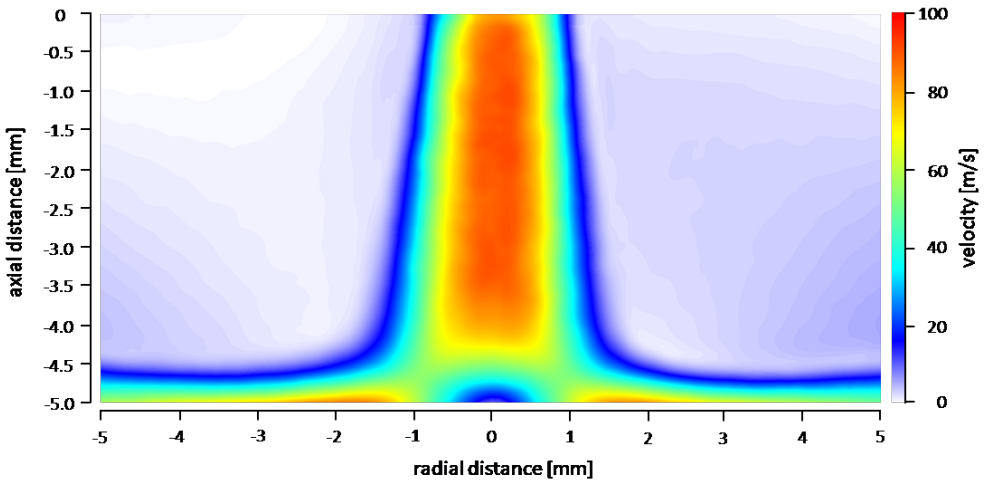

Figure 2.5: PIV measurement of a water jet with an exit velocity of 100m/s (flow-rate of 18L/min) and a backpressure of 95 bar (Hahn et al., 2019).

2.5 Rock Physics and Jetting Experiments

The sections above described the RJD technology as well as the nozzles, which are all parameters that can be changed. However, the rock that has to be jetted cannot be changed, which is why it is important to investigate the rock properties and their influence on the jetting potential. This section describes the general properties of rocks in terms of composition and strength and some jetting experiments that have been performed at atmospheric and stressed conditions from the literature.

2.5.1 Composition & Physics

The composition of a sedimentary rock is geologically speaking dependent on the parent rock (provenance). However, the rock can have gone through mechanical and chemical changes during burial (diagenesis), which may have altered the rock properties. Furthermore, the sorting of the grains can differ as well, which influences the porosity as well as the elastic properties of the rock. The strength of a rock is dependent on mineralogy, porosity, clay content and cementation (Sabatakakis et al., 2008). A Shale consists of relatively soft clay minerals, whereas a granite is composed of hard feldspars and quartz interlocked, which makes it a hard rock with no porosity. A clean sandstone consists mostly of quartz minerals bonded together with cement, but most sandstones contain may different minerals like clay minerals and feldspars. The most important properties of a rock are the Ultimate Compressive Strength (UCS), Ultimate Tensile Strength (UTS), porosity and permeability. Hahn and Wittig (2017) showed that the jettability of the rock is mainly dependent on the ultimate tensile strength (UTS), porosity and permeability.

2.5.2 RJD Experiments

Experiments with a high pressure water jet have been conducted at atmospheric (Hahn and Wittig, 2017) and submerged semi-reservoir conditions (Gradzki et al. (2018), Bakker et al. (2019)). Field tests show that the ROP increases downhole (R. ter Veen (WSG), personal communication, January 31, 2019), while experiments with an increased backpressure showed a decrease in ROP. Which seems contradicting as the pore pressure due to hydro-static pressure at depth is usually much higher than the pore pressure at atmospheric conditions.

Hahn and Wittig (2017) performed experiments with a high pressure water jet on multiple rock types under atmospheric conditions. They concluded that jetting of hard rocks is not possible under atmospheric conditions with a flow-rate of 20L/min and a bit pressure of 230 bar. Furthermore, the results showed that the jettability (ROP) of the rock seems to be mainly dependent on the porosity/permeability which is partly confirmed by the experiments that have been performed by Bakker et al. (2019). However, Bakker et al. (2019) also concluded that there is a dependency on the tensile strength. Table 2.1 shows the rock properties of three sandstones and their ROP from Hahn and Wittig (2017). It can be seen that the ROP of the Gildehaus sandstone is much higher than of the other sandstones where permeability of the Gildehaus sandstone is the only (favourable) property which is very different from the Bad Durkheim (BD). The UCS and UTS of the Gildehaus are even higher than that of the BD sandstone.

Table 2.1: Properties of three sandstones with their ROP (Hahn and Wittig, 2017). The Gildehuas sandstone has the highest ROP and a significant higher permeability while the UCS an UTS values are higher than of the Bad Durkheim sandstone.

Sandstone	UCS [MPa]	UTS [MPa]	phi [%]	k [mD]	ROP [m/h]
Bad Durkheim	30	2.9	19	0.45	0.46
Gildehaus	53	3.5	24	6.3	**4.28**
Dortmund	68	7.2	8	1.9*10^-5	0.25

It is known that a water jet performs better at reservoir conditions than at atmospheric experiments. The main differences between the reservoir and atmospheric conditions is the difference in stress and in pore-pressure. Bakker et al. (2019) found that the ROP increases in the direction of the lowest stress (σ_3). Field experiments in a quarry showed that the jet even follows the direction of lowest stress (Reinsch et al., 2018). Gradzki et al. (2018) also found that the ROP increased in sandstones when the samples were under "duo-axial" stress (cylindrical compressed). So if there are no tectonic stresses in a reservoir, the direction of the highest ROP would usually be horizontal as the maximum stress (σ_1) is in vertical direction due to the overburden of the overlying rocks at reservoir depths.

Furthermore, Bakker et al. (2019) investigated what the effect of a fracture is on the ROP. They found that the ROP decreased when a fracture was encountered. Even when the jet had passed the fracture, the ROP was lower than it was before encountering the fracture. This is explained by the fluid loss into the fracture, resulting in a lower stagnation pressure. The experiments were performed on a big block of sandstone (300 x 300mm) where they used a self-propelling nozzle. so the decrease in ROP after passing the fracture may have

been caused by the decrease of the weight on bit (WOB), as the backward jets were losing propelling force jetting into the fracture.

2.6 Destruction Mechanisms

If one wants to understand the destruction mechanism of the jetting technology, it is key to understand the interaction of the rock with the jetting fluid and associated pressure. In the literature, four destruction mechanisms were established over the years, these are discussed in this section. Some mechanisms are referred to as erosion mechanisms because they result in material erosion which leads to the destruction of the rock, eventually creating a cavity. The following mechanisms probably happen simultaneously, the question is only which one contributes the most. The four mechanisms can be subdivided into two groups; (1) porosity-independent and (2) porosity-dependent.

2.6.1 Surface erosion

This is the mechanism that results in material-erosion due to shear and compressional forces exerted on the surface by the high velocity flow of the high pressure water jet (Buset et al., 2001). This mechanism is independent of porosity, as it also occurs with non-porous materials. However, a higher porosity also results in a rougher surface which is more prone to surface erosion. It is assumed that this process takes place as there is flow along the rock's surface. The magnitude of the wall shear stress is, however, assumed to be too low compared to the effectiveness of a water-jet, it is hence unlikely that surface erosion is the governing destruction process (Buset et al., 2001). Also the location of the shear stress is along the walls instead of the cavity-bottom, therefore this process will widen the cavity.

2.6.2 Cavitation Erosion

Cavitation is the phenomenon in which vapour bubbles are formed in a flowing fluid. If the water accelerates to pass by the corners of the nozzle or when the water rapidly changes direction, the fluid experiences rapid pressure fluctuations locally, which may result in pressures that drop below the vapour pressure, creating a small cavity in the fluid filled with vapour. When the fluid including the bubbles move to an area where the pressure increases again, the bubbles implode (Buset et al., 2001). This implosion generates a pressure wave which might be as high as several hundred megapascals (Isay, 1989). Erosion of the material is caused by either one or the superposition of the following mechanisms: (1) Shock wave due to *symmetric* implosion of the bubbles, which means that the bubble remains spherical until the very end where the vapour is completely replaced by fluid again, and (2) the formation of micro-jets due to *asymmetric* implosion and collapse of bubble clusters (Momber, 2003). It is called *cavitation erosion* when the implosion results in material-erosion. The asymmetric collapse of a bubble, creating a micro-jet is shown in figure 2.6.

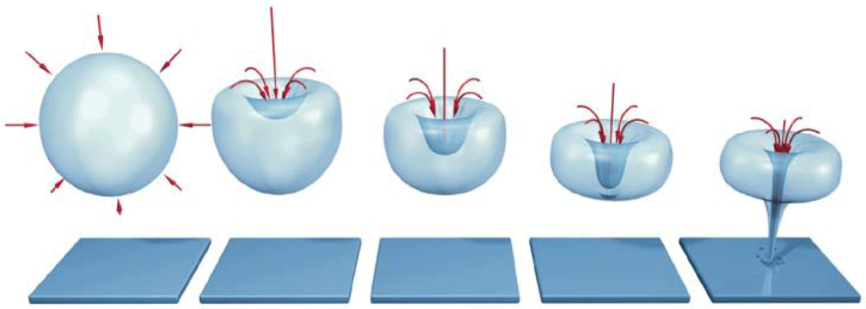

Figure 2.6: Schematic representation of an asymmetrical collapse of a vapour bubble forming a jet that erodes the surface (Ben Hamida et al., 2017)

Experiments have been performed by Hahn et al. (2019) to see where the cavitation occurred if a flat surface is impinged by a jet. In their experiments, the jet has a flow rate of 18L/min with zero back pressure (atmospheric). The stand-off distance is 5mm and the jet has a geometry as shown in figure 2.4a. The experiments consisted of two parts, (1) impinging a flat aluminium plate and (2) impinging a rock where the pores were filled with glue in the circular area where the jet hits the surface in a diameter of 5mm in order to investigate of this area was damaged by an porosity-independent mechanism. The experiment with the aluminium plate showed that the cavitation erosion occurred around the impinged area in a ring-like shape (see figure 2.7a) with an inner undamaged circular area of 5mm in diameter. The second experiment on a rock surface with the clogged area showed a similar pattern; the rock around the clogged circle was damaged by cavitation erosion whereas the glue-filled area stayed intact (see figure 2.7b). If shear forces or cavitation was the governing destruction mechanism, the glued area would have been damaged as well. When the same rock type was jetted, a hole with a depth of several centimetres was already created in a few seconds while the jetting time in the experiment (2) with the glue was 2 minutes.

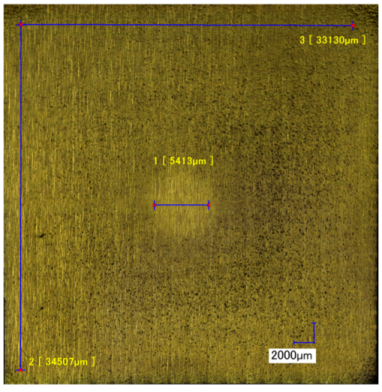

(a) Cavitation erosion on an aluminium plate, cavitation only occurred around the impinged area. Undamaged area has a diameter of 5.5mm

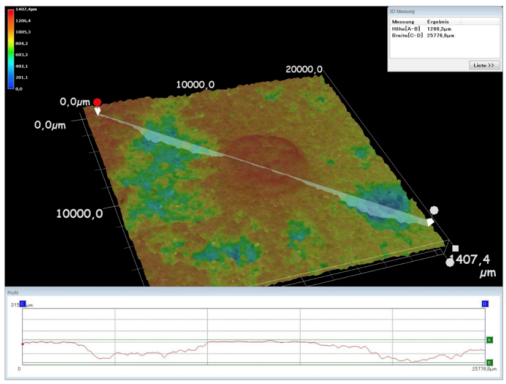

(b) Cavitation erosion on a rock sample with a clogged area of 5mm diameter

Figure 2.7: Result of cavitation experiments, the cavitation damage only occurs in a ring-like shape around the impinged area (Hahn et al., 2019)

Kumagai et al. (2011) performed numerical (CFD) simulations and experiments for a similar case. The cavitation number was calculated from the pressure and the flow from the CFD simulations. Although he used a lower flow velocity at the outlet (20m/s) and a bigger stand-off distance than Hahn et al. (2019), the results led to similar patterns. Figure 2.8a shows the erosion pattern of the experiment on an aluminium plate performed by Kumagai et al. (2011) and figure 2.8b shows the CFD simulations of the distribution where cavitation erosion could happen (erosion is the integration effect of time, and bubbles do not necessarily have to implode and cause erosion).

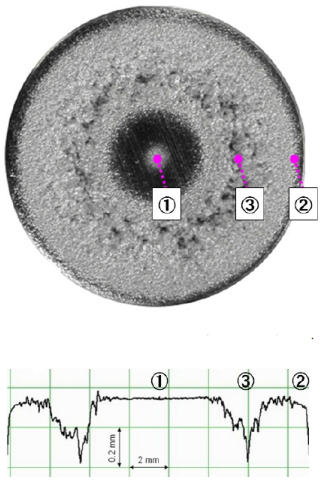

(a) Cavitation erosion on an aluminium alloy specimen cavitation only occurred around the impinged area.

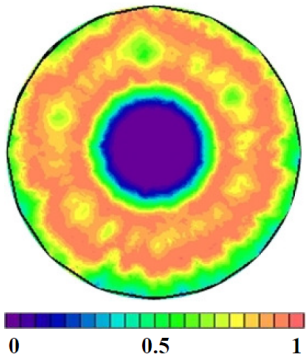

(b) Distribution of where cavitation could happen, calculated from CFD simulations

Figure 2.8: Comparison of an experiment with a CFD simulation of the location and distribution of cavitation (erosion) on an aluminium alloy specimen (Kumagai et al., 2011). The same ring-like shape can be seen as Hahn et al. (2019) found in their experiments.

Both studies prove that cavitation is not the governing erosion mechanism on a flat surface and hence in the first few milliseconds of jetting a rock as there is no cavity yet at this time. However, it does not prove that cavitation erosion is not happening inside a water-jet-created borehole.

2.6.3 Hydraulic fracturing

During jetting, the pores are locally, just below the stagnation point filled with high pressure fluid, a much higher pressure than the far-field in-situ pore pressures. Therefore the rock can fail in tension due to local pore pressure differences (see figure 2.9) (Buset et al., 2001). This mechanism obviously only occurs in porous rocks as it is fully dependent on porosity in order to work. As the area of increased pore pressure is as big as the area of impingement, this effect may cancel out due to the compression exerted by the jet (i.e. the grain is in equilibrium between the two fluid pressures). It is assumed that surface erosion actively enhances this process (Buset et al., 2001), because the wall shear stress on a grain has a force vector slightly

deviated (a high magnitude force parallel to the surface and a small force perpendicular), resulting in a small tensile stress (assumed that the grains leave perpendicular to the surface).

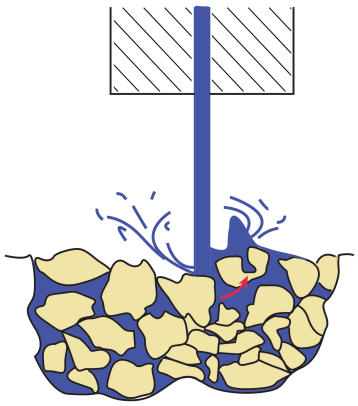

Figure 2.9: Hydraulic fracturing mechanism of a porous medium impinged by a high pressure water-jet (from the top in the above figure), modified after (Buset et al., 2001).Inthe picture, one grain is expelled, depicted by the red arrow, due to the high differential pressure between its pore and the pressure next to the jet (in the drawing).

Rehbinder (1980) tried to describe the erosion of a cutting jet (goal of a cutting jet is cutting material with a moving jet rather than drilling a hole) with hydraulic fracturing. Rehbinder (1980) approaches the rock cutting process in a theoretical manner. It was stated that the jettability of a rock depends on the erosion resistance and the threshold pressure (pore pressure at which the UTS in exceeded). The erosion resistance is described by the ratio between the average grain size and the permeability, the higher the permeability the lower the erosion resistance. The threshold pressure is measure for the ultimate micro-scale tensile strength of the rock. The theory of Rehbinder (1980) concludes that the jettability is highly dependent on grain size (permeability); the smaller the grain size (lower porosity), the higher the tensile strength threshold and thus the lower the jetting potential.

2.6.4 Poro-elastic Tensile Failure

Induced tensile stress might occur if the pore pressure decrease at the surface becomes higher than the effective stress and tensile strength of the rock at that point (Buset et al., 2001). This tensile stress occurs if the compressibility of the rock and the pore fluid is not equal. The equilibrium between grain and pore fluid must be retained by flow trough the pore space. This needed flow through the pore-throat in order to reach equilibrium takes time, resulting in a poroelastic effect (Buset et al., 2001). So this effect can only occur in a permeable rock and is thus porosity-dependent. However, if the permeability is too high (<1 Darcy), this effect can no longer occur, because the equilibrium is retained too fast according to Buset et al. (2001).

3. Methodology

This chapter presents the methodology and the experimental setup used in this project. The experiments were conducted with the aim of investigating the maximum jettable depth of multiple sandstones, the effect of a fracture during jetting, the influence of backpressure and finally the location of cavitation erosion. When experiments were no longer feasible due to the costs of material or the time frame of this thesis, numerical simulations were carried out in order to approximate the jetting process. 3D simulations were conducted in order to find the relation between pressure (fluctuations) and cavity-depth. Furthermore, a 2D Darcy-flow solver was developed to examine the pressure distribution in a porous sample, which is coupled to the pressure-depth simulations later on. This chapter firstly presents the experiments and simulations aimed to find pressure-depth relationships, followed by the experiments and simulations that investigate the destruction mechanism. The last section of this chapter presents the proposal of an analytical correlation which predicts whether a rock is jettable or not and what the maximum jettable depth is, based on the findings of the experiments, simulations and literature. The experiments conducted beforehand will validate whether this correlation is correct, and how accurate it is. Hence the correlation combines the erosion mechanism and the pressure-depth relationship.

3.1 Pressure-Depth Relation

This section presents the methodology for the experiments and simulations conducted to understand the relation between pressure and cavity depth. The jetting experiments were performed at atmospheric conditions and were mainly conducted to investigate the maximum depth of jetting and the influence of fractures during jetting. Three different sandstones with varying material properties were chosen for these experiments. These sandstones were chosen as to their fast preparation and short experiment duration.

As a static nozzle drills a cavity, the jetting water has to be pushed out of the hole which reduces the pressure exerted on the bottom of the hole (i.e, stagnation pressure). The water column in the created cavity has a damping effect on the pressure as well. So the stagnation pressure as well as the pressure fluctuations are expected to be less intense as the cavity depth increases. The stagnation pressure at the bottom of the jetted cavity versus its cavity depth, with a **static nozzle**(distance between cavity bottom and nozzle increases during jetting, and only one forward jet), is key to understand, because this can potentially provide the optimum stand-off distance of a water jet. However there is no analytical solution for the pressure loss in turbulent flow including back-flow inside a cavity. This problem should

therefore be solved experimentally or numerically.

A setup was designed which had the purpose of measuring the pressure at the cavity bottom during impingement of the jet (the design of the setup can be found in chapter 6). However, the specifications of the pressure sensor were too demanding and hence too expensive. The problem is therefor solved numerically with the *Ansys Fluent* software. The combination of the simulation results with the experiments can give information about the pressure (from simulations) at which the jetting ceased (from experiments).

3.1.1 Samples

As mentioned before, this study focuses on the destruction mechanism of sandstones. Three different sandstones were chosen for the experiments; the Triassic Bad Durkheim sandstone, the Cretaceous Gildehaus sandstone and the Dortmund sandstone from the Carboniferous. The properties of these three sandstones are listed in table 3.1 below.

Table 3.1: Properties of the three sandstones used in the experiments.

Sandstone	**Age**	ϕ **[%]**	**k [mD]**	**Poissons ratio [-]**	**UCS [MPa]**	**UTS [MPa]**	**KI [MNm$^{2/3}$]**
Bad Durkheim	Triassic	19.5	450	0.26	30	2.9	0.6
GildeHaus	Cretaceous	23.7	6300	0.27	53	3.5	0.4
Dortmund	Carboniferous	8.7	0.018	0.12	68	7.2	0.8

As the experiments have the final aim of providing insights in the erosion mechanism, the ideal rock type would be an homogeneous rock because then the results would be independent of local changes in rock properties. The Bad Durkheim has a high level of homogeneity and is therefore used the most in this study. The Gildehaus sandstone has proved to have the highest ROP among these three sandstones (Hahn and Wittig, 2017), which is why it was also chosen for the experiments. The Dortmund sandstone has a much higher UCS an UTS and a much lower porosity and permeability than the other two sandstones, which makes it an interesting rock for comparison. However the Dortmund sandstone is relatively heterogeneous making it hard to draw conclusions from the results as properties may locally change drastically.

In this study 55mm diameter cores were used. This diameter is chosen such that the samples are strong enough to prevent them from fracturing due to the high impact of the jet while being small enough to use material efficiently. The cores were cut in a length of 50mm, because it was not expected that the water jet drills further than 40mm. Hahn and Wittig (2017) showed that the saturation of the rocks has a big effect on the jetting performance; the lower the saturation, the lower the jettability. The samples were therefore fully saturated with water before usage in the experiments, to avoid saturation effects in the results.

3.1.2 Experiments

The experiments that were designed to determine the pressure-depth relation were conducted at atmospheric conditions. Four types of experiments were performed; (A) jetting on a blank rock surface, (B) jetting a rock with a pre-drilled cavity, (C) jetting a rock with a sealed aluminium adapter on top, and (D) jetting a rock with an aluminium adapter which was *not* (completely) sealed. Every different test (varied jetting time, stand-off distance etc..) was repeated three times to decrease the measuring error and possible heterogeneity's in the samples. A schematic representation of these experiments is shown in figure 3.1. The four different types of experiments are further explained in this section.

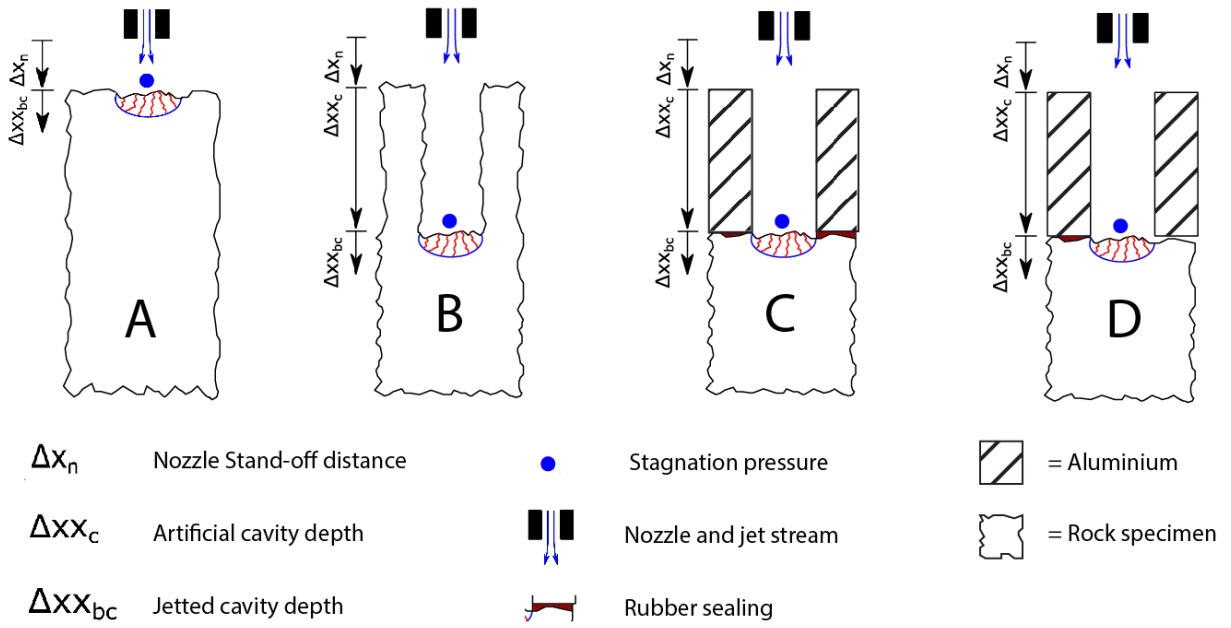

Figure 3.1: Illustration of four experiments performed on three different sandstones. (A) jetting on a black rock surface, (B) jetting on a rock with a pre-drilled hole of $\varnothing = 8$mm, (C) jetting on a rock with a sealed aluminium adapter with an $\varnothing = 6$mm hole and (D) jetting a rock with a non-sealed aluminium adapter on top, creating an artificial fracture.

The experiments were performed at atmospheric conditions. A stand as shown in figure 3.2 with an adjustable static nozzle and a sample holder were placed in a small aquarium filled with water such that the nozzle and the sample are submerged. The samples were placed in the stand and pressed by an aluminium plate which is connected to the bottom of the stand (depicted as (4) in figure 3.2a). The high pressure hose is attached to the stand and further connected to a static nozzle (number 1 in figure 3.2a). The distance between the nozzle and the rock (stand-off distance) can be adjusted. Figure 3.2 below gives a schematic overview of the setup and a photo. The pump, connected to the nozzle with a high pressure hose, can give a maximum pressure of 280 bar. The pump pressure for the experiments in this study was 160 bar, which resulted in a flow rate of 28L/min and a nozzle-outlet velocity of 160 m/s.

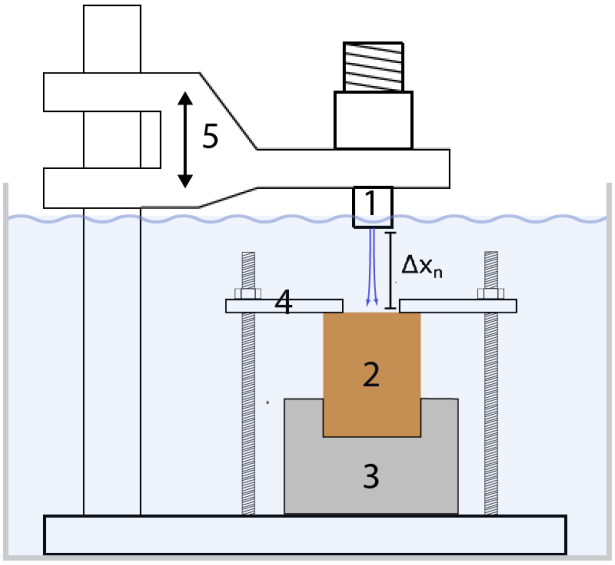

(a) Schematic sketch of the setup for the proposed experiments. (1) is the nozzle, (2) is the rock sample, (3) is a sample holder, (4) is a clamp to fix the rock sample and (5) is the holder which holds the nozzle and can be moved up and down to change the stand-off distance X_n.

(b) Photo of the setup. A rock sample is compressed with an aluminium adapter on top (experiment (C)).

Figure 3.2: Illustration of the setup used for the four experiments proposed before and illustrated in figure 3.1.

Blank Rock Surface (A)

Several tests have been performed on a plain rock surface in order to measure the penetrated depth of the used rock type at different jetting times. Rocks were jetted for 10s, 30s and 300s. This was done to investigate at what time the maximum jetting depth was reached, where the 300 seconds case was assumed to result in a maximum cavity depth. The stand-off distance (Δx_n) of the jet was also varied from 5 to 30mm, in order to see if the jet would loose considerable jetting power (i.e, stagnation pressure on the rock).The created cavity depth and width were measured after the experiment.

Rock with Pre-Drilled Hole (B)

In order to see the effect of pressure loss due to the drilled hole itself, rock samples were pre-drilled with a 10, 15, 20 and 25 mm deep hole with a diameter of 8mm (comparable to the width of a jetted hole). The pre-drilled cavity has the advantage that it is a perfect cylinder, which makes it easier to compare with simulations (where a perfect cylinder is modelled). Pre-drilling a hole with a drill before jetting is also convenient because the different tests

can be compared more accurately, because the geometry of the borehole is the same in every experiment. The depth of the cavity as well as the roughness of the cavity wall influences the pressure loss at the cavity bottom. As the pre-drilled cavities still had different friction factors due to heterogeneity of the rock, it was decided to make an aluminium adapter with a hole that has the same properties in every experiment. Experiments with such an adapter are discussed in the next section (Experiment (C)).

Sealed Aluminium Adapter (C)

Aluminium adapters (see figure 3.3) were manufactured with a pre-drilled hole of 6 and 8mm in diameter and various thicknesses ranging from 25mm to 50mm to investigate the where the jetting ceases. The adapter is placed on top of the rock sample and is sealed with a rubber (see figure 3.1 (B)). These tests were performed to investigate the effect of the pressure loss due to cavity depth (similar to experiment (B)). The advantage of the aluminium adapter is that the friction is lower and remains the same, unlike the similar experiments with a pre-drilled cavity (B). This makes the comparison with simulations more accurate. The aluminium also takes away the effect of the permeable cavity wall. The experiments with the pre-drilled hole (B) had a permeable wall which is very hard to simulate numerically because flow is dependent of pressure which varies constantly inside the cavity due to turbulence and pump pressure fluctuations.

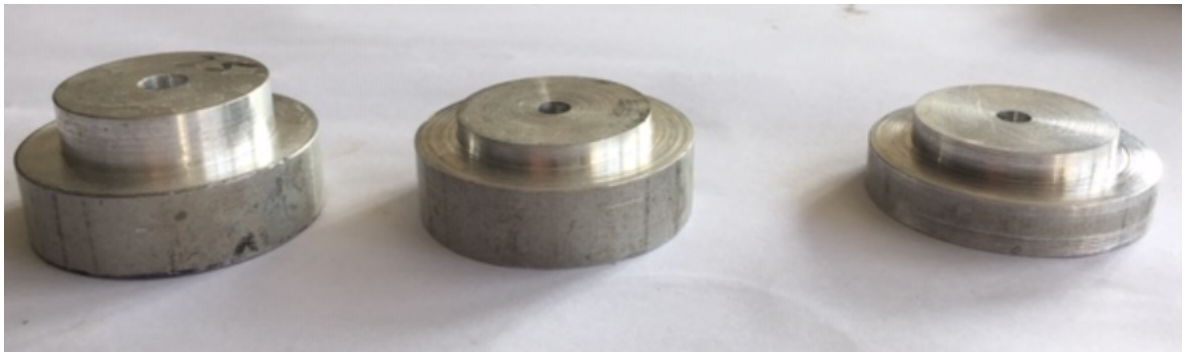

Figure 3.3: Three aluminium adapters with a drilled hole. They were used to put on top of a sandstone sample to consistently create an "already" jetted (artificial) cavity.

Adapter with Artificial Fracture (D)

In the previously described experiment (C), the rubber that was supposed to seal the aluminium on the rock was sometimes blown out, causing a local pressure relief between the rock and the aluminium disc. This pressure relief resulted in a higher stagnation pressure on the cavity bottom of the rock. So when the rubber was non-sealing, the jet was able to drill further than experiments with a proper seal. With this result, it was decided to make another set of experiments where the rubber was partly cut, creating a pathway for the fluid to escape the borehole. If a jet hits a fracture, the same pressure relief can occur if that fracture is open, so by creating this pathway, an artificial fracture was created. This is interesting to compare with the findings of Bakker et al. (2019), who also investigated jetting across a fracture.

3.1.3 Simulations

The computational fluid dynamics (CFD) simulations were carried out in *Ansys Fluent* with the goal of obtaining a correlation between the (average) stagnation pressure (P_s) and the cavity depth. Furthermore, the pressure fluctuations at the cavity bottom can be obtained from these simulations. It is assumed that these pressure fluctuations (resulting in pressure differences between pores) are necessary to remove material, as discussed earlier in section 2.6.3. It is also expected that the pressure fluctuations are small during the first millisecond (still a flat rock surface) and increase with depth as the turbulence intensity is expected to increase up to a certain depth where this turbulence and thus the fluctuations decrease again due to damping effects of the higher water column. Different turbulence models were compared with the PIV measurements on a flat surface (see section 2.4). The different geometries, the meshing procedure, the physics (turbulence models) and the boundary conditions for these simulations are discussed in this section.

Geometry

For the *Ansys* simulations, *only* the water body is modelled. First, a geometry was made that is used for comparison of the results with the PIV measurements. The PIV measurements were conducted in a pressurised vessel called the "mini-iBOGS". Secondly, geometries of the water bodies were made with an increasing cavity depth that serve the goal of modelling the pressure versus depth relationship. Both tpes of geometries are discussed below.

Mini-iBOGS Geometry

The geometry of the mini-iBOGS model is shown in figure 3.4. As the nozzle used for the PIV measurements is highly cavitating (see figure A.1 in Appendix A), the fluid body in the nozzle is also part of the geometry as it might influence the results when simulating multi-phase fluid flow (cavitation). The fluid domain above the surface which is impinged, is 20mm in diameter. The height of the fluid body is 5mm (stand-off distance). The fluid body is smaller compared to the actual fluid body in the mini-iBOGS, but most of the physics happen in the jet region and close around this region. So it was decided to model only this small part to save computational time.

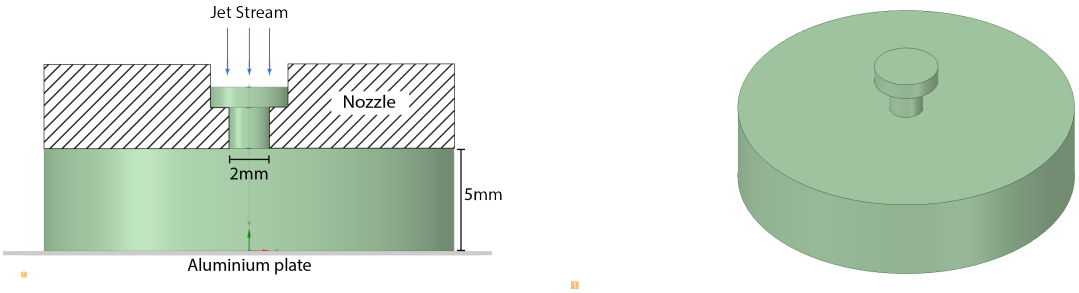

Figure 3.4: Geometry of the water body used for further simulations of the jetting process in the mini-iBOGS. The top part is the water inside the nozzle, which is taken in to account because of the cavitating nature of the nozzle design.

Cavity Geometry

The geometry of the cavity is modelled as a simple cylinder (cavity of the rock) attached to the fluid body between the rock and nozzle (see figure 3.5). Multiple models were made with a cavity depth ranging from 0 to 40mm, with increments of 5 mm or smaller where needed. The standoff-distance is again 5 mm, and the radial distance from the jet axis to the outflow is 10mm resulting in a circular disk with a diameter of 20mm and a height of 5 mm. The inlet of the water body (outlet of the nozzle) is again 2mm in diameter. The diameter of the cavity is 6mm (comparable to a jetted hole), but some additional models were made with a diameter of 8mm in order to compare them with laboratory experiments (B) described in section 3.1.2. A few cross-sectional geometries of different depths (5, 15 and 40mm) are shown below in figure 3.5. The Blue part in these figures represents the fluid body. The nozzle (seamed lines), the jet stream (blue arrows) and the rock (yellow part) are only drawn around it for clarity.

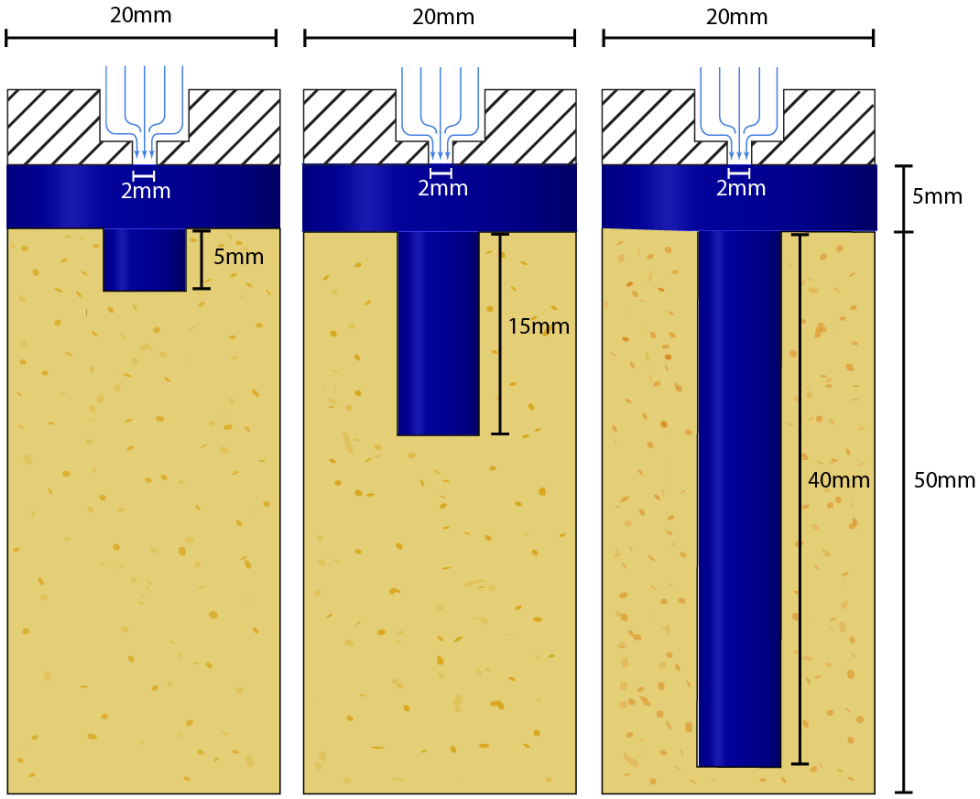

Figure 3.5: Cross-sectional view of the fluid body (in blue) with different cavity depths (5, 15 and 40mm from left to right) which are used for the simulations. The rock (in yellow) and the nozzle (seamed lines) are shown as well for clarity.

Meshing

In numerical simulations, the geometry is subdivided in small discrete elements, this process is called meshing. The smaller the mesh, the more accurate the solution becomes. In this study, a tetrahedral mesh is used. As discussed before, the academic version of the *Ansys*

licence has a limit of 512k elements. In order to give the jet region the smallest element size, the geometry (discussed above) was narrowed down to only the part where the velocity of the fluid will be the highest. For the simulations on a flat aluminium surface (mini-iBOGS), the mesh near the surface was refined (inflated) 15 times with a growth rate of 1.2 in order to simulate the near-wall region as accurate as possible (see figure 3.6a). The simulations with a cavity have a finer mesh inside the cavity, no inflation layers were used because the exact solution in the near-wall region is less important than the eddy's inside the cavity. A crossection of both the mini-iBOGS model and one of the cavity meshes are shown in figure 3.6.

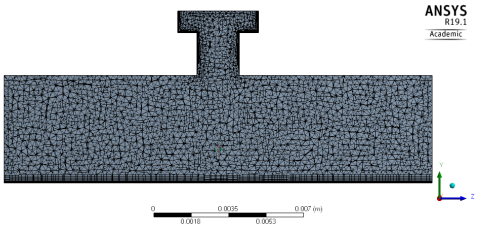

(a) Mesh of the water body used to simulate the jetting in the mini-iBOGS. The near-wall region is refined in order to maximise accuracy in that region. The water body of the nozzle is also taken into account because of its cavitating nature.

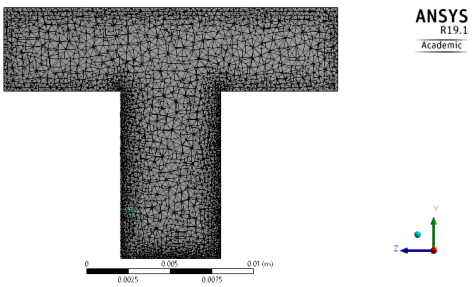

(b) Mesh of one of the cavity-models. The mesh is finer in the cavity because the turbulence will occur there.

Figure 3.6: Cross-sectional view of the mesh of the mini-iBOGS model and the cavity models (10mm cavity depth).

The quality of the mesh is important for the convergence of the final solution. There are different indicators for the mesh quality which can be calculated before running simulations. The aspect ratio of a cell should not be to high (<5:1, except for boundary layers) in order to avoid divergence of the solution, the Jacobian ratio, which is the ratio between the element geometry and the perfect (theoretical) element geometry, should be lower than zero. Furthermore, the average skewness, which is the defined as the difference in shape between a cell and an equilateral cell with the same volume, should not be higher than 0.95. If these quality indicators were not met, the mesh was refined or changed at the corresponding location. After meshing, the model needs to be set up in terms of physics (i.e, turbulence models), boundary conditions and methods used to solve the problem

Physics

There are many correlations used to solve turbulence flow problems, which all serve different purposes. In this study, three different models are used, namely:

- $k - \epsilon$
- $k - \omega$ with shear stress transport (SST)
- Delayed detached Eddy simulation (DDES) with the shear stress transport (SST) $k-\omega$

Where k is the turbulence kinetic energy, ϵ the rate of kinetic energy dissipation and ω the rate of dissipation of turbulence kinetic energy into thermal internal energy. The three models have been compared to each other in order to choose the best solver. The $k-\epsilon$ model is a two-equation turbulence model which is especially helpful for solving the physics near the walls, but is not accurate enough for solving eddy's in the fluid body far away from the walls and is therefore not applicable for simulating the jetting process.

The $k-\omega$ model is also a two equation turbulence model which accurately solves the inner part of the water-body, it is a closure of the Reynolds-averaged Navier-Stokes (RANS) equation. Adding the shear stress transport (SST) to this model combines the best of two worlds as the SST models the near boundary regions and the $k-\omega$ model simulates the inner regions. However, this model is unable to accurately simulate high Reynolds numbers. The simulation of a high pressure water jet has significantly high velocities and therefore high Reynolds numbers.

The third model is the Delayed Detached Eddy Simulation (DDES) in combination with the $k-\omega$ - SST model. This model is a modification of the RANS model that switches to a sub-grid scale formulation fine enough for a Large Edyy Simulation (LES) model. Near- wall regions with a turbulence length smaller than the element size are solved using the RANS model. The DDES in combination with the SST $k-\omega$ model is used for the simulations is this study. The mathematical description of these models are presented in Appendix B on page 79. Having the physics setup, the boundary conditions can be defined.

Boundary Conditions

Every face of the geometry has its own boundary condition. There is an inlet, outlet and walls. There are five different boundary conditions in the conducted simulations. Figure 6.2 depicts the 3D geometry with the numbered boundaries. The boundary conditions are as follows:

1. The inlet, which is the outlet of the jet. The inlet is controlled by velocity. The mean velocity is either 106 m/s (for the mini-iBOGS simulations) or 160 m/s (for cavity simulations). The pump pressure feeding the nozzle fluctuates due to the pistons of the pump, resulting in a fluctuating outlet nozzle-outlet velocity. These fluctuations are considered in the simulations and are discussed further below.

2. The outlet (number 2 in figure 6.2). This boundary is controlled by pressure, which was atmospheric in most simulations, except for the mini-IBOGS simulations where it was 95 bar.

3. Wall of the nozzle (number 3 in figure 6.2). The interface of the water body with the wall of the jet. A friction coefficient of 0.00015m.

4. Wall of the rock (number 4 in figure 6.2). This is the interface of the water body with the rock, with a friction coefficient of 0.0025m.

5. Bottom of the cavity, which is a wall as well as an outflow (number 5 in figure 6.2). The outflow is dependent on the cavity depth and pressure as it is calculated with the Darcy-flow equation. The outlet boundary condition is further discussed below.

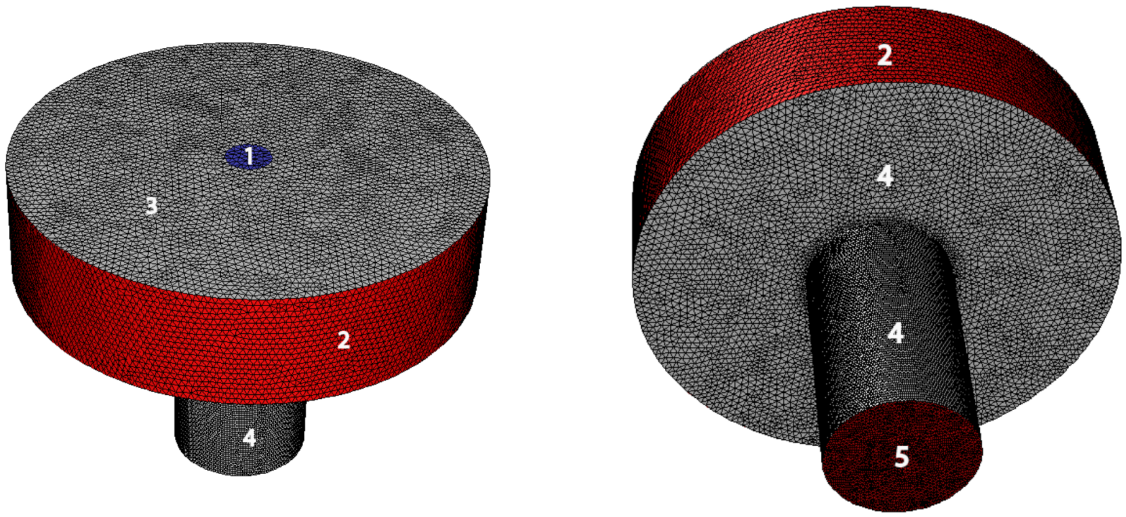

Figure 3.7: Boundary conditions of the model. 1: the velocity at the inlet (outlet of the nozzle), 2: pressure outlet, 3: the wall of the nozzle, 4: the wall of the rock and 5: a porous wall with a mass-outflow, controlled by Darcy flow.

As the pump of the water jet has pistons which generate the pressure, the pump pressure is not constant but has small fluctuations (pressure drops between piston stages). This also results in fluctuations in the velocity at the outlet of the nozzle. So the inlet of the water body is also not constant. To account for this effect, a function was given for the inlet velocity of the model. The mean velocity for the cavity simulations is set at 160 m/s with an amplitude of 5m/s and a frequency of 60 Hz. The inlet velocity over time is shown in figure 3.8 below.

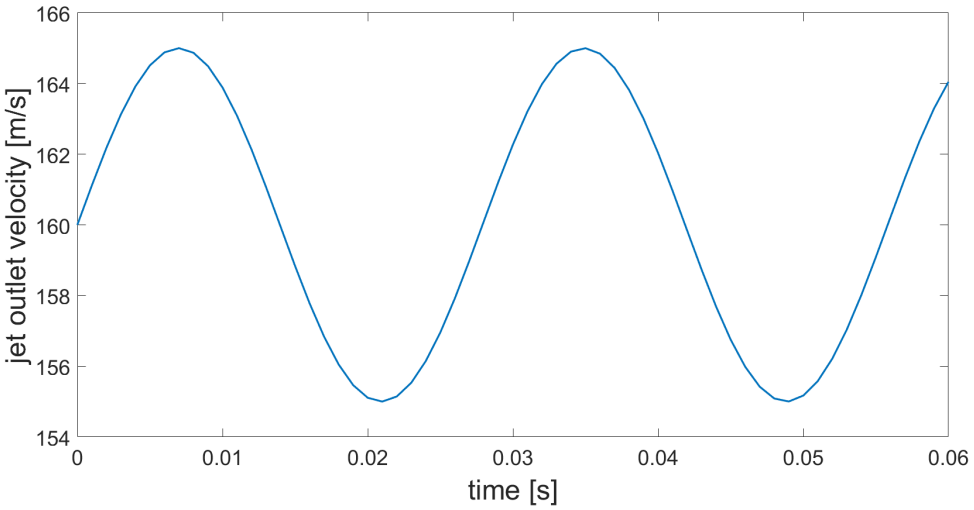

Figure 3.8: Velocity at the inlet (outlet of the nozzle). The fluctuations are a result of the pump which is used for the experiments.

The bottom of the cavity (number 5 in figure 6.2) is also an outflow (to the porous medium) controlled by the mass outflow in kg/s. A pure pressure dependent porous rock

would cost too much computational time and does not add much value to the final solution of the simulation. So the simulations were run without a transient pressure-dependent porous outlet, but with a constant mass outflow porous outlet which was calculated with the Darcy equation (equation 3.1). The pressure used for the calculation of the flow was determined in an iterative manner; first a simulation was run that had no porous outflow on boundary 5, with this pressure at the cavity bottom, the flow was calculated. Then the simulation was run again, but now with the calculated outflow, resulting in a different pressure at the cavity bottom, which was then used for calculating the outflow again. This was repeated until the pressure of the new simulation was (almost) the same as the previous simulation. The computed pressure is then further used to calculate the flow using equation 3.1 (Darcy). The resulting flow versus depth correlation as well as the pressure at the cavity bottom is shown in figure 3.9. As can be seen in figure 1.8, the pressure of the jet is significantly high when the cavity is shallow, resulting in a higher flow rate. Moreover, the pressure of the jet decreases when the cavity depth increases. The length between the cavity bottom and the bottom of the rock sample (ΔL) however decreases with increasing cavity depth, which also results in a higher flow rate from the cavity bottom to the bottom of the rock sample.

$$Q = \left(\frac{kA}{\mu}\frac{\Delta P}{\Delta L}\right) * \rho \tag{3.1}$$

Where
$Q = Flow\ in\ kg/s$
$k = Permeability\ in\ m^2$
$A = Area\ in\ m^2$
$\Delta P = Pressure\ difference\ between\ cavity\ bottom\ and\ bottom\ of\ the\ rock\ sample\ in\ Pa$
$\mu = Viscosity\ in\ Pa \cdot s$
$\Delta L = Length\ from\ cavity\ bottom\ to\ bottom\ of\ the\ rock\ sample\ in\ m$
$\rho = Density\ of\ water\ in\ kg/m^3$

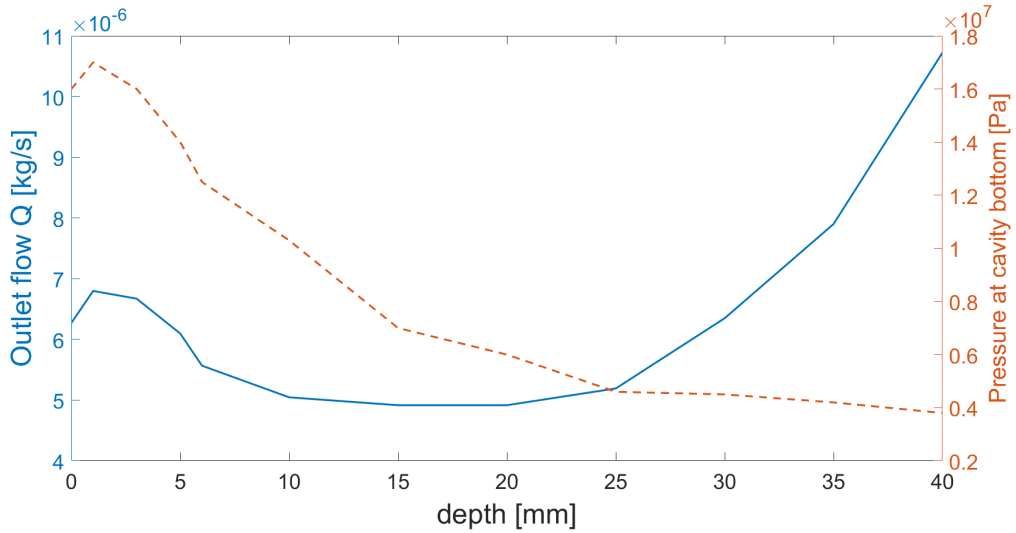

Figure 3.9: Pressure at the cavity bottom (right axis) and associated mass flow through the cavity bottom (left axis).

Solving Methods & Convergence

The simulations are solved in a transient manner using a time-step of 0.001 seconds with 50 steps. The transient numerical formulation was bounded second order implicit in a coupled scheme which improves accuracy and stability (disadvantage is longer computational time) compared to first order methods. The residuals of the calculations can be monitored to check the convergence of the solution. A Residual is the difference between a solution of a current iteration and the previous iteration, this value should decrease or at least not increase (diverging). The residuals for one of the simulations is shown in figure 3.10. The peaks are associated with a jumping to the next time-step. Then in every time-step, the calculations are iterated until they meet their convergence criterion.

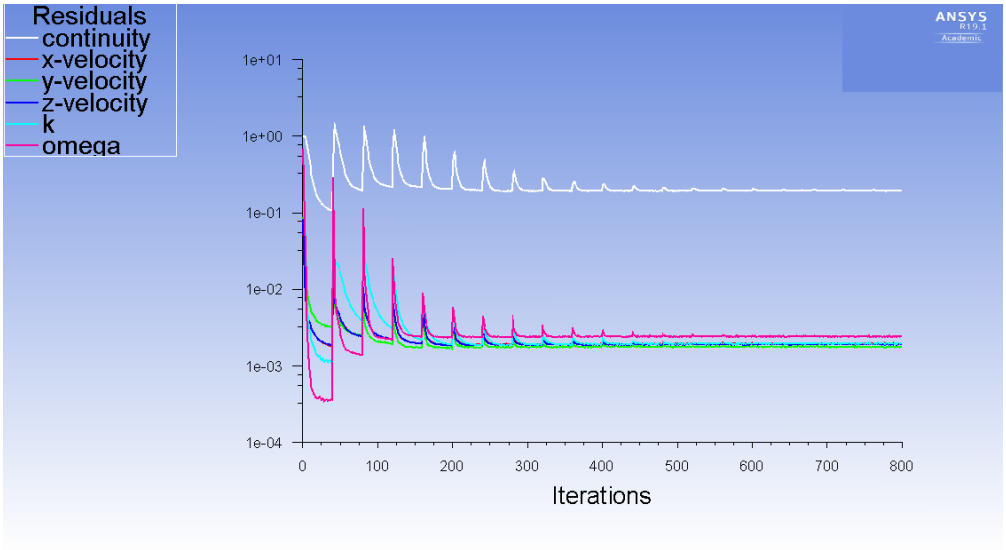

Figure 3.10: Residuals (error in the results) for one of the simulations (10mm case). The residuals should be either decreasing or stay constant. The spikes occur due to the jump to the next time-step.

3.2 Erosion Mechanism Experiments & Simulations

In order to acquire a better understanding on which of the four proposed destruction mechanisms is the governing one during jetting of a sandstone, experiments and simulations were carried out. This chapter presents the steps undertaken during the conduction of the experiments and during setup of the simulations. As stated before in section 2.6, the four proposed mechanisms are are: surface erosion due to shear forces, cavitation erosion, fracture induction due to stagnation pressure and poroelastic tensile failure. Buset et al. (2001) already stated that surface erosion due to shear force is most likely not the governing erosion mechanism. Hydraulic fracturing and poro-elastic tensile failure are interconnected as they both depend on pressure fluctuations and porosity/permeability. So this chapter mainly investigates the effect of the pressure fluctuations, and the effect of cavitation erosion. Firstly, simulations were carried out to investigate the effect of an increased pore-pressure (back-pressure) during jetting. Secondly, experiments similar to the experiments conducted by Hahn et al. (2019) were carried out, however *inside* a cavity rather than on a flat surface. This was done in

order to see if cavitation occurs inside a cavity. Simulations were conducted to localise the occurrence of cavitation (using a multiphase solver). And finally, the jetted rock samples were analysed under a microscope with as aim to find a difference between cavitation erosion and destruction due to other mechanisms.

3.2.1 Back pressure Increase Simulations

In order to evaluate the pressure distribution in a rock sample, a pressure solver was developed using `Matlab`, with the Finite Difference Method (FDM) in 2D. The model uses Darcy-flow to solve the pressure and flow. This model can be used to evaluate the pore pressure distribution during jetting with an increasing back pressure. It can also provide the pore pressure differences which might be necessary to expulse the grains as described in in the theory of hydraulic fracturing. The model is written for both incompressible and slightly compressible flow. The slightly compressible pressure solver is potentially a better approximation because the process of hydraulic fracturing as layer of grains is a transient process: it requires pressure differences on very small time scale which is not captured in the steady state (incompressible) case. The model is eventually combined with the results of the *Ansys* simulations to implement the jet pressure. This section presents the methodology and parameters of the two models (incompressible and slightly compressible).

Governing Equations

The general Mass conservation equation is given by equation 3.2 below:

$$\frac{\partial}{\partial t}\left(\phi \rho_\alpha S_\alpha\right) - \nabla \cdot \left(\rho_\alpha \lambda_\alpha \cdot \nabla p\right) = \rho_\alpha q_\alpha \tag{3.2}$$

Because we only deal with water in this study, only single-phase flow is considered, hence $\alpha = 1$ and $S = 1$. Furthermore, density and porosity are constant for incompressible flow. But density is however a function of pressure and thus non-linear in (slightly) compressible flow. For slightly compressible flow, the change of pressure over time is multiplied by a compressibility term (C_{eff}). The equations for incompressible and slightly compressible flow respectively are listed below (equation 3.3 and 3.4).

$$-\nabla \cdot \left(\lambda \cdot \nabla p\right) = q \tag{3.3}$$

$$\phi C_{eff} \frac{\partial p}{\partial t} - \nabla \cdot \left(\lambda \cdot \nabla p\right) = q \tag{3.4}$$

Incompressible flow is time-independent. Slightly-compressible flow is however time-dependent since it takes time for the pressure to reach the steady-state solution and must therefore be solved in time.

Mesh

The rock sample is modelled numerically in 2D using a rectangular geometry having the sample's dimensions (50mm x 50mm) and using rectangular mesh elements. There are 40

000 mesh elements used with dimensions 0.25 x 0.25mm.. The mesh is shown in figure 3.11 below. The location where the jet acts is depicted as red. The back pressure is applied to all the other boundaries. The pressure which is applied to the red elements is taken from the *Ansys* simulations, which varies every time-step.

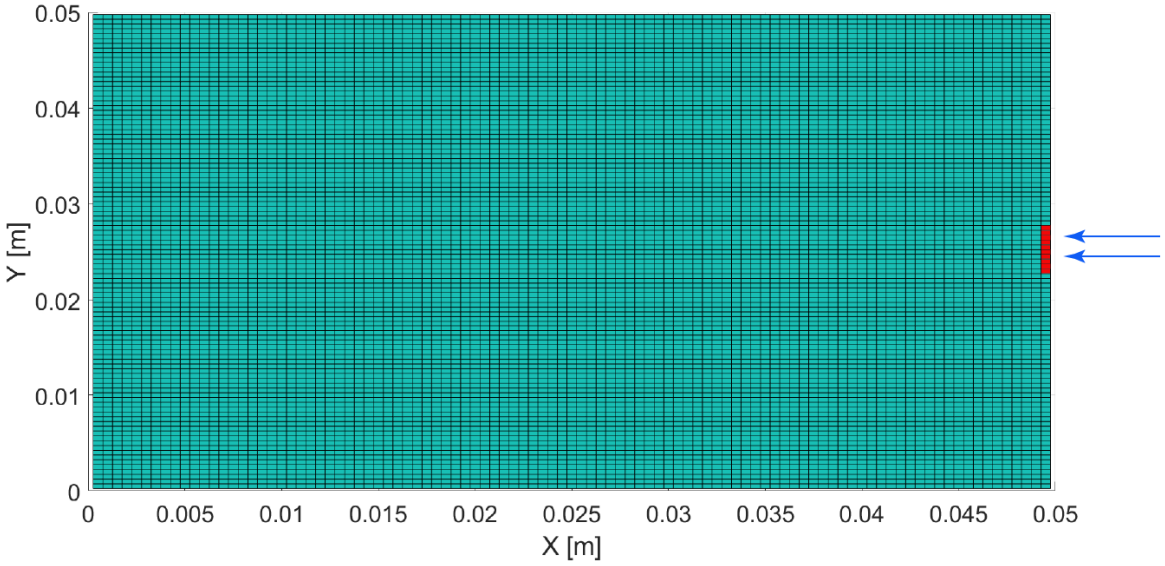

Figure 3.11: Grid of the FDM-solver. The location where the water jet acts is depicted in red.

Discretization

Discretization of $\frac{\partial}{\partial x}\left(\lambda\frac{\partial p}{\partial x}\right) = q$ for cell i gives the following equation:

$$\frac{(-\lambda\frac{dp}{dx})^{i+1/2} - (-\lambda\frac{dp}{dx})^{i-1/2}}{\Delta x} = q_i$$

In 2D, the above equation changes; the x is replaced for y and i for j.

Which is approximately (FD approach):

$$\underbrace{\frac{\lambda^{i-1/2}}{\Delta x^2}}_{T_{i-1/2}}(p_i - p_{i-1}) + \underbrace{\frac{\lambda^{i+1/2}}{\Delta x^2}}_{T_{i+1/2}}(p_i - p_{i+1}) = q_i \tag{3.5}$$

If one uses the finite volume approach, which is more convenient, then $A\Delta x$ (=Volume) is multiplied with equation 3.5 above to give the following equation:

$$\underbrace{\frac{A\lambda^{i-1/2}}{\Delta x}}_{T_{i-1/2}}(p_i - p_{i-1}) + \underbrace{\frac{A\lambda^{i+1/2}}{\Delta x}}_{T_{i+1/2}}(p_i - p_{i+1}) = A\Delta x q_i \tag{3.6}$$

At the boundary of the mesh the distance is only half the distance of a normal cell. The equations for the first and last cell are shown respectively below:

$$\frac{A\lambda^{1}}{\Delta x/2}(p_1 - p_{left}) + \frac{A\lambda^{1+1/2}}{\Delta x/2}(p_1 - p_2) = A\Delta x q_1 \tag{3.7}$$

$$\frac{A\lambda^{N_x-1/2}}{\Delta x/2}(p_{Nx} - p_{N_x-1}) + \frac{A\lambda^{N_x}}{\Delta x/2}(p_{N_x} - p_{right}) = A\Delta x q_{Nx} \tag{3.8}$$

Since the mobility λ is only known at every cell centre, while the equations above use the mobility at the interface, the harmonic average is taken to obtain the mobilities at the interface (i.e $\lambda^{i+1/2}$):

$$\lambda^{i+1/2} = 2\frac{\lambda^i \lambda^{i+1}}{\lambda^i + \lambda^{i+1/2}} \tag{3.9}$$

Rearranging equation 3.5 gives the following relation, where T is the transmissibility:

$$-T_{i-1/2}p_{i-1} + (T_{i+1/2} + T_{i-1/2})p_i + (-T_{i+1/2})p_{i+1} = q_i \tag{3.10}$$

This results in a set of linear equations ($A + p = q$) which can be solved for the pressure. Where A is the transmissibility matrix, p the pressure and q the source term. The problem is solved implicitly using the Backward Euler approximation in time. This approximation is unconditionally stable, hence stable for all delta t. The implicit scheme is shown below in equation 3.11.

$$\phi C_{eff}\frac{p^{n+1} - p^n}{\Delta t} = \frac{\partial}{\partial x}\left(\lambda\frac{\partial p^{n+1}}{\partial x}\right) + q^{n+1} \tag{3.11}$$

This can be written in terms of C and A as follows:

$$(C + A)p^{n+1} = q + Cp^n$$

Which is a linear set of equations which can be solved in `Matlab` as follows:

$$p^{n+1} = (C + A)\backslash(q + Cp^n)$$

If the pressure is solved, the transport can be solved as well in order to calculate the flow behaviour in the rock sample which was not the goal of the simulation, but it can be interesting if the solver is combine with the pressure data from the *Ansys* simulations, because it can potentially show where the destructed "particles" move (as the flow is a result of pressure differences).

3.2.2 Cavitation Erosion Inside a Cavity

As described in section 2.6.2, experiments (Hahn et al., 2019) and simulations (Kumagai et al., 2011) were carried out to investigate the location where cavitation erosion occurs during jetting on a flat aluminium surface. However, the location of cavitation *inside* a cavity is not yet known. As part of this research on the governing destruction mechanism, the cavitation inside a cavity is investigated both in a experimentally and with simulations in *Ansys Fluent*, the methodology is discussed further in this section.

Experiments

As a cavity is created by the jet, the fluid flow inside that cavity will become highly turbulent because of the high velocities and back-flow. This turbulence might create local pressure changes high enough to create cavitation bubbles. The location and intensity of this cavitation is however unknown. The experiments are similar to the ones conducted by Hahn et al. (2019). That is, a polished aluminium plate was used, however an aluminium adapter with a drilled hole is introduced (similar to the ones used in experiment (C) and (D), described in section 3.1.2) which was put on top of the aluminium plate. The thickness of the adapters (i.e., depth of the cavity) varies from 5mm to 30mm. There has been chosen for this thickness because in the experiments where a rock was jetted with an aluminium adapter of 25mm, the jet was not able to penetrate the rock anymore. So if cavitation occurs at these depths, it is at least not creating (enough) damage to the rock. The 30mm adapter was chosen to secure the findings, and have a larger range. The aluminium plates were analysed under a microscope to qualitatively assess the location and intensity of cavitation erosion on the plates.

Simulations

Cavitation is simulated using a multi-phase fluid solver. There is single-phase flow at the inlet (liquid). When the pressure in the fluid drops below the vapour pressure (3540 Pa in these simulations), the liquid will change to vapour. The model is only capable of showing the location where cavitation happens, which is not necessarily the location where cavitation *erosion* occurs. The simulations were setup similarly to the models discussed in section 3.1.3. Simulations for solving the location of potential cavitation erosion were carried out on a flat surface, to compare them with the findings of Hahn et al. (2019) and Kumagai et al. (2011) discussed in section 2.6.2, and in a cavity of 10 millimetres deep to compare with the experiments described above.

3.2.3 Analysis of the Jetted Rocks

Bakker and Barnhoorn (2019) showed that the grains and other rock properties were still unchanged moving towards the proximity of the jetted hole. This was observed in a CT-scan image. Hahn et al. (2019) measured the diameter of impact diameter of cavitation erosion on an aluminium plate and found that the diameter of erosion (25-30 micrometers on average) is significantly smaller than one grain (200 micrometers, for BD sandstone). So the damage on grain scale by cavitation erosion should also be visible on the grains itself, which was not the case in the study of Bakker and Barnhoorn (2019). Rocks that have a cavity due to jetting and rocks with cavitation damage (see figure 2.7b in section 2.6.2) were analysed using a CT-scanner to image the rock at grain scale. The hypothesis is that one can differentiate between cavitation erosion and other destruction mechanisms that do not cause damage the grains themselves by looking at individual grains on the CT-scans. That might prove that cavitation is not the destruction mechanism during jetting.

3.3 Jetting Correlation

As mentioned earlier, the jetting correlation proposed in this section should combine the pressure-depth relationship with the hydraulic fracturing destruction mechanism. If the hypothesis of hydraulic fracturing as the governing erosion mechanism is correct,the destruction of the rock could then be estimated by a correlation consisting of the hydraulic and the material properties. The aim of such a correlation is to estimate the cavity depth a jet can create in a given time with a static nozzle. The advantage of such a correlation is that it can provide a forecast of whether a rock is jettable or not. For this correlation, the model of the rock is highly simplified. The assumptions made for the correlation are shown below.

- Mono-disperse hexagonal packing
- Grains are assumed to be perfect spheres with an average diameter r_{mean}
- Grains stay intact, matrix breaks
- Homogeneous matrix properties
- Matrix material has a zero thickness
- Hydraulic force only acts on grains
- Homogeneous hydraulic properties
- Exponential increase in pore pressure in first layer of grains
- Bonds break in one direction, so a layer of grains is eroded instead of individual grains

Figure 3.12 below shows the simple 1D model which shows the pore pressure build-up due to the applied stagnation pressure by the jet, as well as the grain packing with their pores and matrix material (bonds). Where the graph shows the increasing tensile stress on these bonds.

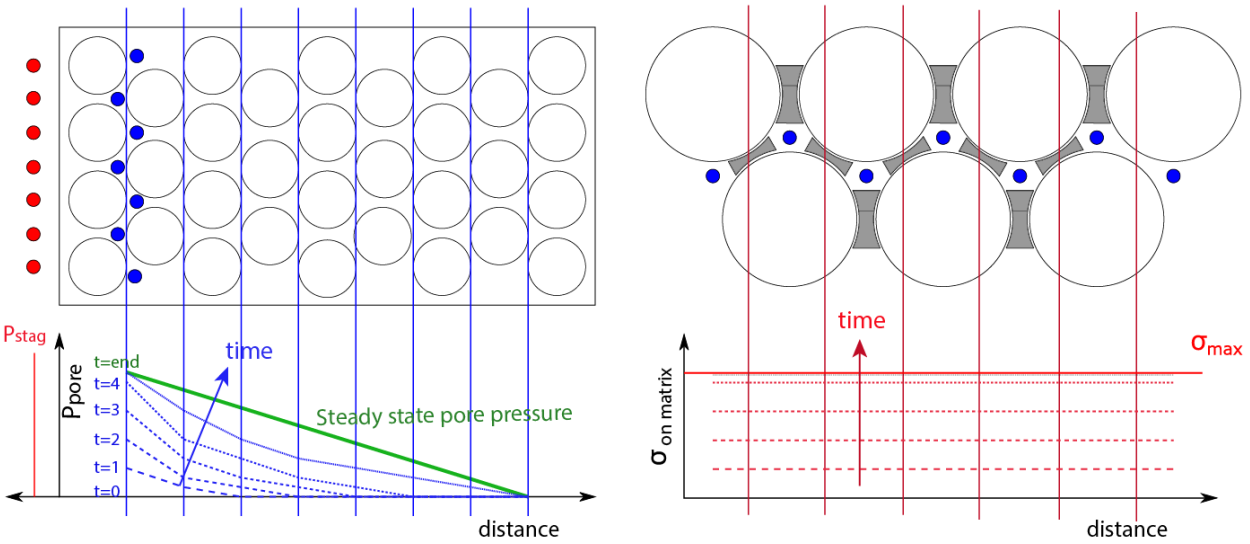

Figure 3.12: Pore Pressure build up from stagnation pressure over time (left) and packing scheme of the rock with their corresponding bonds with a graph of the increasing tensile stress on the grains over time due to pore pressure increase (right).

The left diagram in figure 3.12 shows the pore pressure (blue dots) increase due to the stagnation pressure (red dots). The graph below the schematic representation of the rock shows that the pore pressure increase is a time-dependent process (milliseconds), so the pore pressure is increasing over time and distance (to the right) until the steady state is reached (green line). The right side of figure 3.12 shows the first two layers of grains and the first layer of pores. As time passes, the pore pressure increases which results in a force acting on the grains. When the stagnation pressure is suddenly dropped (due to fluctuations caused by turbulence and pump frequency), the pore pressure in the first layer is still present which results in a tensile stress within the first layers of pores. When the magnitude of this tensile stress goes beyond the ultimate tensile strength (UTS) of the bonds(red line), the grains will be expulsed, according to the theory of hydraulic fracturing.

In this model, the pore has a maximum volume capacity that it can reach. When this volume reaches the maximum value, too much stress is exerted on the adjacent grains which in turn leads to rupture of the inter-granular bonds. This pore is filled trough its associated pore-throat and described by Darcy-Weisbach equation (equation 3.14), where the area of one third of a grain is used. The filling of the pore towards its maximum capacity has a logarithmic behaviour (see graph on the left in figure 3.12), where the analogy of a capacitor in an electric circuit can be made. Equation 3.12 shows the relation for the loading of a capacitor in a circuit following Kirchhoff's voltage law, that calculates the potential (U) after a certain amount of loading time.

$$U(t) = U(0)(1 - e^{-t/\tau}) \tag{3.12}$$

Where τ is a time constant defined by $\tau = R * C$. R is the resistance and C is the specific capacity, a property of the capacitor. Furthermore, $U(t)$ is the potential of the capacitor after a certain loading time (t), $U(0)$ is the applied voltage during loading. The analogies to

the hydraulic loading of pores is as follows:

- $U(t)$ = Pore pressure $P_p(t)$ in the first layer of pores (blue dots in figure 3.12) after a certain time of jetting.
- $U(o)$ = Stagnation pressure P_s exerted on the first layer by the jet.
- R = Resistance to flow, which is the inverse of the flowrate ($1/Q$, where Q is the volume flowrate (equation 3.14) through the adjacent pore-throat.
- C = Maximum virtual expansion of one pore ΔV until the pore pressure passes the maximum differential pressure, such that the bond breaks.

The above described analogies lead to the following equation for the pore pressure over time:

$$P_p(t) = P_s(1 - e^{-\frac{t}{1/Q*\Delta V}}) \tag{3.13}$$

Where Q is described by the Darcy-Weisbach equation as shown below in equation 3.14.

$$Q = \frac{\pi * D^4}{128\mu}\frac{\Delta P}{\Delta L} \tag{3.14}$$

These equations cover the hydraulic part of the correlation, which gives the pore pressure as a function of time. The material model must now be formulated. As discussed earlier, a hexagonal packing scheme is assumed for the material model as shown in figure 3.12. The aim of the material term in the equation is to identify a pore pressure threshold at which the force on a grain becomes larger than the tensile strength of the matrix of the rock (bonds). Therefore, the pore geometry is examined as well as the area of the grain where the pore pressure is acting on (to calculate the force). Furthermore, the area of 1 bond is needed for the material model. These parameters are calculated with the use of examining one unit cell of a hexagonal closed packing (HCP) as shown in figure 3.13. There are 6 complete grains in one unit cell, 18 pores, and every grain has 12 bonds (contact with other grains). The void geometry of a HCP is tetrahedron and octahedron with a ratio of 2:1 respectively.

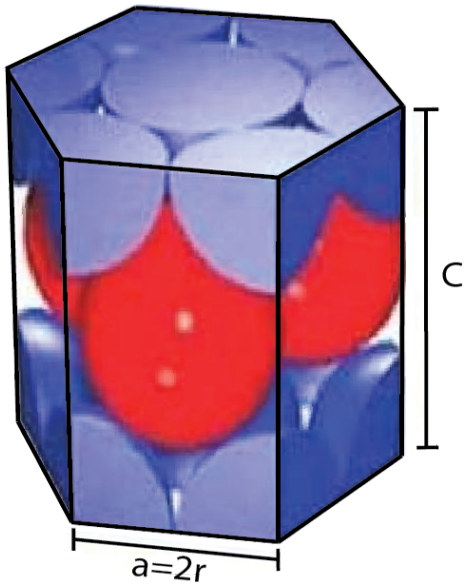

Figure 3.13: Unit cell with hexagonal closed packed grains inside.

The volume of the unit cell is defined as the area of a hexagon with side length (a) times the height (c) of the unit cell:

$$V_{unit\ cell} = \frac{3\sqrt{3}}{2} a^2 * c \tag{3.15}$$

Where a is two times the grain radius r_g (see figure 3.13). The relation between c and a is always the same for a HCP and is defined as $c/a = \sqrt{8/3}$, which means that $c = \sqrt{8/3} * 2 * r_{grain}$
The volume of 6 spherical grains inside the unit cell is equal to:

$$V_{grains} = 6 * (\frac{4}{3}\pi * r^3) \tag{3.16}$$

The volume of the voids is calculated as follows:

$$V_{voids} = V_{unit/cell} - V_{grains} \tag{3.17}$$

So the (theoretical) porosity of HCP unit cell is:

$$\phi_{theoretical} = \frac{V_{voids}}{V_{uni\ cell}} \tag{3.18}$$

The theoretical porosity of a HCP is independent of the grain diameter and hence always the same: 25.95%. Rocks usually have cement or other matrix materials that form the bonds between the grains, occupying part of the void space. Assuming an HCP and perfect spherical grains, the matrix material ($M_{fraction}$ should be equal to:

$$M_{fraction} = \phi_{theoretical} - \phi_{measured} = 0.2595 - \phi_{measured} \tag{3.19}$$

As mentioned before, the voids in a HCP are either tetrahedral or octahedron in a 2:1 ratio. For the jetting correlation, an average pore volume is needed, which is calculated as follow:

$$\overline{V}_{pore} = V_{voids}/18 \tag{3.20}$$

It is assumed in the model that the matrix material is located in the corners of the voids. A tetrahedron has 4 corners while a octahedron has 6 corners. So the average number of corners is (2*4+1*6)/3=4.67 (2:1 ratio). The volume of 1 corner is defined as follows:

$$V_{corner} = \frac{V_{pore} * M_{fraction}}{4.67} \tag{3.21}$$

The height of the tetrahedron filled with cement is half the length of 1 bond, which is the radius of the bond material (r_{bond} which is needed to calculate the area of bond material. The height of this small corner can be calculated with the volume of one corner:

$$r_{bond} = \sqrt[3]{\frac{V_{corner}}{0.2165}} \tag{3.22}$$

The Force needed to overcome the tensile strength of the bond between two layers is defined as the the ultimate tensile strength times the area of one bond:

$$F_{max} = UTS * (pi * r_{bond}^2) \tag{3.23}$$

The last parameter which is needed is the area of the pore on one grain (one face of the pore geometry). Every pore has 4.67 corners (bonds). And every bond is shared with 4 other pores. Every pore has on average (2*4+1:8)/3 = 5.33 grain faces where it is acting on. So the area where the pore pressure acts on one grain is described as follows:

$$A_{act} = \frac{A_{grains} - (18\ [pores]) * (4.67\ [corners/void]) * (1/4) * (\pi * r_{bond}^2)}{18} \tag{3.24}$$

The pore pressure is acting on an angle of 60 °. So the Force from the pore needed to overcome the ultimate tensile force is defined as:

$$F_{act} = \frac{F_{max}}{sin(60)} \tag{3.25}$$

So the pore pressure threshold to expel one grain is the needed force (F_{act}) divided by the area of the grain in contact with the pore which was A_{act} from equation 3.24. So the material part of the jetting correlation becomes:

$$P_p = \frac{F_{act}}{A_{act}} \tag{3.26}$$

Summarising equation 3.15 untill 3.26 gives the following formulation for the pore pressure threshold:

$$P_p = \frac{UTS * \left[\pi * \left(\frac{V_{unit\ cell} - V_g rains) * (M_{fraction})}{18}\right)^{2/3}\right]}{\left(6 * A_{grain} - 1.1675 * \left[\pi * \left(\frac{V_{unit\ cell} - V_g rains) * (M_{fraction})}{18}\right)\right]^{2/3}\right) * \sin(60)} \tag{3.27}$$

The above equation can be written in terms of grain radius UTS, grain radius r_g and porosity ϕ:

$$P_p = \frac{UTS\left[\pi\left(\frac{r_g^2(\frac{4}{\sqrt{3}}r_g - 6\pi)(0.2595-\phi)}{18}\right)\right]^{2/3}}{\left(24\pi r_g^2 - 1.1675\left[\pi\left(\frac{r_g^2(\frac{4}{\sqrt{3}}r_g - 6\pi)(0.2595-\phi)}{18}\right)\right]^{2/3}\right)\sin(60)} \tag{3.28}$$

Equating the material formulation above with the hydraulic formulation (equation 3.13) gives the jetting correlation:

$$P_s(1 - e^{-\frac{t}{1/Q*\Delta V}}) = \frac{UTS\left[\pi\left(\frac{r_g^2(\frac{4}{\sqrt{3}}r_g - 6\pi)(0.2595-\phi)}{18}\right)\right]^{2/3}}{\left(24\pi r_g^2 - 1.1675\left[\pi\left(\frac{r_g^2(\frac{4}{\sqrt{3}}r_g - 6\pi)(0.2595-\phi)}{18}\right)\right]^{2/3}\right)\sin 60} \tag{3.29}$$

If the hydraulic and material properties are known, one can estimate the time which is needed to erode 1 layer of grains. Due to the closed packing, the depth of the created cavity in this time doe not equal the radius of a grain. There are effectively 2 grains stacked in the hexagonal unit cell, which means that the depth of the cavity, after erosion of one grain layer is the unit cell height c divided by 2 grains:

$$depth(t) = \frac{c}{2} = \frac{\sqrt{\frac{8}{3}} * 2r_g}{2} = \sqrt{\frac{8}{3}} * r_g \tag{3.30}$$

The jetting correlation is dependent on the stagnation pressure (P_s), which changes when material is eroded. The jetting correlation in combination with the *Ansys* simulations (for the pressure-depth relationship) will provide the theoretical maximum jetting depth. The jetting correlation will be validated by using the results of the experiments (A), where the maximum jetting depth was measured.

4. Results & Discussion

This chapter describes the results of the experiments and simulations explained in chapter 3. The experiments and simulations had the aim to provide a relation between pressure and cavity depth, and to prove/disprove the governing destruction mechanism during jetting. The last section of this chapter combines the results into a 'jetting correlation' which is tested with experiments.

4.1 Pressure-Depth Relation

Experiments were performed to investigate the depth at which the jetting stops with a static nozzle. The pressure at these depths is analysed with numerical simulations, which give the full pressure versus depth profile. The results give an insight into the optimum nozzle-rock distance. Furthermore, experiments and simulations were performed which show the effect of a fracture across the jetted cavity.

4.1.1 Experimental results

This section presents the results of the jetting experiments at atmospheric conditions. Jetting experiments were carried out on: (A) a blank rock surface, (B) rocks with a pre-drilled cavity, (C) rocks with a sealed aluminium adapter and (D) on a rock with a non-sealed aluminium adapter (artificial fracture). The Bad Durkheim is used for all the experiments whereas the other two sandstones are only used for experiments (A) and (B). The results of each experiment are presented below.

Blank Rock Surface (A)

The jetting experiments on a blank surface were performed in order to investigate the maximum cavity depth a jet could drill with a static nozzle (not moving into the borehole). The depth was measured after jetting for 10, 30 and 300 seconds (for the BD sandstone). Where the depth after 300 seconds was assumed to be the maximum possible depth with the used flowrate of 28L/min. Figure 4.1 below shows the results for the Bad Durkheim Sandstone. The rock was jetted for 10 seconds in experiment 1-4, 30 seconds in experiment 5-8 and for 300 seconds in experiment 9 and 10. The maximum jetting depth is approximately 25mm, which is already reached in 10 seconds in one of the conducted experiments. The depth did not increase drastically after 30 seconds of jetting. The red line in figure 4.1 represents the maximum jetting depth (average depth after 300 seconds of jetting).

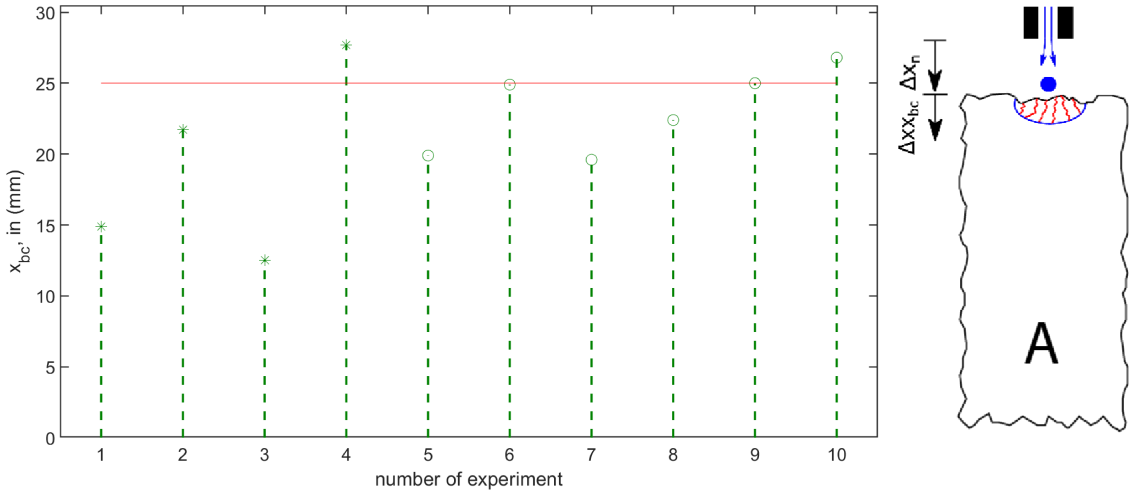

Figure 4.1: Maximum jetting depth into the BD sandstone. The height of the green dashed lines show the jetted depth (Δx_{bc}. The horizontal red line indicates the maximum jetting depth (25mm).

For the Dortmund and Gildehaus sandstone, experiment (A) was conducted less times. The jetting depth of the Dortmund and Gildehaus sandstones after different jetting times are presented in table 4.1 below. Every experiment was repeated twice (the two rows for every sandstone in table 4.1). The maximum jetting depths of the Dortmund and Gildehaus sandstones are 13 and 50mm respectively.

Table 4.1: Jetting depth after 10, 30 and 300 seconds into the Dortmund and Gildehaus sandstones. Maximum jetting depth is 15 and 50mm respectively.

	experiment #	**depth [mm] 10s**	**depth [mm] 30s**	**depth [mm] 300s**
Dortmund	1	1	2	13
	2	0	4	10
Gildehaus	1	-	38	50
	2	-	34	47

When jetting was continued, after the maximum depth was reached, the created cavity was washed out (widening of the hole). Cavity widths increasing from 5 to 8 millimetres were observed in the Bad Durkheim and Gildehaus sandstones. The widening of the borehole results in easier backflow (discharge of the water out of the cavity), which results in a higher pressure on the cavity bottom. This higher pressure is due to the fact that the jet can focus better if the water, which is standing in the borehole, can be discharged more efficiently. So even after the maximum depth is reached, it can slowly drill slightly further, due to this widening of the hole. To overcome this effect, experiments were performed where a pre-drilled hole was already drilled into the sample, with the exact same diameter (8mm) and different depths (experiment (B)). The results of these experiments are discussed in the next section below.

Rock with Pre-Drilled Hole (B)

The samples that were used in this experiment had pre-drilled hole, ranging from 5 to 25 millimetres depth. The experiments were performed on the Bad Durkheim, Dortmund and Gildehaus sandstones. The goal of these experiments was to investigate the maximum jetting depth when the pre-drilled cavity is the same for every experiment in terms of wall friction factor and cavity diameter. The different depths of the pre-drilled cavity show the effect of friction factor and cavity diameter. The results of the experiments are shown in figure 4.2, 4.3 and 4.4 for the Bad Durkheim, Dortmund and Gildehaus sandstones respectively. The red lines represent the depth of the pre-drilled cavity, the blue line shows the jetted depth (Δxx_{bc}) and the dashed green line shows the total depth, which is the pre-drilled depth added to the depth created by the jet ($\Delta xx_c + \Delta xx_{bc}$). The jetting exposure time was 30 seconds in every experiment presented in this section.

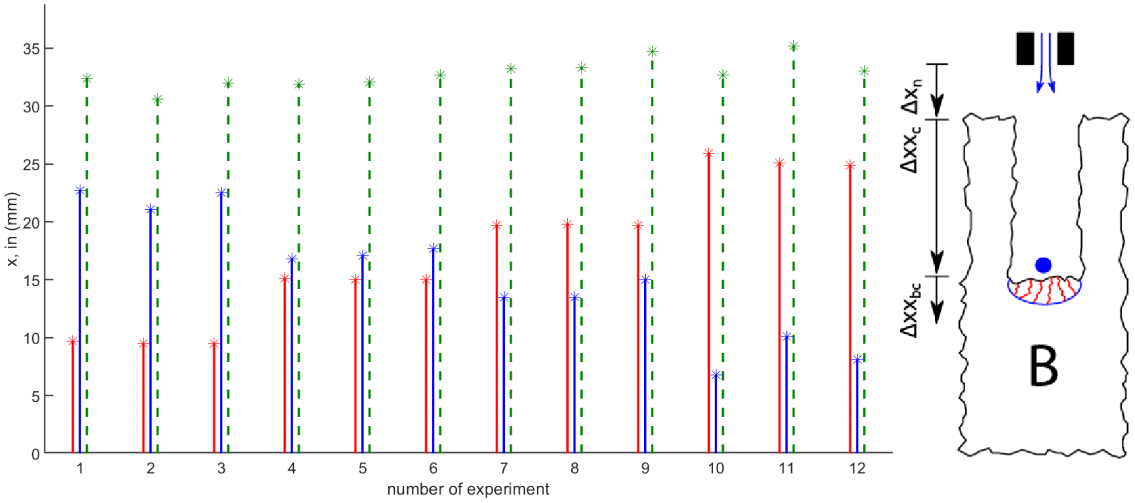

Figure 4.2: Results of jetting into the Bad Durkheim sandstone with a pre-drilled cavity with and increasing depth. The pre-drilled cavity depth is depicted in red, the blue line represents the jetted depth (xx_{bc}) and the green dashed line is the total depth ($\Delta xx_c + \Delta xx_{bc}$).

It can be observed from figure 4.2 above that the maximum jetting depth of the BD sandstone is now 32mm. The jet was able to drill further because the backflow out of the cavity was more efficient compared to experiments (A). However, the differences are subtle, resulting in an almost similar final depth in all experiments.
Figure 4.3 shows the results of jetting into the Dortmund sandstone with pre-drilled holes.

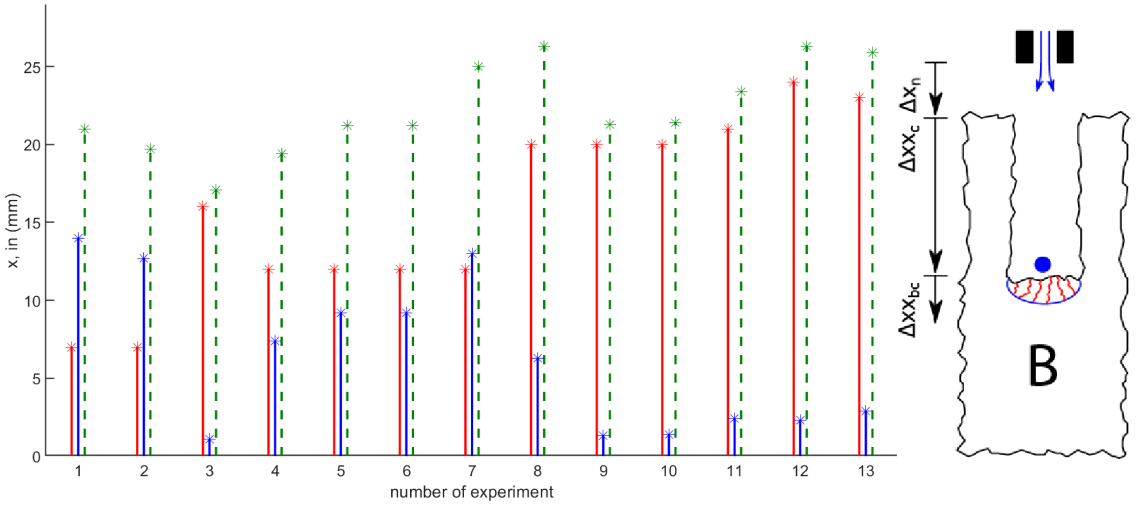

Figure 4.3: Results of jetting into the Dortmund sandstone with a pre-drilled cavity with an increasing depth. The pre-drilled cavity depth is depicted in red,the blue line represents the jetted depth (xx_{bc} and the green dashed line is the total depth (adapter depth + jetted depth).

The final jettable depth varies more with the Dortmund sandstone compared to the previously shown BD sandstone. With a shallow pre-drilled cavity, the total depth was around 19mm whereas the total depth with a pre-drilled cavity of 20mm showed a total depth of up to 25mm (see figure 4.3). The reason for these differences is that the Dortmund sandstone is very hard (in terms of UCS and UTS) and has a low porosity and permeability (see table 3.1). Moreover, the jetting exposure time was probably not long enough to reach maximum depth in the experiments with a shallow pre-drilled cavity, which explains the difference in jetting depth, apart from the easier backflow (deeper pre-drilled hole means less friction). However, results between similar pre-drilled depths varied more than the BD sandstone. The variation is probably due to the heterogeneity of the Dortmund sandstone. The experiments above were drilled with a high pressure on the nozzle (240 bar instead of the 160 bar, used in all the other experiments). That explains the discrepancy between the maximum jetting depth of the Dortmund sandstone presented in table 4.1 of experiment (A) and the graph shown in figure 4.3.

The results of jetting into the Gildehaus sandstone is shown in figure 4.4 below.

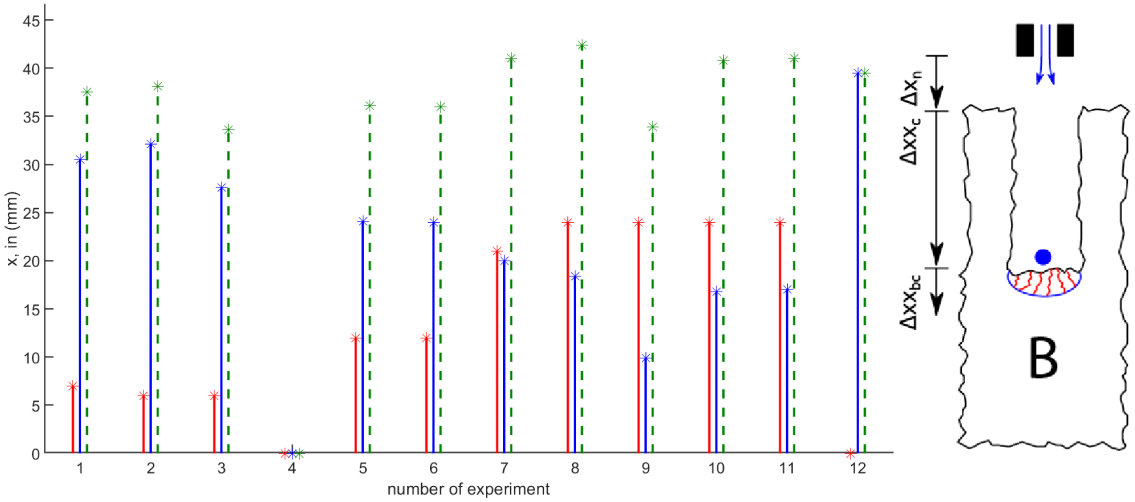

Figure 4.4: Results of jetting into the Gildehaus sandstone with a pre-drilled cavity with an increasing depth. The pre-drilled cavity depth is depicted in red,the blue line represents the jetted depth (xx_{bc} and the green dashed line is the total depth (adapter depth + jetted depth).

The Gildehaus sandstone is a rock with a high porosity and a very high permeability (6300 mD). This resulted in a very deep cavity compared to the two sandstones discussed above. Jetting depths of over 40mm were observed. A difference in total depth with varying pre-drilled depth is not visible. It was observed that the wash-out was much more severe with this sandstone compared to the other two sandstones.

To conclude, the depth of the pre-drilled cavity did not change much to the maximum total jettable depth. But the smoother and wider the hole, the more efficient the backflow out of the hole, resulting in better focusing of the jet and a higher maximum jettable depth.

Sealed Aluminium Adapter (C)

The experiments with an aluminium adapter on top of the rock sample don't differ much from experiment (B). As the experiments with a pre-drilled cavity (experiments (B)) had the limitation that the wall was permeable, fluid could dissipate through the wall, making the experiments less consistent (due to heterogeneity of the rocks). Replacing the pre-drilled hole with an aluminium adapter eliminates this effect; the hole is not permeable and the wall fiction is the same in every experiment.

The aluminium adapter was sealed with a rubber between the adapter and the rock (see section 3.1.2 for the scheme of the setup). The experiments with a sealed aluminium adapter were only performed on the Bad Durkheim sandstone. The results are shown in figure 4.5 below. The red horizontal line represents the depth of the aluminium adapter (25mm). The diameter of the drilled hole in the adapter was 6 mm, except for experiment 8, 9 and 10, which had a hole diameter of 8 mm.

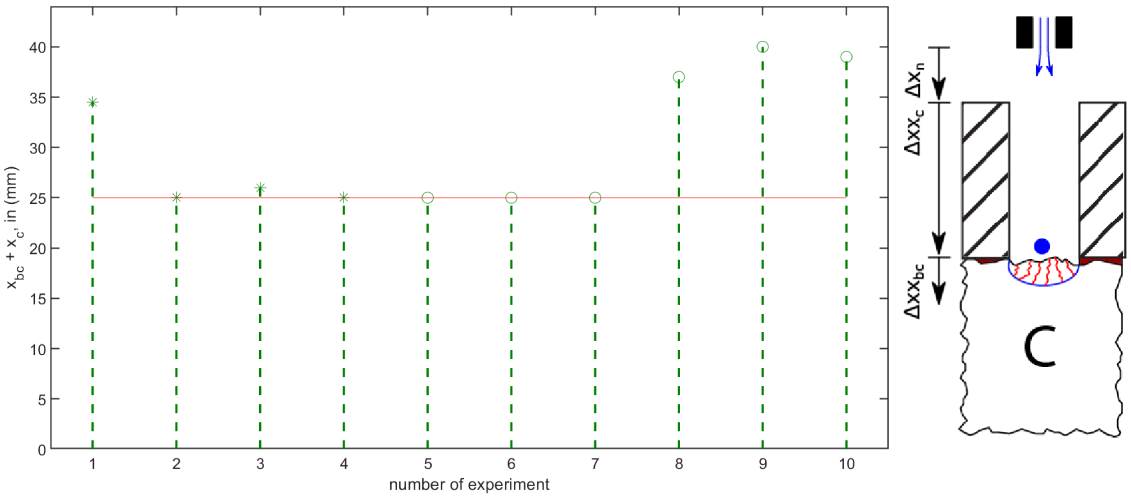

Figure 4.5: Results of jetting the Bad Durkheim sandstone through an aluminium adapter as shown in the diagram at the right of the graph. The used adapter had a thickness (i.e, depth) of 25mm (depicted by the horizontal red line). Experiments 8, 9 and 10 were performed with an 8mm diameter adapter (instead of 6mm), creating a more efficient backflow resulting in a more focused jet on the cavity bottom.

From the graph shown above in figure 4.5, it can be seen that the jet was not able to drill further than the depth of the aluminium adapter when using a 6mm diameter aluminium adapter (except for experiment 1). When the inner diameter of the adapter was increased to 8mm, the jet was able to drill 15mm beyond the adapter, reaching a final depth of 40mm. From this result, it can be concluded that increasing the adapter's inner diameter (i.e more efficient back flow) makes a significant difference. With a 8mm diameter aluminium adapter, the jet was able to drill further than the 8mm diameter pre-drilled cavity from experiment (B). This difference is probably due to the higher friction factor of the rock compared to the aluminium hole. As discussed in section 3.1.2, sometimes the rubber between the adapter and the rock was not sealing properly. This was then leading to a pathway for the fluid to escape (more efficient backflow), resulting in a more focused jet on the cavity bottom. This scenario is analogous to a fracture in a rock. This led to the idea of intentionally creating a pathway between the adapter and the rock, which was done by cutting part of the rubber. The results of the non-sealing adapter experiment is presented in the next section.

Adapter with Artificial Fracture (D)

The experiments with an artificial fracture are similar to the experiments with an adapter as described above (experiment (C)). However, the rubber between the rock sample and the aluminium adapter is not sealed, creating a pathway for the fluid to escape. These experiments were only performed n the Bad Durkheim sandstone. Figure 4.6 shows the results of the experiments with a sealed adapter (on the left) and with a non-sealed adapter (artificial cavity) on the right. The red lines represent the depth of the aluminium adapter placed above the rock sample.

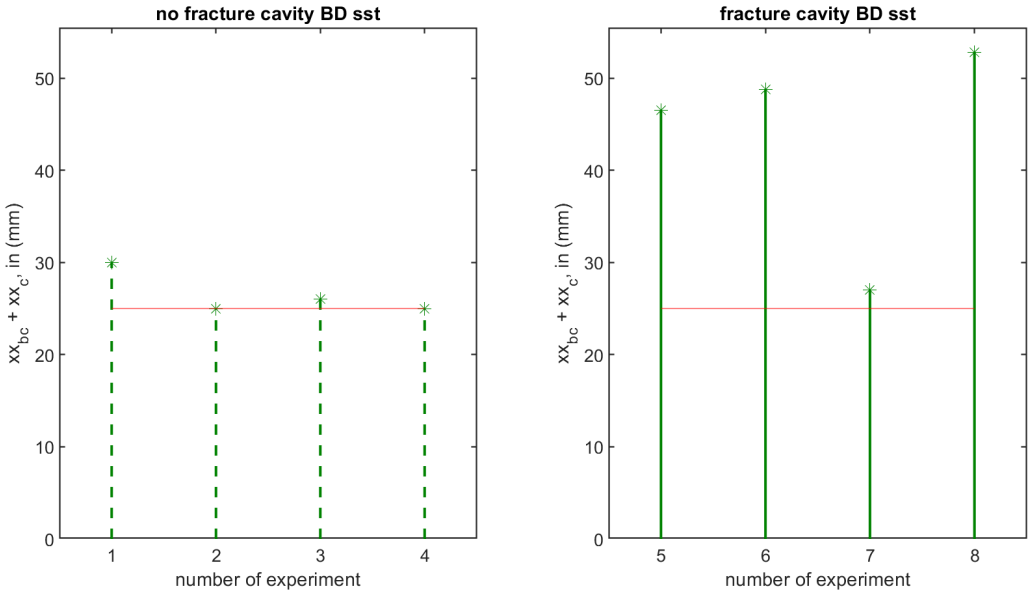

Figure 4.6: Comparison of jetting into the BD sandstone, with a sealed (left) and non-sealed (right) adapter. If the water is discharged efficiently, the jet can focus better on the cavity bottom, resulting in a larger total depth.

From figure 4.6 it can be seen that the creation of a fluid pathway results in a much deeper cavity. In experiment (A), the maximum jetting depth was determined to be 25 mm without an adapter. But the result with an artificial fracture shows that if the water can be discharged efficiently, the jet is able to drill as far as the maximum depth (see right graph of figure 4.6). This experiment is also numerically simulated in order to investigate the pressure differences at this depth with and without a fluid pathway. The simulation of this artificial fracture is presented in the following section.

4.1.2 Simulation Results

This section presents the results of numerical simulations carried out using the *Ansys Fluent* software. Firstly, a simulation of a water jet impinging a flat surface under pressurised conditions (95 bar) is presented. Secondly, the simulations of jetting into a cavity are discussed. The last section compares the simulation of an artificial fracture with the experiments and simulations without this artificial fracture.

Velocity Field comparison

In order to compare the simulations with the experimental data, the PIV measurements performed by Hahn et al. (2019) were simulated. Figure 4.7 shows the PIV measurements next to the simulated velocity field of a jet impinging an aluminium surface. It can be observed that the jet is more diverging in the PIV measurements than in the simulations. Furthermore, the jet in the PIV experiment is slightly deviated, resulting in a small difference between the measurements and the simulation. However, the velocity field of the simulation

is very similar to the measurements; all the characteristics such as stagnation point and (sideways) velocities are qualitatively accurate compared to the PIV measurements

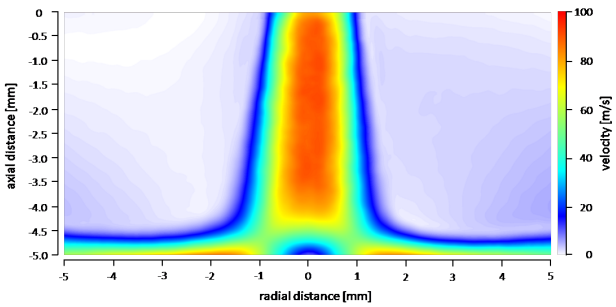

(a) PIV measurement of a water jet with 95 bar backpressure and a flowrate of 18 L/min (Hahn et al., 2019).

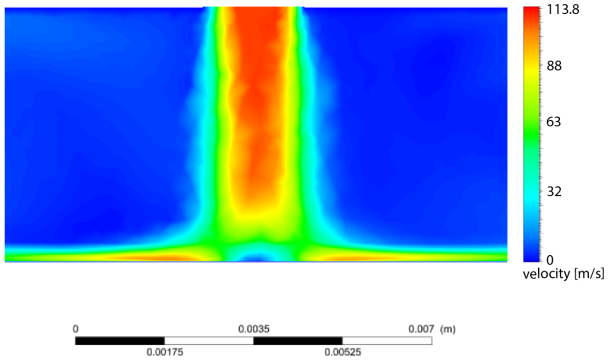

(b) Ansys simulation with 95 bar backpressure and a flowrate of 18L/min.

Figure 4.7: Comparison of the velocity field measured with PIV and the simulated velocity field with Ansys. The main difference is that the jet is more diverging in the PIV experiments. Note the colourbar, which is not exactly the same in both figures.

Pressure-Depth Relation

For the pressure-depth relationship, multiple water bodies with an increasing cylinder (cavity depth) were constructed (see figure 3.5 in chapter 3.1.3 for a schematic drawing of the water bodies). Simulations were performed at cavity depths ranging from 0-40mm. Figure 4.8 and 4.9 present the velocity and associated pressure profile of simulations at a cavity depth of 5 and 25 mm respectively. Simulation results at different cavity depths can be found in Appendix C on page 81.

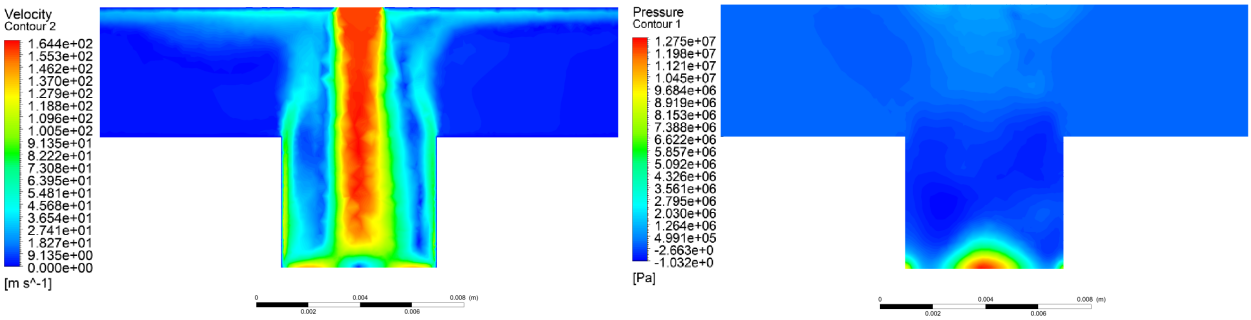

Figure 4.8: Velocity field (left) and pressure field (right) of the simulation of a jet in a cavity of 5mm depth at time step 11 (0.01s).

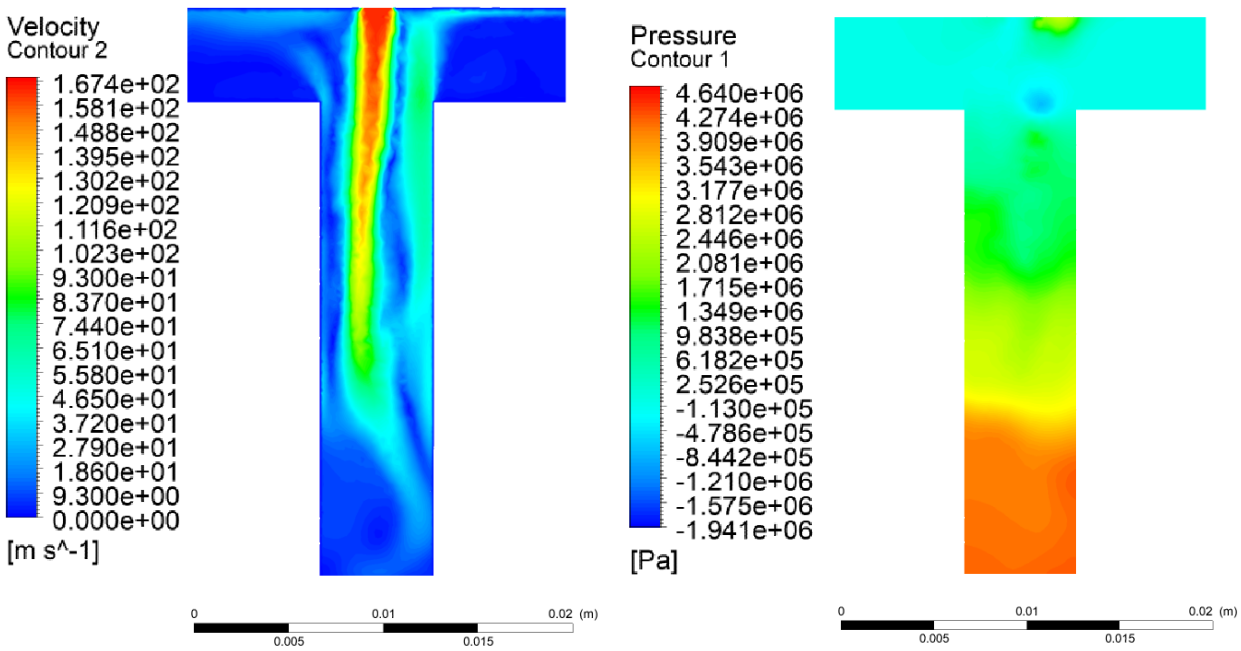

Figure 4.9: Velocity field (left) and pressure field (right) of the simulation of a jet in a cavity of 25mm depth at time step 21 (0.02s).

Considering figures 4.8 and 4.9, it can be seen that at a cavity depth of 5mm there is still a clear stagnation point. Whereas at a cavity depth of 25mm it becomes more of a pressure column, as the jet does not impinge directly on the cavity bottom. Moreover, the turbulence intensity becomes less after 5mm of cavity depth (with 160 bar nozzle pressure). This results in less pressure fluctuations at the cavity bottom.
Figures 4.8 and 4.9 are the results of a simulation at a time step of 0.001 seconds. In order to obtain a full pressure-depth relationship, the pressure at the cavity bottom is recorded in time for every simulated cavity depth. The results of these recordings is shown in figure 4.10. This is the actual pressure-depth relationship, but every depth is depicted by a colour. The x-axis represents time (as fluctuations are in time at one depth). Figure 4.11 shows the average pressure and the amplitude of the fluctuations versus depth.

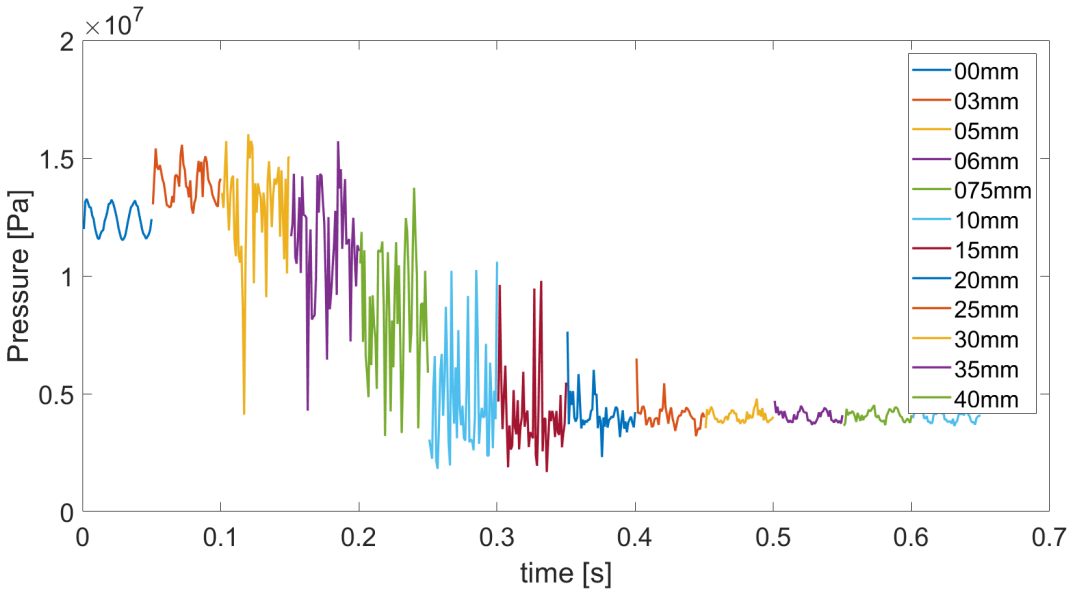

Figure 4.10: Pressure recorded in time for every simulated cavity depth. Every simulation had a time lapse of 0.05 seconds (as can be seen on the x-axis). However, increasing time on the x-axis also means an increase of cavity depth (figure not scaled as more simulations were run from 0-10mm)

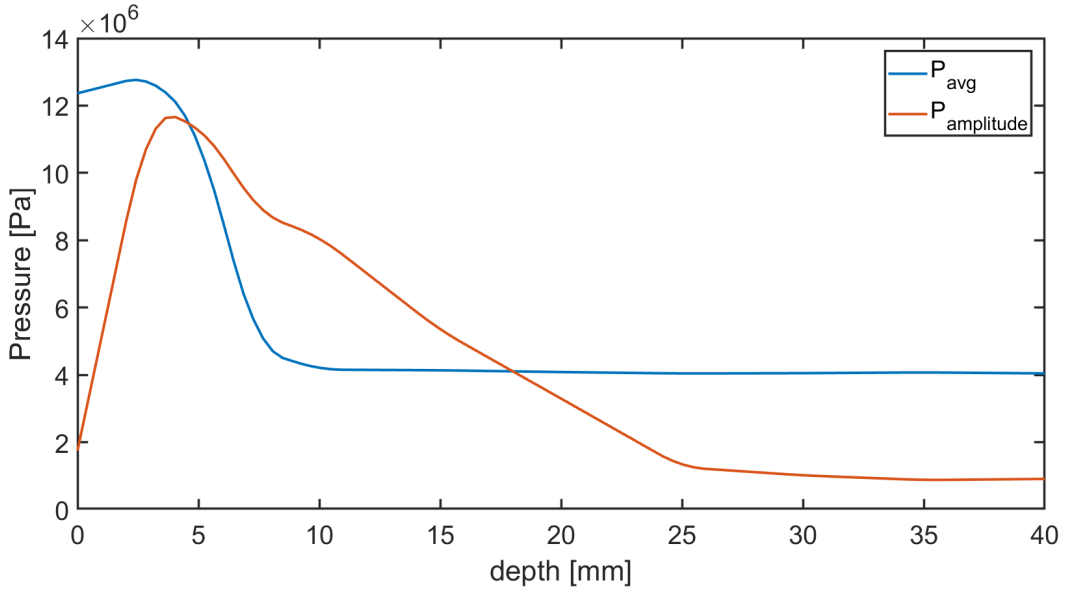

Figure 4.11: Average stagnation pressure on the cavity bottom and the amplitude of the fluctuations versus depth. Around 4mm, the pressure and the amplitude of fluctuations are the highest, which is potentially the depth where the jet has the highest ROP.

As can be seen in figure 4.10, if the cavity depth is 0mm, the pressure fluctuations follow the exact frequency of the velocity inlet of the jet. Once the jet has drilled a small hole (>0mm), the pressure fluctuations increase drastically, which also results in higher maximum stagnation pressures than obtained at 0mm depth (while the distance between nozzle and

rock increased, as cavity depth is increased). The increase in fluctuations is due to the increase of the turbulence intensity; when a small hole is created, water has to move out of the created cavity creating small eddies (i.e, turbulence). Figure 4.12 shows the pressure recordings at a depth of 3mm, plotted with the velocity of the nozzle outlet. It can be seen that the pressure fluctuations no longer follow the frequency of the velocity.

When the cavity depth is increased (more than 15mm depth), the turbulence intensity decreases again, resulting in less pressure fluctuations due to turbulence, which means the pressure fluctuations follow the velocity frequency of the nozzle again (see figure 4.10 and 4.11). The experiments with a jet showed a maximum depth of 25, 15 and 40mm for the Bad Durkheim, Dortmund and Gildehaus sandstones, respectively. That means that if the destruction process is dependent on pressure fluctuations, the minimum pressure fluctuations must have an amplitude of 15, 60 and 10 bar in order to effectively jet a hole (see figure 4.11.

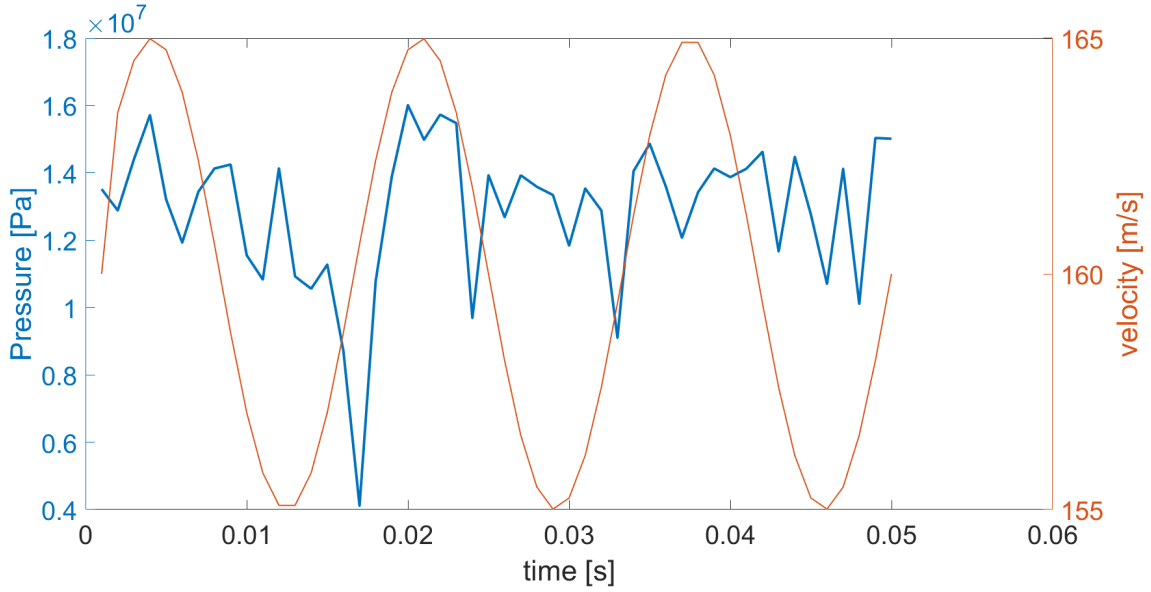

Figure 4.12: Pressure at a 3mm cavity bottom plotted with the velocity of the nozzle outlet. It can be observed that the pressure does not follow the frequency of the velocity anymore.

The pressure fluctuations in figure 4.10 are recorded at one point on the cavity bottom. However, the pressure fluctuations also occur laterally around that point on the cavity bottom. Figure 4.13 below shows a plot of the pressure fluctuations in space and time. The y-axis represents the radial distance from the middle of the cavity, with 0 mm being the centre. Every column represents one time step of 0.001 seconds. The colours indicate the pressure in Pascal.

As can be seen, the pressure is in most time-steps the highest at the centre of the cavity bottom. However, fluctuations in space are visible as well, where pressure differences between time-steps at the same location can be as high as 30 bars. The pressure fluctuations shown in figure 4.13 are further used in combination with the FDM Darcy flow solver, to analyse the effect of these fluctuations on a porous rock (see section 4.2.1).

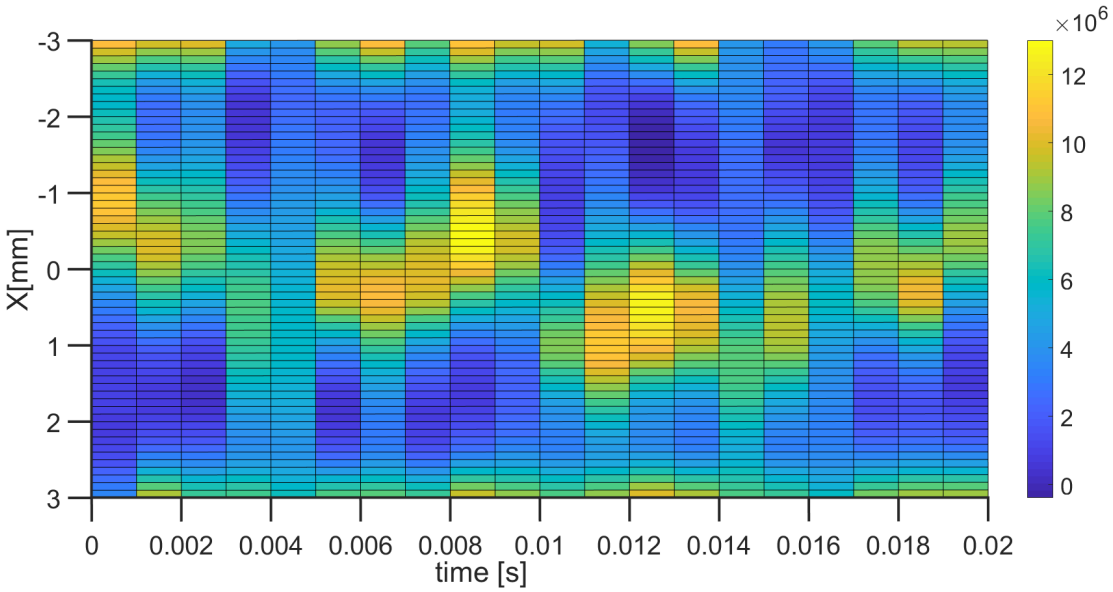

Figure 4.13: Pressure profile at a 10mm cavity bottom in space and time. Every column represents one time step. The y-axis represents the radial distance from the cavity centre (diameter of the cavity) and the colour-bar indicates the pressure in Pascal.

Artificial Fracture

Previous experiments conducted on the BD sandstone showed that the jet could not drill beyond a sealed aluminium adapter of 25mm length. However, it showed that the jet can drill further once a fluid pathway was created ('artificial fracture'). A simulation was run to investigate the difference in pressure (fluctuations) when a similar pathway is created. Figure 4.14 shows the velocity and pressure field of jetting into a 25mm cavity with an artificial fracture. Comparing figure 4.14 above with figure 4.9 shows that the addition of a fluid pathway changes the velocity and pressure field drastically. If there is a fluid pathway, the jet tip can reach the bottom of the cavity. Figure 4.15 shows the pressure recording at the cavity bottom for both cases (with and without fluid pathway). It can be seen that especially the pressure fluctuations are much higher if the fluid has another outflow path. This result confirms the idea that pressure fluctuations are more important than the average pressure.

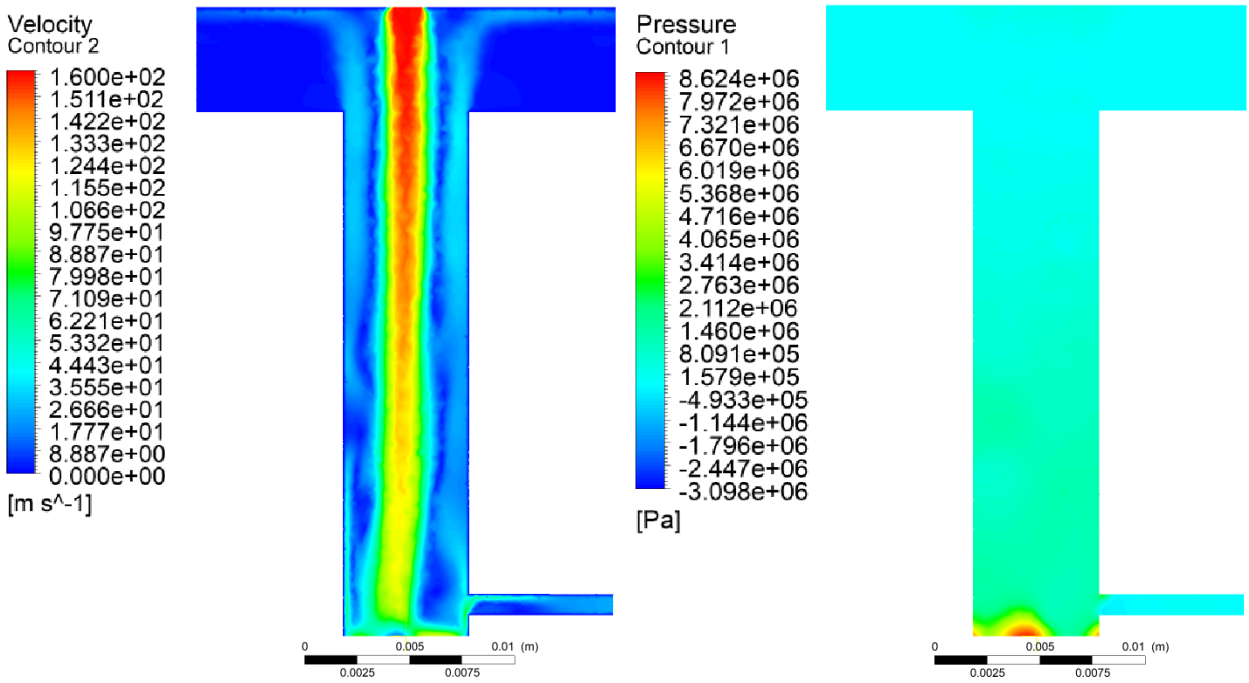

Figure 4.14: Velocity field (left) and pressure field (right) of the simulation of a jet in a cavity of 25mm depth with an artificial fracture similar to experiment (D).

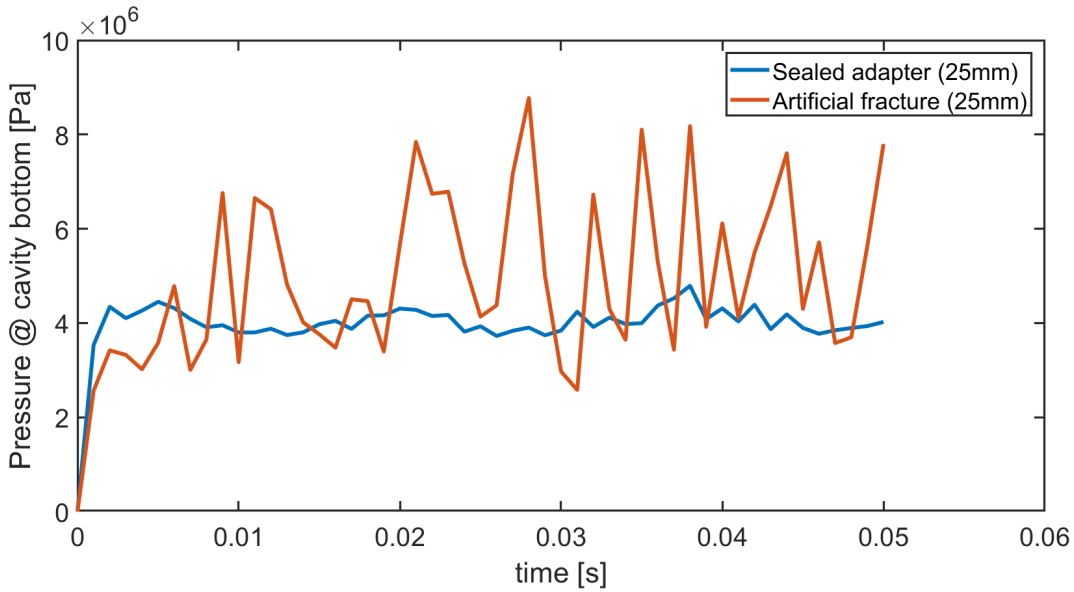

Figure 4.15: Pressure at the cavity bottom with and without an artificial fracture versus time. The pressure fluctuations are much higher if the fluid has another outflow path. The average stagnation pressure in not much higher.

4.2 Destruction Mechanism Results

This section presents the results of experiments and simulations that had the aim to prove or disprove one of the destruction mechanisms, by investigating the effect of pressure fluctuations (hydraulic fracturing and partly poro-elastic tensile failure) and cavitation erosion. First, the results of the FDM simulations in a porous rock are presented. Then, the experiments and simulations about cavitation erosion are discussed. The last section presents the microscopic images and CT-scan of two rock samples; one with cavitation damage and one without cavitation damage.

4.2.1 FDM Simulations for Pressure and Flow in Porous Media

It is experimentally not possible to analyse the pore pressure inside a rock specimen and is therefore analysed numerically. A Finite Difference Method (FDM) was developed to simulate the pressure distribution inside a rock sample. The model was used to evaluate two things: (1) the pressure (fluctuations) in the first layer of pores closest to the impinged area during jetting and (2) the influence of backpressure on the pressure and flow in the impinged area.

Pore Pressure Fluctuations

The results of the experiments and simulations discussed in the previous section (4.1.2) already showed that pressure fluctuations on the cavity bottom are important for the destruction mechanism. But it is also important to analyse the pore pressure *inside* the sandstone during jetting because the difference between pore pressure and cavity bottom are believed to be key for the destruction process.

In order to evaluate the influence of pressure fluctuations of the jet on the pores close to the impinged area, the pressure profiles presented in figure 4.13 are used. Every time step in the FDM solver is also set at 0.001 seconds, such that for every time step a new pressure profile can be implemented. The FDM solver is implemented for slightly compressible fluids, the pore pressure in the first pore layers can still have a different pressure than the jet stagnation pressure at the next time step, as the pores do not reach the steady-state solution instantaneously. If this pressure difference is high enough, the rock can hydraulically fracture. Figure 4.16 shows the pore pressure in the first pore layer together with the stagnation pressure (from figure 4.13) at different times with zero backpressure.
From figure 4.16 it can be seen that the pressure fluctuations of the jet cause pressure differences between the fluid pressure in the cavity and the pore pressures adjacent to the cavity. These fluctuations are needed in order to expel grains in the theorem of hydraulic fracturing (see section 2.6.3). It can also be observed that there are pressure differences between adjacent pores as well, which might help the hydraulic fracturing process.

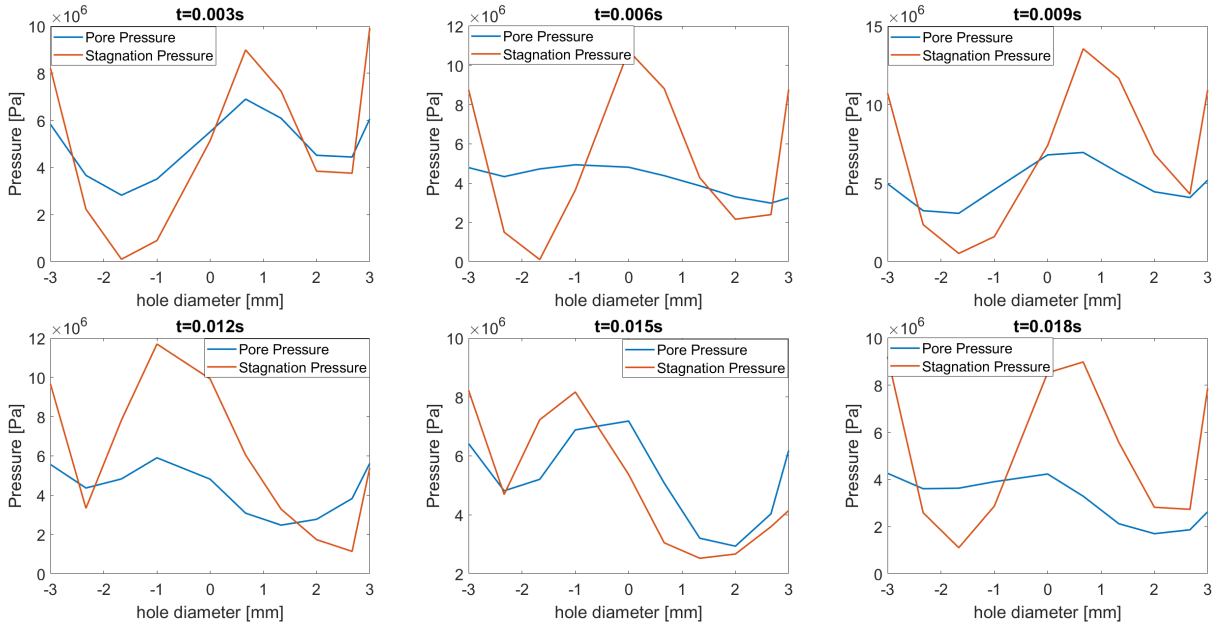

Figure 4.16: The pressure at the cavity bottom in 2D is depicted by the red line. The blue line represents the pore pressure in the first layer of pores adjacent to the location where the jet acts.

Back Pressure Influence

The pore pressure in a reservoir is usually much higher than the pore pressures in rocks at atmospheric conditions. This difference can be one of the reasons why the jetting performance is higher down-hole than in experiments at the surface. That is why it is important to investigate the influence of back pressure inside a rock sample. The FDM model is used to evaluate this influence.

Multiple simulations were run with different back pressures, to see the influence on the pore pressures, especially close to the impinged area (where the destruction is supposed to occur). This section presents the result of increasing the back pressure and its influence on the maximum pressure and maximum pressure difference needed for hydraulic fracturing. The FDM model uses again the jet pressure profiles in time, presented in figure 4.13, but now with different back pressures. Figure 4.17 below shows the 2D pore pressure distribution in a rock sample of 50 x 50mm impinged by a jet, with a back pressure of 0 bar (left) and 200 bar (right)

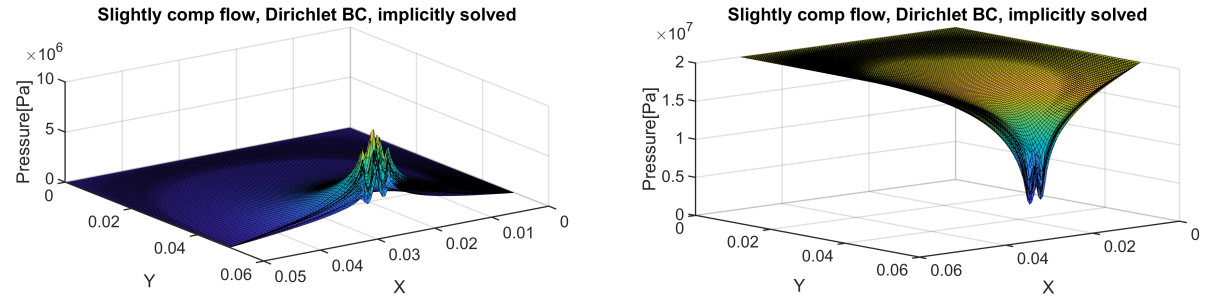

Figure 4.17: Pressure in the 2D simulated porous medium (of 50 x 50mm) impinged by a jet for 0.02 seconds, with a back pressure of 0 bar (left) and 200 bar (right).

Considering the pressure distribution in figure 4.17, it can be seen that the increase in backpressure has an influence on the pore pressure at the impinged area (pore pressure at this area is lower than in the rest of the sample, if the back pressure is high). But as a fluid flows from high to low pressure, it can be stated that the flow towards the cavity is higher when the back pressure is increased. The flow fields at the impinged area are shown in figure 4.18 below. It is clear that the magnitude and amount of outflow towards the cavity is higher when the back pressure is increased. This means that if the back pressure is increased, the location of the pressure differences is more favourable resulting in the expelling of grains towards the borehole.

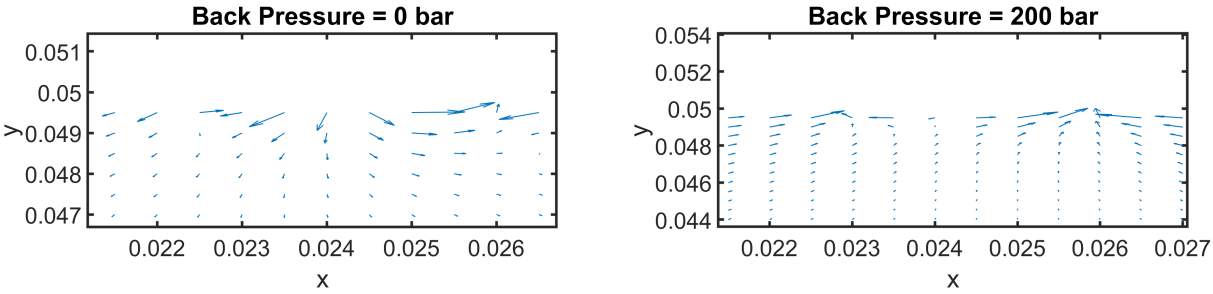

Figure 4.18: Flow field near the impinged area with a back pressure of 0 bar (left) and 200 bar (right).

The maximum pore pressure, the maximum difference in adjacent pore pressures and the maximum difference between the impinged pores and the stagnation pressure are compared for different back pressures. The results are graphically shown in figure 4.19 below. As can be seen, the maximum pore pressure of the impinged cells increases linearly with increasing back pressure. Moreover, the difference between adjacent pores (i.e, grid cells) increases slightly with increasing back pressure (0.6 bar), but not enough to result in a substantial difference in jetting performance. The most important parameter; the maximum difference between the pore pressure of the impinged cells and the jet pressure, first decreases until the back pressure equals the maximum jet pressure and then increases again as the back pressure is larger than the jet pressure. After 25 MPa of back pressure, the maximum difference between pore and back pressure is again larger than its value at 0 MPa. The ideal situation for rock destruction would be a back pressure where the maximum pore-cavity pressure difference is

highest and the maximum pore pressure in the impinged pore is highest. Considering the three graphs in figure 4.19, the ideal back pressure (with a 160 bar nozzle pressure) would be above 25 MPa. Which means that jetting performance only increases if the back pressure exceeds the average stagnation pressure.

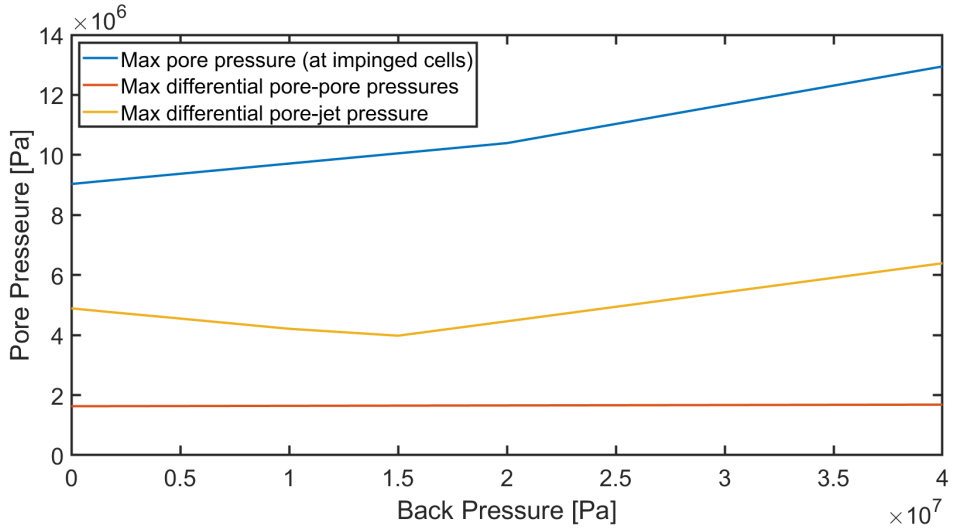

Figure 4.19: Maximum pore pressure of the impinged cells, maximum pore pressure difference, and maximum difference between the pore pressure and jet pressure with increasing back pressure.

4.2.2 Cavitation Erosion

This section presents the results of experiments and simulations on cavitation erosion. The experiments had the aim to investigate whether there is cavitation erosion on the bottom of a cavity. Simulations were carried out in order to see where cavitation is possible, which is then compared to the findings of Kumagai et al. (2011).

Experimental Results

The experiments consisted of jetting into an aluminium adapter, which was placed on top of a polished aluminium plate (see section 3.2.2). A jet is not able to drill through the aluminium plate, but if cavitation occurs (vapour bubbles), the aluminium can be damaged from the implosion of these vapour bubbles. The cavitation erosion can easily be qualitatively detected under a microscope. Figure 4.22 shows the microscopic images of three aluminium plates that were jetted for 60 seconds, with a 5, 15 and 30 millimetres thick adapter on top. Cavitation erosion occurred at all tested depths. However, the erosion seemed to increase with increasing depth. The erosion at 30mm was more severe than the erosion at 5mm depth (see figure 4.22). Although cavitation occurs at 25mm depth, it does not seem to destruct the rock at this depth because the jet was not able to drill beyond the 25mm adapter in experiment (B) (see section 4.1.1). That is why it is concluded that cavitation erosion is not the governing destruction mechanism in sandstones jetted with a nozzle pressure of 160 bar.

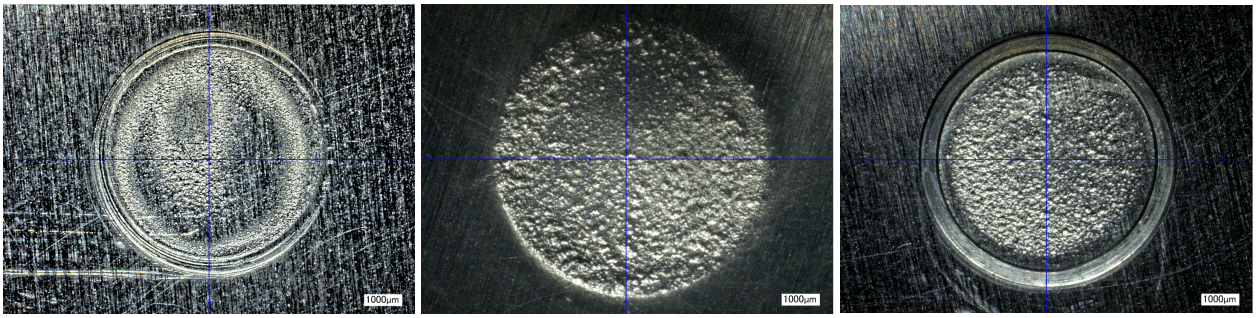

Figure 4.20: Cavitation erosion at 5, 15 and 25mm depth, from left to right respectively. Imaged with a microscope.

Simulation Results

Simulations were carried out to investigate at which location cavitation can happen, on both a flat surface and inside a cavity. The result of cavitation on a flat surface is shown in figure 4.21b next to the results of Kumagai et al. (2011). It can be seen that the potential cavitation location is around the area of where the jet hits the surface, in a ring-like shape. There is therefore no cavitation at zero cavity depth, which proves again that cavitation is not the governing mechanism damaging the rock, at zero cavity depth at least.

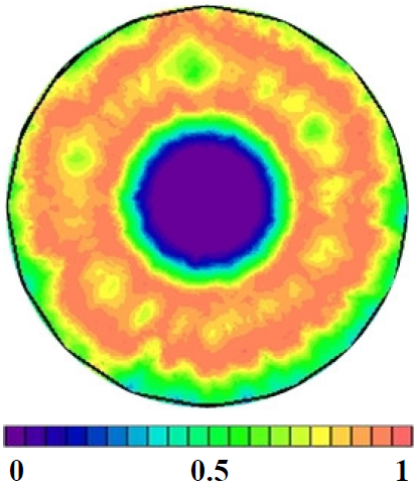

(a) Location of potential cavitation erosion, numerically simulated by Kumagai et al. (2011).

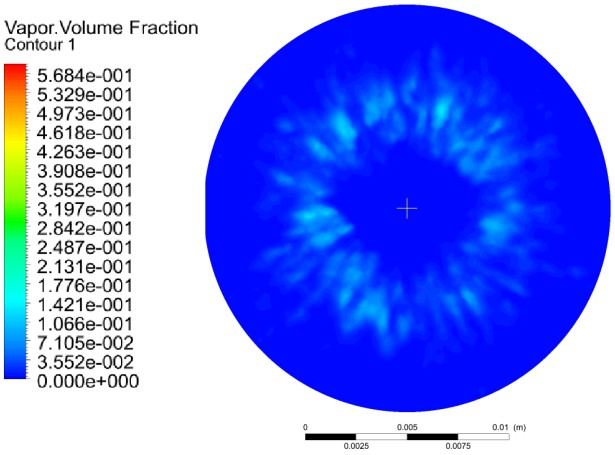

(b) Location of possible cavitation erosion on a flat surface, numerically simulated with the *Ansys* software.

Figure 4.21: Location of potential cavitation erosion. Both the *Ansys* simulations as the simulations from Kumagai et al. (2011) show a ring-like pattern around the area where the jet impinges the surface. Experiments confirm this result (Kumagai et al. (2011), Hahn et al. (2019)).

Simulations were also run to investigate the location of the potential cavitation erosion inside a cavity. The experiments showed that there is cavitation erosion on the cavity bottom, at least down to a depth of 30mm. Two simulations were run, one at 10mm and one at 30mm cavity depth. The vapour volume fractions in both fluid bodies are shown in figure

4.22 below. The vapour bubbles do not exist at the cavity bottom in both simulations, which is contradicting with the experiments that showed cavitation erosion at these depths. The simulations show the formation of vapour bubbles only, they could possibly travel further and still implode at the surface of the cavity bottom. Another reason for the discrepancy between the simulations and experiments can be that the setting at which pressure vapour bubbles form is too high (3540 Pa) resulting in less cavitation in the simulation. It is is also important to consider that cavitation erosion is a time-integrated process, and the simulations show only a time step of 1 millisecond. Hence, the location of the bubbles might change at different time steps.

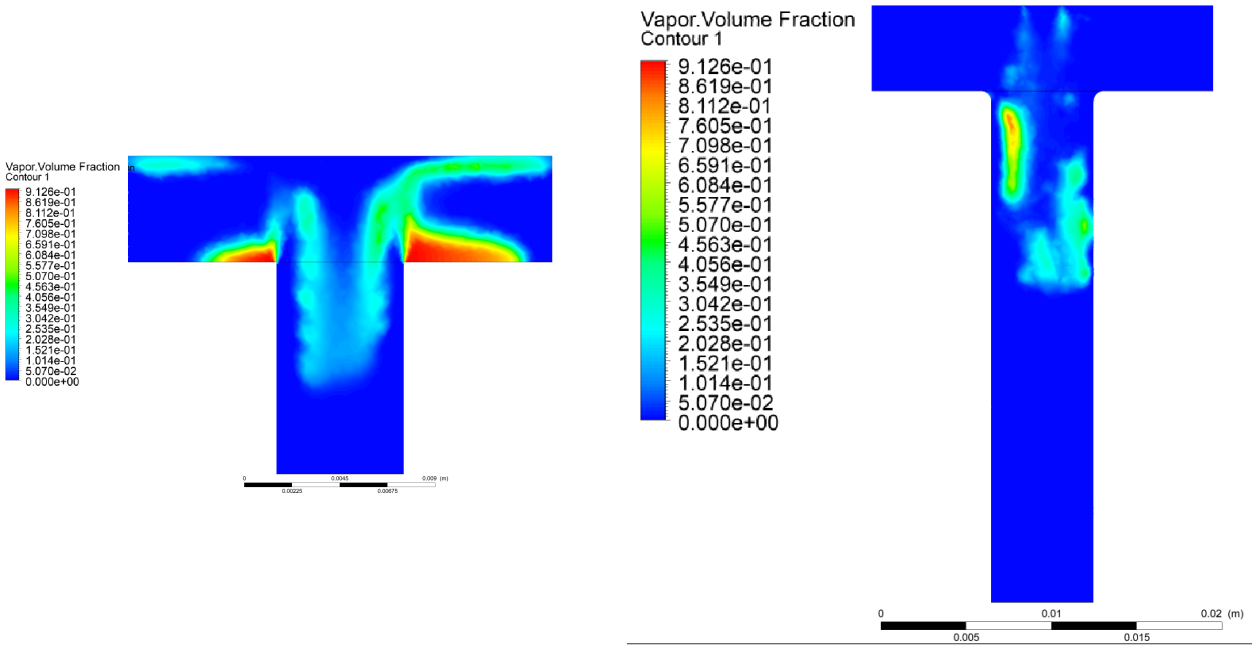

Figure 4.22: Location of potential cavitation inside a cavity of 10mm (left) and 25mm (right).

4.2.3 Analysis of the Jetted Rocks

Two Bad Durkheim sandstone samples were analysed under the microscope and imaged by a CT-scanner. One sample had a hole drilled by the water jet, taken from experiment (A). The other sample is the one shown in figure 2.7b, where the impinged area was filled with glue. This second sample was interesting because the damage on the rock around the filled area was definitely eroded by cavitation erosion Hahn et al. (2019). The hypothesis was that a one could distinguish between cavitation erosion and a non-cavitating erosion on grain scale. Figure 4.23 shows the microscopy images of three parts of the rock; (1) eroded part by cavitation, (2) undamaged rock part and (3) damaged by a water jet. There is no difference visible between the three images.

Figure 4.24 shows the CT images of part of the BD sandstone; one image was taken at the edge of the cavitation damage (left photo) and the other image was taken close to the jetted hole (right photo). Unfortunately, not much difference between cavitation erosion and undamaged rock or jetted rock is visible in terms of grain damage. However, it seems that

the porosity is slightly higher around the jetted borehole, compared to the porosity around the cavitation damage. This must be confirmed by post-processing of the images and by quantification of the pore space and the grain size as it is contradicting to the findings of Bakker and Barnhoorn (2019), who showed that the porosity near the jetted hole did not change.

Figure 4.23: Microscopic images of Bad Durkheim samples. From left to right: sample with cavitation erosion, undamaged sample and a sample with a jetted hole. Not much difference is visible.

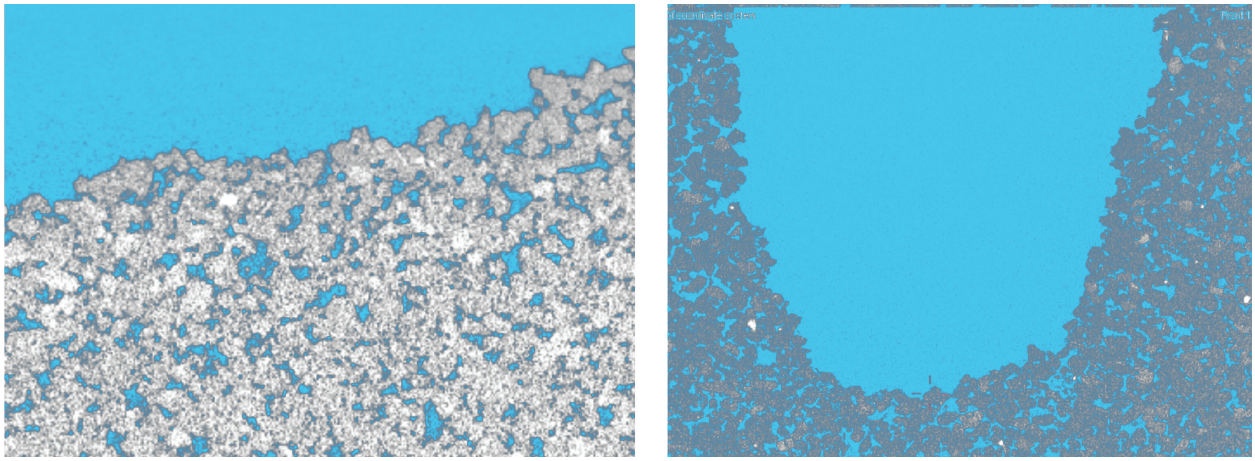

Figure 4.24: CT-scan images. Left: part of a sample damaged by cavitation erosion. Right: a sample with a jetted cavity. The blue colour is added to make the pores more visible. It seems that the jetted cavity has a higher porosity.

4.3 Jetting Correlation

The experimental and numerical results obtained in the previous discussed section show that the drilling is highly dependent on pressure fluctuations. It is also shown that cavitation can not be the governing destruction mechanism. And Buset et al. (2001) already proved that shear forces are not the governing mechanism. It is therefore concluded that the governing destruction mechanism in our experiments is hydraulic fracturing (pore over-pressure) in combination with theorem of pore-elastic tensile failure (pressure fluctuations). It was tried to capture the results and this conclusion into a usable correlation: the jetting correlation.

The jetting correlation is an analytical formulation that aims to predict whether a rock is jettable or not. When the grain size, porosity and UTS are available, the correlation can estimate the time needed to erode one layer of grains. If pressure versus depth data are known, the correlation also estimates the maximum jettable depth, with a static nozzle. The correlation is based on the theorem of hydraulic fracturing in combination with pressure fluctuations and is mathematically derived in section 3.3 of which the result is shown below in 4.1

$$P_s(1 - e^{-\frac{t}{1/Q*\Delta V}}) = \frac{UTS\left[\pi\left(\frac{r_g^2(\frac{4}{\sqrt{3}}r_g - 6\pi)(0.2595-\phi)}{18}\right)\right]^{2/3}}{\left(24\pi r_g^2 - 1.1675\left[\pi\left(\frac{r_g^2(\frac{4}{\sqrt{3}}r_g - 6\pi)(0.2595-\phi)}{18}\right)\right]^{2/3}\right)\sin 60} \tag{4.1}$$

Where P_s is double the amplitude of the fluctuations in stagnation pressure, t the time Q the volumetric flowrate, UTS the Ultimate Tensile Strength, r_g the grain diameter and ϕ the porosity of the rock. The left hand side of the equation calculates the pore pressure build up over time. The right hand side calculates a pore pressure threshold at which the grains are expelled from the rock. Enabling one to calculate the time (t) needed to erode one layer of grains. The properties of the Bad Durkheim, Dortmund and Gildehaus sandstones are used to predict the maximum jetting depth and then compared to the experimental results.

4.3.1 Prediction & Validation

The properties of the three sandstones used for the jetting correlation are shown below in table 4.2. The pressure (P_s), which is actually the pressure fluctuation, is obtained from the previously presented results of the *Ansys* simulations (see figure 4.10). Figure 4.25 shows the depth in time estimated by the jetting correlation (blue line), together with the depths obtained from experiments (dots).

Table 4.2: Properties of the three sandstones which are also used for the jetting experiments.

	UTS [MPa]	porosity (%)	grain diameter [mm]	permeability [mD]
Bad Durkheim	2.9	19.5	2	450
Dortmund	7.2	8.7	0.5	0.018
Gildehaus	3.5	23.7	2	6300

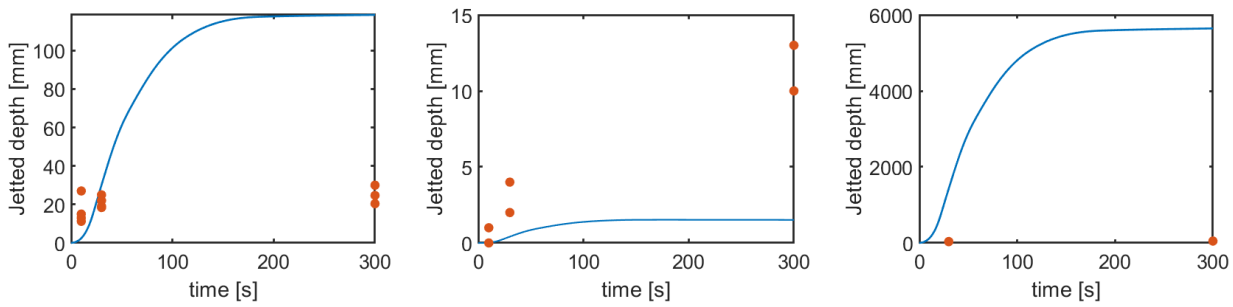

Figure 4.25: Depth versus time estimated by the jetting correlation, together with the experimental results. For the Bad Durkheim, Dortmund and Gildehaus sandstone from left to right respectively.

It is clear that the jetting correlation shown in figure 4.25 is not accurate in estimating the maximum depth. However, the correlation has been adjusted in order to fit the maximum jetting depth with the experimental data. ΔL of the Darcy-Weisbach equation (equation 3.14) was changed until the correlation was matching the experimental results. This ΔL was then plotted against the permeability k, which resulted in a straight line on log-log scale (see figure 4.26).

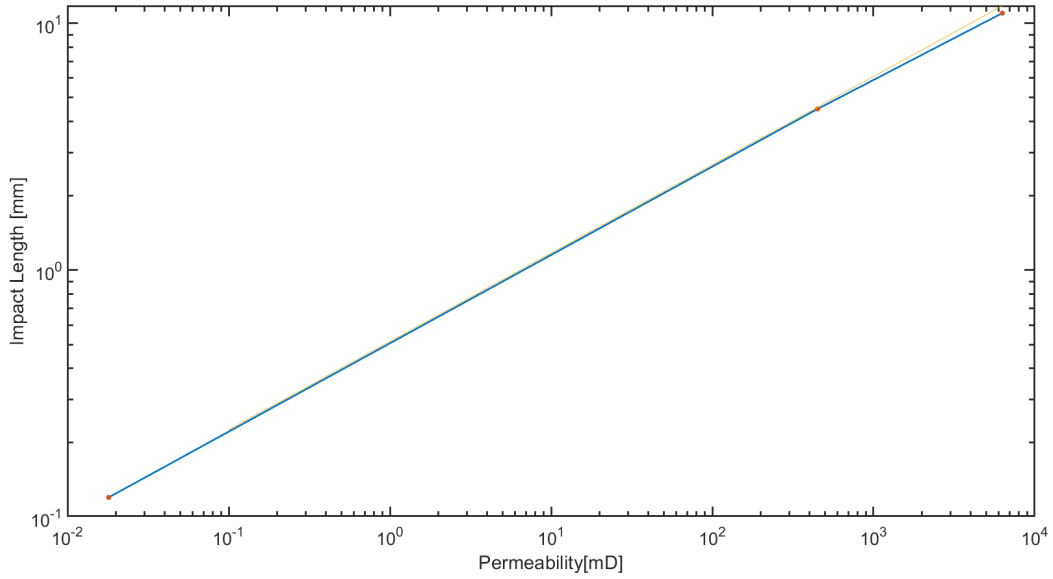

Figure 4.26: ΔL plotted against permeability of the different rocks on a log-log scale, resulting in a linear correlation.

Adjusted Jetting Correlation

Since the value of ΔL can be estimated with the use of the graph in figure 4.26, the jetting correlation has to be adjusted according to this relation. From the graph, the following equation for ΔL is formulated:

$$\Delta L(k) = k^m * 10^b \tag{4.2}$$

Where b is the intersect point on the log-log plot which is $b = 0.289mm$ and m the slope of the graph which is defined as:

$$m = \frac{log(L2/L1)}{log(k2/k1} = \frac{log(11/0.12)}{log(6300/0.018)} = 0.3579$$

So the final jetting correlation becomes:

$$P_s(1 - e^{-\frac{t}{1/Q*\Delta V}}) = \frac{UTS\left[\pi\left(\frac{r_g^2(\frac{4}{\sqrt{3}}r_g - 6\pi)(0.2595-\phi)}{18}\right)\right]^{2/3}}{\left(24\pi r_g^2 - 1.1675\left[\pi\left(\frac{r_g^2(\frac{4}{\sqrt{3}}r_g - 6\pi)(0.2595-\phi)}{18}\right)\right]^{2/3}\right)\sin 60} \tag{4.3}$$

where Q is expressed as follows:

$$Q = \frac{\pi * D^4}{128\mu}\frac{\Delta P}{k^{0.3579} * 10^{-0.289}} \tag{4.4}$$

The final adjusted jetting correlation is graphically shown in figure 4.27, for the three tested sandstones. The correlation predicts the maximum jetting depth accurately, however the ROP in the beginning does not fit the data except for the Dortmund sandstone. The accuracy of the adjusted jetting correlation indicates that hydraulic fracturing is the governing mechanism, as the correlation is fully based on this theorem. As the correlation is validated with only three sandstones, more experiments should be conducted in the future.

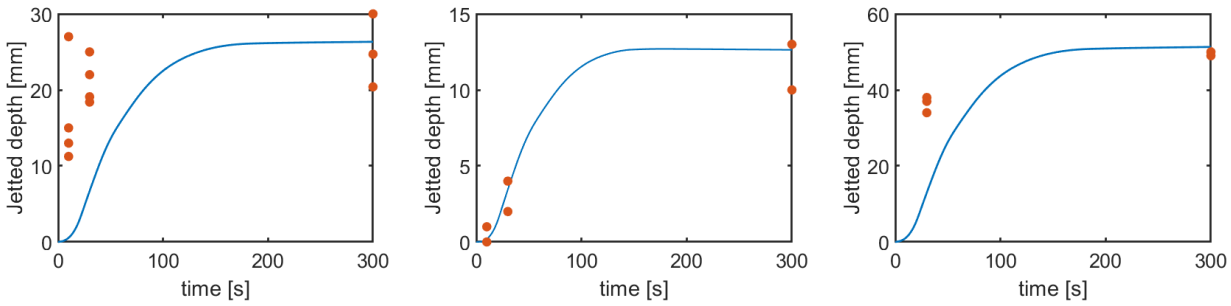

Figure 4.27: Depth versus time estimated by the adjusted jetting correlation, together with the experimental results. For the Bad Durkheim, Dortmund and Gildehaus sandstone from left to right respectively.

5. Conclusions

The purpose of this study was to investigate the destruction mechanism of a rock during high pressure water jetting. In order to understand this process, it was important to first find the relation between stagnation pressure and cavity depth. With this relation, an optimum nozzle-rock distance can be found and applied in the field. Experiments were conducted to find the maximum jettable cavity depth (with a static nozzle) as well as the effect of hole diameter and friction on the jetting performance. Experiments were performed on three different sandstones; the Bad Durkheim, Dortmund and Gildehaus sandstone. The experiments showed that the jetting process stops at a certain maximum cavity depth. When the hole diameter was increased, or when an extra fluid pathway was made, the jet was able to drill further than the first measured maximum cavity depth. That means that efficient fluid relief (discharge of the water standing inside the cavity) causes the jet to drill faster and further, because the energy of the jet is then completely focused on the cavity bottom rather than dissipated in pushing fluid out of the cavity.

The experiments gave information at which depth the jetting stops, but do not give information about the magnitude of the fluid pressure at the cavity bottom. Computational Fluid Dynamics (CFD) simulations were carried out to quantify this pressure. The simulation had the aim to find a continuous relation between the fluid pressure at the cavity bottom and cavity depth. Multiple cavity depths were simulated, ranging from 0 to 40mm depth, for 0.02 seconds. The pressure was recorded in the middle of the cavity bottom, for all cavity depths, in order to obtain the relation between pressure and depth. The simulations showed that the pressure decreases with increasing cavity depth (except for the first mm, where the maximum pressure increases) as expected. The pressure fluctuations, which are believed to be important in the theorem of hydraulic fracturing and poro-elastic tensile failure, increased drastically in the first millimetres, due to turbulence, which is not existing at 0mm depth. After 5mm depth, the fluctuations decreased with increasing cavity depth, due the damping effect of the water column inside the cavity. The pressure fluctuations were present in time, but also in space (laterally across the cavity bottom), which enhances the process of hydraulic fracturing even more.

Furthermore, a simulation was run with an artificial fracture (i.e a fluid pathway), where the fluid could escape (similarly to experiment (D)), resulting in a more focused jet. The simulations showed that the average stagnation pressure (over time) in the presence of a fracture was slightly increased. The pressure fluctuations increased drastically compared to a cavity without a fracture. Therefore, it is concluded that the fluctuations in pressure are key for efficient destruction of a porous rock.

The pressure-depth relationship obtained from the simulations only provided the fluid pressure *on* the rock. To understand the jetting process, it is also important to analyse the pressures *inside* the rock (i.e, pore pressure), during jetting. As it is not possible to experimentally measure the pore pressure inside a rock, it was approached numerically using the Finite Difference Method (FDM). The FDM solver was used to (1), analyse the pore pressure fluctuations as a reaction to the jet fluctuations and (2), investigate the effect of applying an increased pore pressure on the whole sample (i.e, back pressure). The applied jetting pressure was obtained from the previously obtained pressure fluctuations and coupled to this FDM solver in order to evaluate the influence of these pressure fluctuations inside a rock. The simulations showed that the pressure difference between the first layer of pores (adjacent to the 'cavity bottom') and the fluid pressure of the jet were significant. This pressure difference is especially important in the theorem of hydraulic fracturing, which requires this difference in order to expel the grains associated with this high pore pressure.

Since the pore pressure in a reservoir is much higher than at atmospheric conditions (at which experiments were conducted), it is also important to investigate the effect of an increased pore pressure, which was also analysed with the FDM solver. The pressure was analysed in the first grid cells adjacent to the applied jet pressure (i.e first layers of pores). The analysis showed that an increase in backpressure causes a linear increase in maximum pore pressure of these first layers of pores. Furthermore, the maximum pressure difference between pores did not change significantly. The most important parameter, the pressure difference between pores and the cavity, decreased first until the average jet stagnation pressure was reached. But when the back pressure was increased more, this pressure difference increased again. After an applied back pressure of 250 bar, this pressure difference was higher compared to the case with 0 bar back pressure. Hence, it is concluded that if the back pressure is higher than the average stagnation pressure on the cavity bottom, the jetting performance increases. This might be one of the reasons why the jetting performance (ROP) is higher in the field at reservoir conditions.

Buset et al. (2001) already stated that surface erosion due to shear forces is most probably not the governing destruction mechanism during jetting. Furthermore, at the stagnation point, the fluid velocity is zero, resulting in zero shear stress as well. Hahn et al. (2019) performed experiments which proved that cavitation cannot be the destruction mechanism at zero cavity depth. This was confirmed by a study of Kumagai et al. (2011), that performed experiments and numerical simulations of jetting on a flat surface. Because the effect of cavitation erosion was still not completely rejected in the literature and cavitation erosion *inside* a cavity was not yet evaluated, we decided to perform experiments and simulations on this mechanism as well.

Experiments were performed where a jet was impinging an aluminium plate, but with an adapter placed on top of this plate with a hole to allow the jet to reach the aluminium plate. The adapters had a thickness ranging from 5 to 30mm. The cavitation erosion was clearly visible on the aluminium plates, in all experiments. There was a slight increase in cavitation erosion with increasing cavity depth. The jetting experiments on the Bad Durkheim for example, showed that the destruction by jetting, with the same type of adapter, stopped at

25mm. Hence, it was concluded that although cavitation erosion occurs at 25mm depth, it is not enough to destruct the rock as the experiments (C) showed. Hence, cavitation is not the governing erosion mechanism.

A simulation was carried out to investigate the location where cavitation can happen when jetting on a flat surface. The results showed that cavitation can only occur around the impinged area, creating a ring-like shape (with an inner diameter of 5mm, which is similar to the numerical simulation results in the study of Kumagai et al. (2011). Simulations of cavitation inside a cavity showed cavitation is present inside a cavity, but not at the cavity bottom, which is contradicting to the findings of the experiments that showed cavitation erosion at the bottom. This discrepancy can be due to convergence problems as the grid size of the mesh was not small enough (due to limitations in the student licence of the software) to accurately simulate multi-phase flow, or because the time span of the simulation was not long enough (cavitation erosion is a time-integrated process).

CT-scan images of the rock did not show a difference in grain damage between a jetted hole and a sample where cavitation erosion had occurred. However, there was qualitatively a difference in porosity visible, which is contradicting to the findings of Bakker and Barnhoorn (2019) who stated that there is no difference in porosity in the vicinity of the jetted hole, compared to an undamaged rock. Further analysis of the scans have to be carried out in order to provide a definite conclusion on whether there is a difference or not.

Based on the results found in this study, it is concluded that pressure fluctuations are essential in the rock destruction process. Buset et al. (2001) already stated that surface erosion due to shear forces is not the governing destruction mechanism, and this study showed that cavitation erosion is also not the governing during destruction. Poro-elastic tensile failure is not evaluated in this study, but is essentially interconnected with the hydraulic fracturing theorem as it is also based on pore pressure fluctuations. So based on this study, the governing destruction mechanism is expected to be hydraulic fracturing, where the pressure fluctuations are essential.

This conclusion together with the results is captured in a formula, called the jetting correlation (equation 4.3). The jetting correlation predicts whether a rock is jettable or not. The correlation was also able to predict the maximum jettable depth (with a static nozzle) when combined with the pressure-depth relationship. With an empirical relation for impact length (the distance to where the stagnation pressure is influencing the pore pressure in the rock), obtained from experimental results, the jetting correlation was able to predict the maximum depth accurately when compared to the experimental results. This validates that the destruction mechanism is indeed hydraulic fracturing. However, it was only tested on three different rocks. More experiments should be conducted in the future to further validate the correlation.

To conclude, the final results and conclusions derived from this study are listed below:

- **Pressure fluctuations are key in the destruction process of porous rocks:** The water jet is most effective at a distance between nozzle and rock where the pressure fluctuations are highest. Designing the nozzle backward jets accordingly can improve jetting time drastically. Furthermore, rotating nozzles can be designed such that the

fluctuations (one rotation equals one fluctuation) are most efficient.

- **Back pressure has an influence on jetting performance:** Based on numerical simulations, the jetting performance will increase if the reservoir pressure is higher than the average stagnation pressure of the jet. Changing the nozzle pressure accordingly can potentially result in a higher ROP and save pumping energy.
- **Hydraulic fracturing is the governing destruction mechanism of a porous rock during high pressure water jetting:** By knowing that hydraulic fracturing (in combination with pressure fluctuations) is the governing destruction mechanism, the jettability of porous rocks can be estimated. A correlation is developed (equation 4.3) which predicts the time needed to erode one layer (if the outcome is an infinite time, jetting is not feasible).

6. Recommendations

Due to time and/or financial restrictions, some of the initially proposed experiments could not be carried out and were replaced by simulations. These simulations are very useful to investigate the qualitative behaviour of a physical problem, but are however not the exact solution. It is recommended validate the simulations with further experiments. Moreover, more experiments are needed in order to prove the conclusions made in this study, especially using different porous rocks. The proposed recommendations are discussed further in this chapter.

Experiments on More Rocks Samples

In this study, only three different sandstones were used. Further research should test more porous rocks (with more clay content for example), but also non-porous rocks. Furthermore, the experiments should ideally be conducted with a start-stop mechanism (a pneumatically controlled steel plate which can be pushed between the nozzle and the rock), to control the jetting exposure time more accurately. In this way the ROP can be measured as well, which can later be combined with pressure data at the depth of highest ROP. Furthermore, thede data could be used to validate or improve the jetting correlation (equation 4.3).

Pressure-Depth measurements

During this project, the aim was to measure the relation between stagnation pressure and depth. An experimental setup is designed to measure the pressure of the jet on the cavity bottom. The designed apparatus is shown in figure 6.1 below. In the proposed experiment, an aluminium cylinder with a cylindrical cavity is created where a piston can move freely inside this cavity. A force-sensor is attached to the bottom of the piston in order to measure the pressure exerted on the piston by the jet. The nozzle will have a constant stand-off distance from the top of the main cylinder, while the piston is moved to simulate different depths. This way, a stagnation pressure versus depth relationship can be established. The pressure sensor design is a challenging part in this proposed setup because it has to withstand very high pressures, and at the same time have a very high sampling rate (>32kHz). These pressure sensors can be made, but are very expensive. Because of this and the time restrictions of this study, we decided to approach the pressure depth relation numerically. However, these numerical simulations are not the exact solution. Therefore, experiments should be carried out in the future to get the exact relationship.

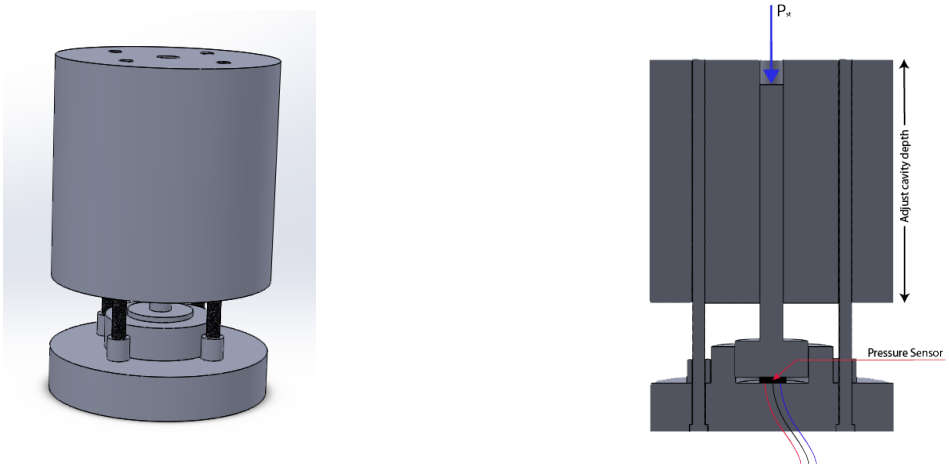

(a) Aluminium apparatus with an adjustable cavity depth

(b) Crossection of the apparatus, force sensor is placed right under the piston

Figure 6.1: Setup for the stagnation pressure measurements at different depth, adjustable depth from 0mm to 80mm

Back Pressure Increase

In this study, the increase in back pressure is analysed by numerically simulating the effect of back pressure in a sample. It was concluded that an increase in back pressure can positively affect the jetting performance. However, this should be validated with experiments which can be performed at the International Geothermal Centre in Bochum that has a vessel called the 'mini-iBOGS' in which the pressure (i.e., back pressure) can be increased up to 500 bar. Previous experiments in this mini-iBOGS showed that the ROP and maximum jetting depth decreased when the back pressure was increased (personal contact with GZB employees and my own experience (not included in this study)). This can be due to two things: (1), the back pressure was not high enough, and as simulations showed, the back pressure needs to be above the average stagnation pressure in order to increase jetting performance and (2), in the previous experiments, the backpressure was increased in the whole vessel, effectively taking away the potential pressure difference needed for hydraulic fracturing to work. In order to simulate subsurface conditions more realistically, the experimental setup has to be changed by making two chambers in the mini-iBOGS rather than one. The top chamber where the jetting occurs is held at a low pressure while the bottom chamber, where the rock is situated, has a high pressure. The proposed setup is illustrated in figure 6.2a.

The rock sample is held in an aluminium disk which is also the seal between the two chambers (see figure 6.2b). The aluminium disk has a hole of 6mm in the middle in order to jet the rock sample. In order to generate two different pressures, two pumps and two pressure valves are attached to the mini-iBOGS (see figure6.2a). Although the pressure gradient is linear from high to low pressures (from bottom chamber to top chamber, through the little hole in the disc), the backpressure will have an effect when the jetting starts as the first layer of pores is loaded from both sides, as the simulations showed in section 4.2.1. It is recommended to validate the simulations by conducting experiments using this adjusted mini-iBOGS experimental setup of which the parts are already manufactured.

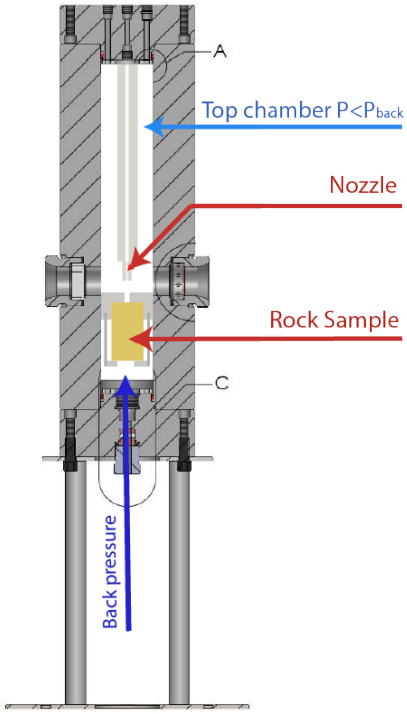

(a) Cross-sectional view of the proposed setup in the mini-iBOGS. The rock is jetted from above where there is a low pressure, while the bottom chamber with the sample has a high pressure.

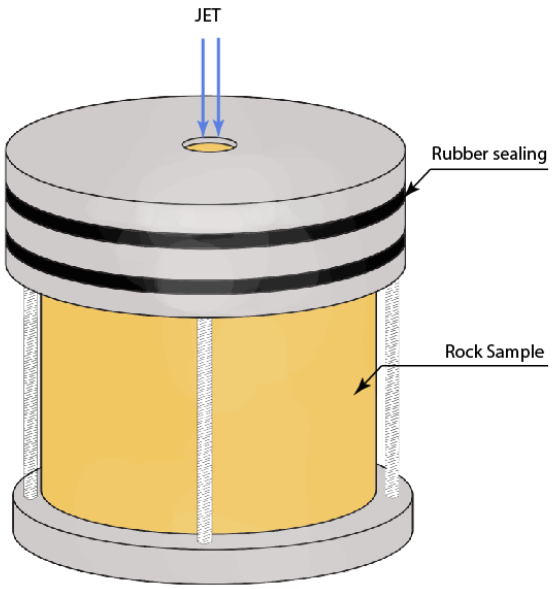

(b) Aluminium sample holder and sealing between the two pressure chambers of the mini-iBOGS showed on the left. There is a small hole in the aluminium disc to jet the rock.

Figure 6.2: Setup of the back pressure experiments (left) and the aluminium disc placed in the middle of the mini-iBOGS to create two chambers which have a different pressure

Analysis of Jetted Rocks

The analysis of the rocks in this study was only qualitative. Further research should include the numerical analysis of these rock samples. It is also recommended that thin sections are made to analyse the grains with a higher resolution in the CT-scanner and under a microscope. In further research it would especially be interesting to quantify the porosity of the rock in the vicinity of the jetted hole, compared to rocks which have been eroded by shear forces and/or cavitation erosion.

Bibliography

R. Bakker, S. Hahn, M. Friebel, D. F. Bruhm, T. Reinsch, and A. Barnhoorn. A laboratory study on radial water jet drilling in true triaxial stress conditions. unpublished, 2019.

R. R. Bakker and A. Barnhoorn. Multiscale evaluation of potential damage in jetted lateral boreholes. *International Journal of Rock Mechanics and Mining Sciences*, 121:104007, 2019.

S. Ben Hamida, V. Srivastava, M. Sillanpää, M. Shestakova, W. Tang, and N. Ladhari. Eco-friendly bleaching of indigo dyed garment by advanced oxidation processes. *Journal of Cleaner Production*, 158, 04 2017. doi: 10.1016/j.jclepro.2017.04.166.

G. Blöcher, E. Peters, and T. Reinsch. Sure report on deliverable version 10/31/2016 project sure-grant-number 654662 page 1/55. 2016.

M. A. Bruni, J. H. Biasotti, G. D. Salomone, et al. Radial drilling in argentina. In *Latin American & Caribbean Petroleum Engineering Conference*. Society of Petroleum Engineers, 2007.

P. Buset, M. Riiber, A. Eek, et al. Jet drilling tool: cost-effective lateral drilling technology for enhanced oil recovery. In *SPE/ICoTA Coiled Tubing Roundtable*. Society of Petroleum Engineers, 2001.

C. R. Chamorro, J. L. García-Cuesta, M. E. Mondéjar, and A. Pérez-Madrazo. Enhanced geothermal systems in europe: An estimation and comparison of the technical and sustainable potentials. *Energy*, 65:250–263, 2014.

S. D. Cinelli, A. H. Kamel, et al. Novel technique to drill horizontal laterals revitalizes aging field. In *SPE/IADC Drilling Conference*. Society of Petroleum Engineers, 2013.

B. Goldstein, G. Hiriart, J. Tester, B. Bertani, R. Bromley, L. Gutierrez-Negrin, E. Huenges, H. Ragnarsson, A. Mongillo, M. Muraoka, et al. Great expectations for geothermal energy to 2100. In *Proceedings, Thirty-Sixth Workshop on Geothermal Reservoir Engineering, Stanford University, Stanford, CA, Jan*, 2011.

D. Gradzki, S. Hahn, S. Jasper, V. Wittig, R. Lindken, and R. Bracke. High pressure jetting in various rocks—investigation of failure mechanism and development of drilling process. In *Innovation-Based Development of the Mineral Resources Sector: Challenges and Prospects: Proceedings of the 11th Russian-German Raw Materials Conference, November 7-8, 2018, Potsdam, Germany*, page 65. CRC Press, 2018.

M. Grant. *Geothermal reservoir engineering*. Elsevier, 2013.

S. Hahn and V. Wittig. Jet drilling at ambient conditions. *SURE Deliverables*, 2017.

S. Hahn, S. Jasper, V. Wittig, and R. Bracke. Investigations on the erosion mechanism of radial jet drilling. unpublished, 2019.

S. Hurter and R. Haenel. Atlas of geothermal resources in europe. 2002.

W. H. Isay. *Kavitation*. Schiffahrts-Verl." Hansa" Hamburg, 1989.

Y. Jun, C. Mingyue, H. Anle, J. Weidong, and L. Chong. Study and application of hydraulic jet radial drilling in carbonate reservoirs. *International Journal of Oil, Gas and Coal Engineering*, 6(5):96, 2018.

K. Kumagai, S. RYU, K. Fujishima, T. Kazama, and J. Ke. Evaluation of cavitation erosion under submerged jet with cfd. In *Eighth JFPS International Symposium on Fluid Power*, pages 116–121, 2011.

J. W. Lund, D. H. Freeston, and T. L. Boyd. Direct utilization of geothermal energy 2010 worldwide review. *Geothermics*, 40(3):159–180, 2011.

W. C. Maurer, J. K. Heilhecker, et al. Hydraulic jet drilling. In *Drilling and Rock Mechanics Symposium*. Society of Petroleum Engineers, 1969.

M. Medetbekova, S. Salimzadeh, H. Christensen, and H. Nick. Stability analysis of radial jet drilling in chalk reservoirs. In *Poromechanics VI*, pages 1842–1849. 2017.

A. Momber. Cavitation damage to geomaterials in a flowing system. *Journal of materials science*, 38(4):747–757, 2003.

J. N. Moore and S. F. Simmons. More power from below. *Science*, 340(6135):933–934, 2013.

K. Peng, S. Tian, G. Li, and H. Alehossein. Mapping cavitation impact field in a submerged cavitating jet. *Wear*, 396:22–33, 2018.

E. Peters, J. Veldkamp, M. Pluymaekers, F. Wilschut, S. A. W. BV, K. Aardwarmtecluster, K. V. B. BV, and C. W. G. BV. *Radial drilling for Dutch geothermal applications*. Utrecht: TNO, 2015.

A. M. S. Ragab. Improving well productivity in an egyptian oil field using radial drilling technique. *Journal of Petroleum and Gas Engineering*, 4(5):103–117, 2013.

G. Rehbinder. A theory about cutting rock with a water jet. *Rock mechanics*, 12(3-4): 247–257, 1980.

T. Reinsch, B. Paap, S. Hahn, V. Wittig, and S. van den Berg. Insights into the radial water jet drilling technology–application in a quarry. *Journal of Rock Mechanics and Geotechnical Engineering*, 10(2):236–248, 2018.

N. Sabatakakis, G. Koukis, G. Tsiambaos, and S. Papanakli. Index properties and strength variation controlled by microstructure for sedimentary rocks. *Engineering Geology*, 97 (1-2):80–90, 2008.

Appendices

A. Nozzle Design

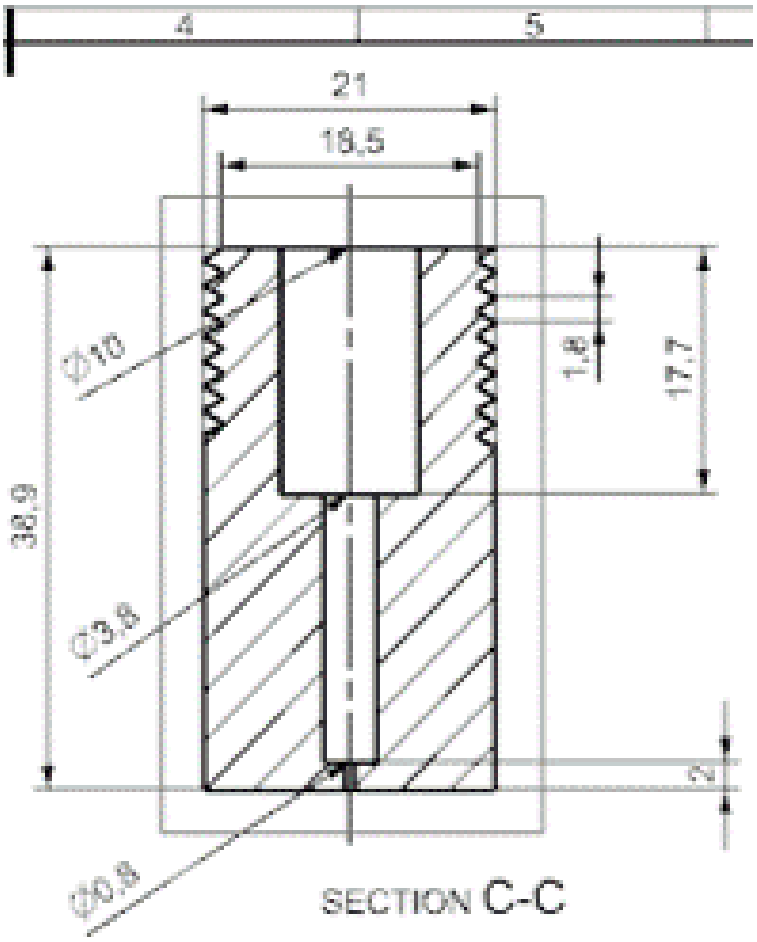

Figure A.1: Cross-sectional view of the nozzle used in the Experiments throughout this study.

B. Turbulence Models

B.0.1 K-epsilon

The $k-\epsilon$ model is commonly used in CFD analysis. It consist of two PDE's, turbulence kinetic energy (k) and dissipation (ϵ). These equations are shown below.

$$\frac{\partial(\rho k)}{\partial t}+\frac{\partial(\rho k u_i)}{\partial x_i}=\frac{\partial}{\partial x_j}\left[\frac{\mu_t}{\sigma_\epsilon}\frac{\partial k}{\partial x_j}\right]+2\mu_t E_{ij}E_{ij}-\rho\epsilon \tag{B.1}$$

$$\frac{\partial(\rho \epsilon)}{\partial t}+\frac{\partial(\rho \epsilon u_i)}{\partial x_i}=\frac{\partial}{\partial x_j}\left[\frac{\mu_t}{\sigma_\epsilon}\frac{\partial \epsilon}{\partial x_j}\right]+C_{1\epsilon}\frac{\epsilon}{k}2\mu_t E_{ij}E_{ij}-C_{2\epsilon}\rho\frac{\epsilon^2}{k} \tag{B.2}$$

This model is accurate at estimating turbulence flow at the walls. Also, this model is not appropriate for high pressure differences, which is expected to happen in the simulations of a high pressure water jet.

B.0.2 K-Omega Shear Stress Transport (SST)

The $k-\omega$ is a two-equation turbulence model, used for the closure of the Reynolds-averaged Navier-Stokes Equations (RANS equations). The $k-\omega$ model is accurate in estimating the turbulence in the water body, but fails near the walls. Combining the $k-\omega$ model with the Shear Stress Transport, it can estimates the flow near the boundaries accurately. However, the model becomes inaccurate in regimes with a high Reynolds number. The governing equations are shown below.

The turbulence kinetic energy k is described by:

$$\frac{\partial}{\partial t}(\rho k)+\frac{\partial}{\partial x_i}(\rho k \mu_i)=\frac{\partial}{\partial x_j}\left(\Gamma_k\frac{\partial k}{\partial x_j}\right)+\tilde{G_k}-Y_k+S_k \tag{B.3}$$

The specific rate of dissipation ω is described by:

$$\frac{\partial}{\partial t}(\rho \omega)+\frac{\partial}{\partial x_i}(\rho \omega \mu_i)=\frac{\partial}{\partial x_j}\left(\Gamma_\omega\frac{\partial \omega}{\partial x_j}\right)+G_\omega-Y_\omega+D_\omega+S_\omega \tag{B.4}$$

Where $\tilde{G_k}$ represents the generation of turbulence kinetic energy due to average velocity gradients, and G_ω the generation of ω. Γ_k and Γ_ω are the effective diffusivity of k and ω. Y represents the dissipation of k and ω, D_ω the cross-diffusion and S_k and S_ω are the source terms.

B.0.3 Detached Eddy Simulation (DES)

The DES model is used in combination with the $SSTk-\omega$ model. In the DES model, the term Y_k is modified such that:

$$Y_k = \rho\beta^* k\omega F_{DES} \tag{B.5}$$

Where F_{DES} is expressed as follows:

$$F_{DES} = max\left(\frac{L_t}{C_{DES}\Delta_{max}}, 1\right) \tag{B.6}$$

Where C_{DES} is the calibration constant and Δ_{max} the grid spacing. The turbulence length scale L_t is defined as follows:

$$L_t = \frac{\sqrt{k}}{\beta^*\omega} \tag{B.7}$$

* The equations in this appendix are taken from the Ansys manual. Further derivations and information about turbulence model can be found on: `https://www.sharcnet.ca/Software/Ansys/17.0/en-us/help/flu_th/flu_th_rans_sst.html`

C. Simulations Results

This appendix shows the velocity and pressure fields at different cavity-depths (not all of the simulated depths), simulated with the *Ansys Fluent* software.

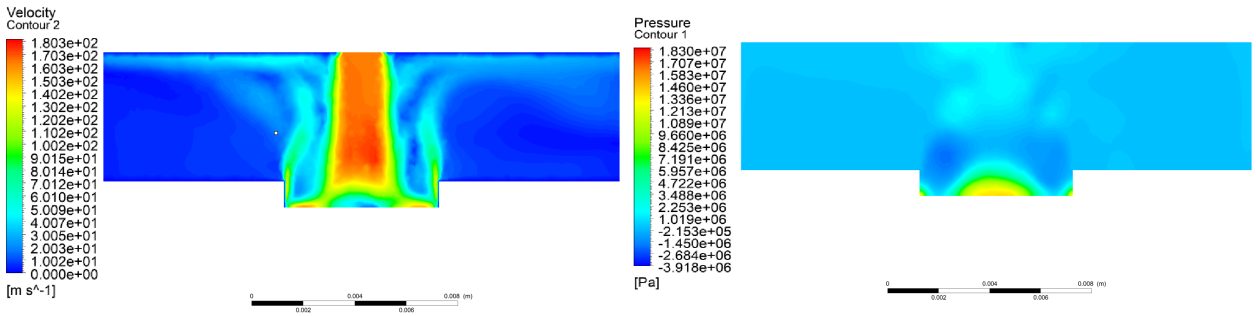

Figure C.1: Velocity field (left) and pressure field (right) of the simulation of a jet in a cavity of 1mm depth at time step 21 (0.021s).

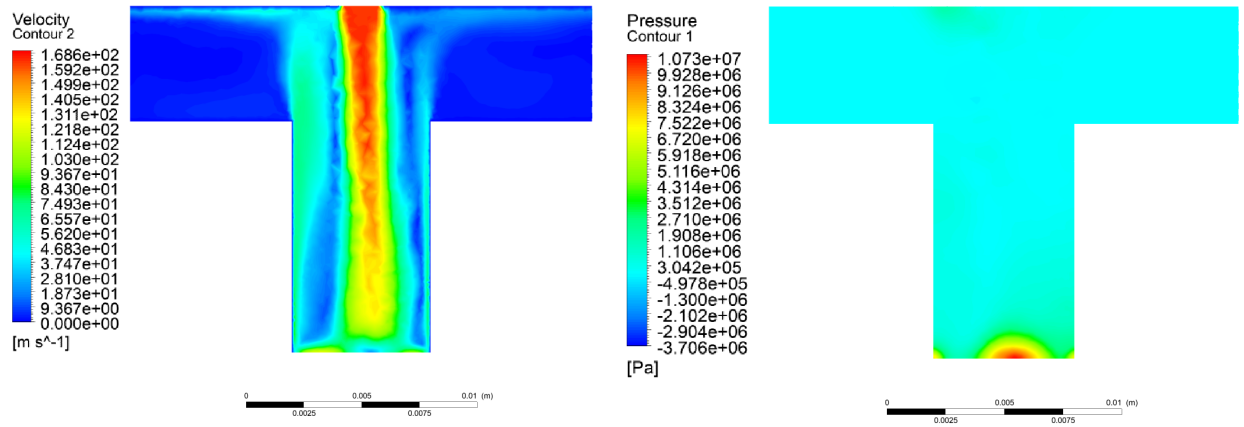

Figure C.2: Velocity field (left) and pressure field (right) of the simulation of a jet in a cavity of 10mm depth at time step 3 (0.003s).

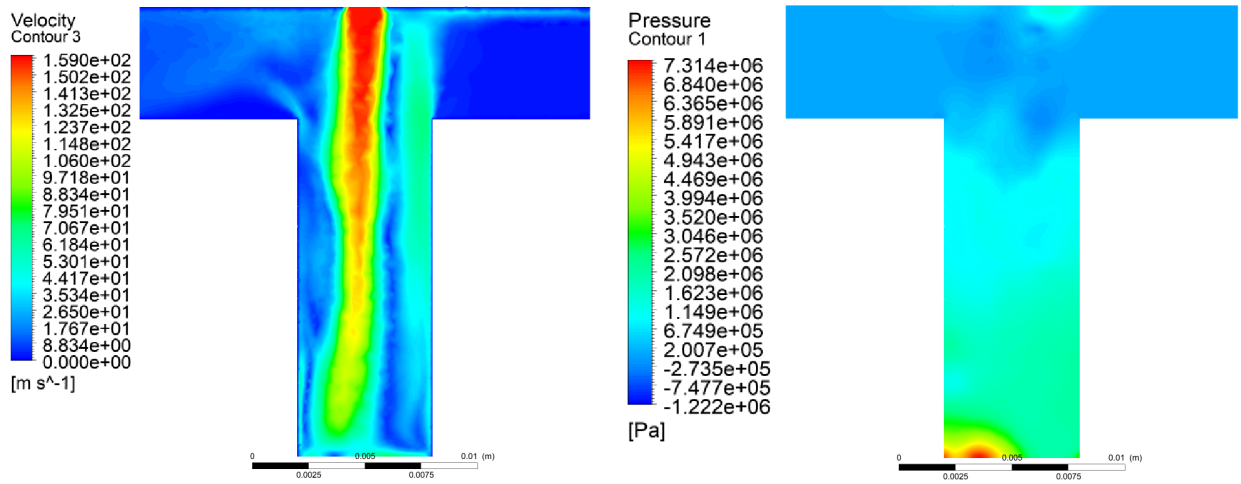

Figure C.3: Velocity field (left) and pressure field (right) of the simulation of a jet in a cavity of 15mm depth at time step 27 (0.027s).

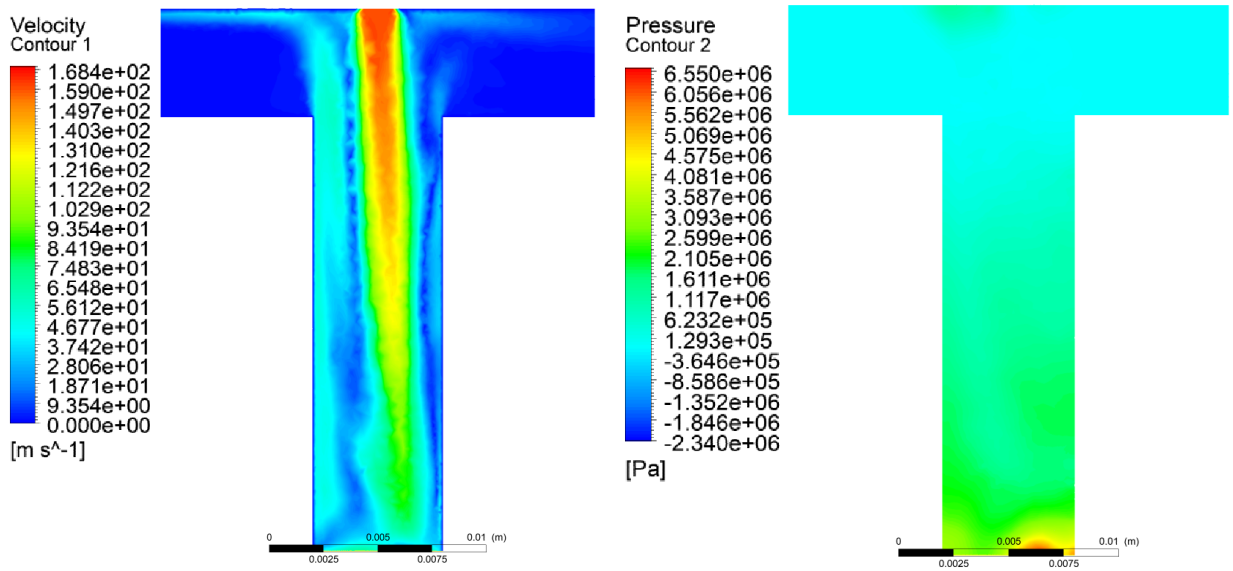

Figure C.4: Velocity field (left) and pressure field (right) of the simulation of a jet in a cavity of 20mm depth at time step 2 (0.002s).

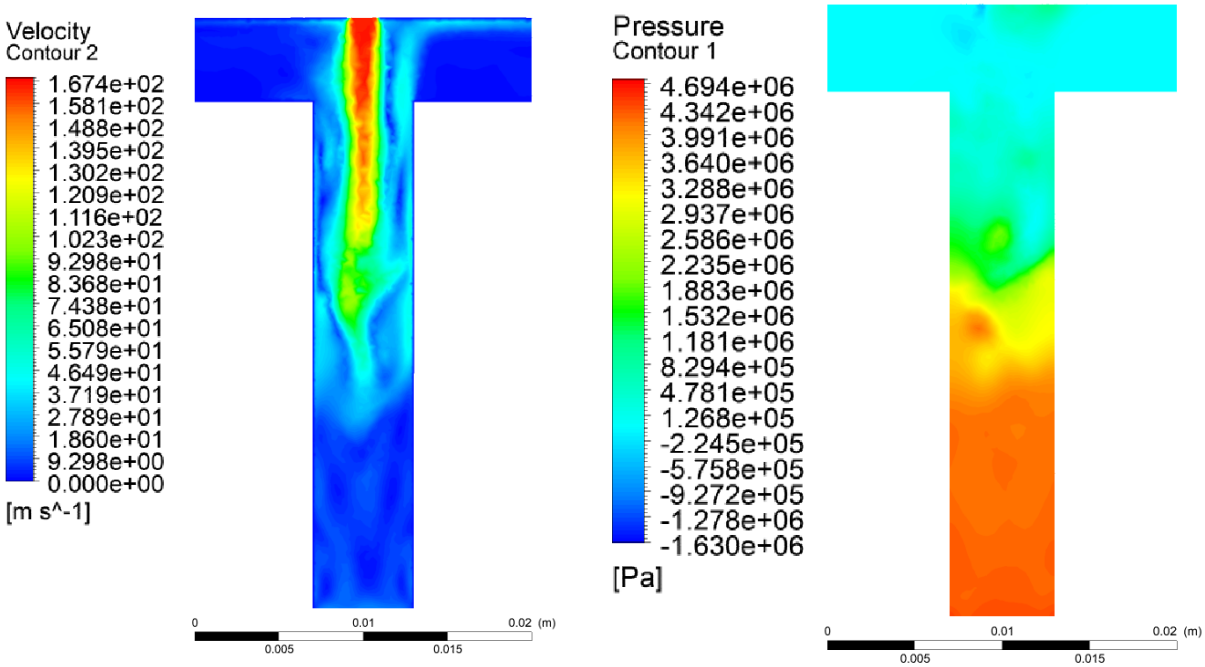

Figure C.5: Velocity field (left) and pressure field (right) of the simulation of a jet in a cavity of 30mm depth at time step 22 (0.022s).

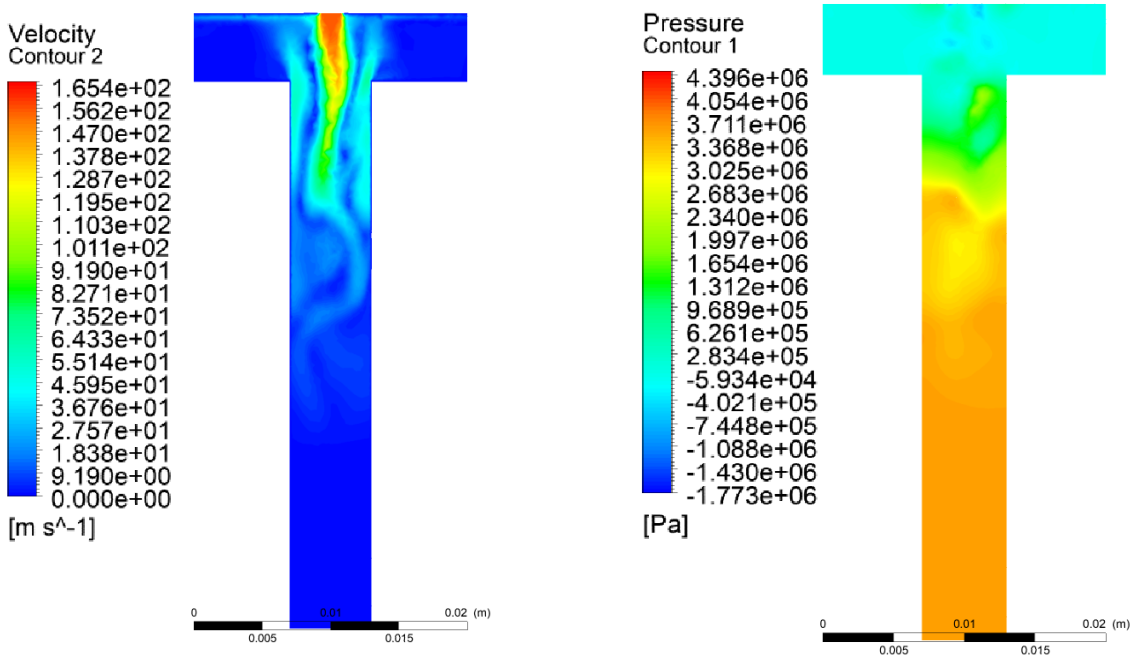

Figure C.6: Velocity field (left) and pressure field (right) of the simulation of a jet in a cavity of 40mm depth at time step 32 (0.032s).